Titre: Title:	Design and Implementation of Novel Nonlinear Processes in Bulk and Waveguide Periodic Structures
Auteur: Author:	Meenu Kajal
Date:	2014
Type:	Mémoire ou thèse / Dissertation or Thesis
Référence: Citation:	Kajal, M. (2014). Design and Implementation of Novel Nonlinear Processes in Bulk and Waveguide Periodic Structures [Ph.D. thesis, École Polytechnique de Montréal]. PolyPublie. https://publications.polymtl.ca/1347/

UNIVERSITÉ DE MONTRÉAL

DESIGN AND IMPLEMENTATION OF NOVEL NONLINEAR PROCESSES IN BULK AND WAVEGUIDE PERIODIC STRUCTURES

MEENU KAJAL

DÉPARTEMENT DE GÉNIE PHYSIQUE

ÉCOLE POLYTECHNIQUE DE MONTRÉAL

THÈSE PRÉSENTÉE EN VUE DE L'OBTENTION

DU DIPLÔME DE PHILOSOPHIAE DOCTOR

(GÉNIE PHYSIQUE)

FÉVRIER 2014

UNIVERSITÉ DE MONTRÉAL

ÉCOLE POLYTECHNIQUE DE MONTRÉAL

Cette thèse intitulée:

DESIGN AND IMPLEMENTATION OF NOVEL NONLINEAR PROCESSES IN BULK AND WAVEGUIDE PERIODIC STRUCTURES

présentée par: KAJAL Meenu

en vue de l'obtention du diplôme de : Philosophiae Doctor

a été dûment acceptée par le jury d'examen constitué de :

M. FRANCOEUR Sébastien, Ph.D., président

M. KASHYAP Raman, Ph. D., membre et directeur de recherche

M. CARDINAL Christian, Ph.D., membre

M. LÉGARÉ François, Ph.D., membre

dedicated to my parents and grandparents,

for bringing me up in a way to accept challenges

in memory of

my loving uncle Azad Singh

ACKNOWLEDGEMENTS

My graduate studies would have been impossible without the support of many people and it is my immense pleasure to thank all those people who have helped me enjoy my graduate life and make it to the finish line. I would like to express my heartfelt gratitude to my supervisor and research director, Prof. Raman Kashyap who has always believed in my potential and offered me with invaluable support, encouragement and guidance during my PhD. His advice in science, and life, in general, has greatly enriched my academic learning. I am grateful to his wife Monika Kashyap and daughter Hannah Kashyap for their support and for considering me as a part of their family.

I would like to thank all of my colleagues and friends at Advanced Photonics Concept Laboratory (APCL) whom I have worked and collaborated with. I would like to especially acknowledge Dr. Amirhossein Tehranchi for his invaluable help during my PhD and in writing this thesis. In addition I would like to thank Ameneh Bostani who has been a constant support during the later years of my PhD, and has always been fun to work with. I feel gratified to have been surrounded by wonderful colleagues: Dr. Aissa Harhira, Elton Soares de Lima Filho, Jérôme Lapointe, Jérôme Poulin, Mathieu Gagné, Mohamad Diaa Baiad, Sébastien Loranger, and Dr. Krishnamoorthy Pandiyan. I would not have enjoyed my PhD as much if I did not get to share the lab with these amazing people. I would like to give a special acknowledgement to the technicians at Poly-Grames Research Center and Laboratoire de Micro-fabrication: Mr. Jules Gauthier, Dr. Alireza Hajhosseini Mesgar and Mr. Christophe Clément for their support in fabrication work.

My PhD studies would have been impossible without the dream of my loving family which includes my grandparents, parents, my sisters Seenu & Seema, and my brother Tarun. Another very important person who has been instrumental during my graduate career is my husband, Vikas Kajal. His continuous support, motivation and patience have made this journey a fun ride. Last but not the least, I would like to thank my sister-in-law Monika Kajal and friends Gargi Sharma, Girudiha Kuganathan, Indrani Bhattacharyya and Kanwarpal Singh for their unending support and affection.

RÉSUMÉ

Les réseaux de télécommunication sont confrontés à une demande croissante de mettre en oeuvre une infrastructure de réseaux tout-optique pour permettre le déploiement à grande échelle de nouveaux services à haut débit triple jeu (i.e. IPTV, vidéo sur demande, voix sur IP). L'un des défis avec ces applications de diffusion vidéo, c'est que celle-ci sont beaucoup plus distribuées et de nature multi-points, contrairement aux réseaux traditionnels de communication point à point. Les composants électroniques à haut débit actuellement déployés dans les réseaux optiques sont incapables de gérer la demande sans précédent en bande passante pour la radiodiffusion en temps réel des sources multimédia. La solution réside essentiellement dans l'augmentation de la transparence des réseaux, i.e. en remplaçant l'électronique de traitement du signal à haute vitesse par des processeurs de signaux tout-optiques, capables d'effectuer des opérations telles que la commutation de longueurs d'onde, multiplexage en fréquence et en temps, la compression d'impulsions optiques, et ce, entièrement dans le domaine optique. Cette thèse vise à fournir une solution tout-optique pour la conversion de longueurs d'onde à large bande et la radiodiffusion sélective en longueur d'onde, desoutils essentiels des réseaux de communication optique, basé sur le principe du mélange d'ondes avec quasi-accord de phase dans les matériaux non linéaires. La technique de quasi-accord de phase (QPM) permet d'obtenir un accord de phase dans de longs cristaux en utilisant des structures (réseaux) de domaines inversés périodiquement, ce qui permet de faire varier le signe de la non-linéarité selon le domaine ; principe connu sous le nom de polarisation périodique du cristal. Il en résulte de nouveaux composants de fréquence à haute efficacité de conversion qui ont été mis en œuvre avec succès pour divers procédés tels que la génération de seconde harmonique (SHG), la génération de somme fréquences (SFG) et la génération de différence de fréquences (DFG).

Conventionnellement, les réseaux de communication optique ont une fenêtre de fonctionnement de ~35 nm centrée à 1,55 μm, connue sous le nom de bande C. La conversion de longueurs d'onde d'un signal d'entrée d'un canal dans la bande C à un canal de sortie également dans la bande C, a été démontrée dans des guides d'onde de niobate de lithium polarisé périodiquement (PPLN) par l'intermédiaire d'un procédé de mélange de différence de fréquences en cascade SHG/DFG et en cascade (c-) SFG/DFG. Bien que ces techniques aient été mises en œuvre pour générer de la conversion de longueurs d'onde dans la bande C à l'aide de PPLN, le but de cette thèse est de surmonter certaines de leurs limites en proposant des améliorations dans la

conception des réseaux de PPLN pour la conversion de longueur d'onde accordable et de l'émission flexible en longueur d'onde. Nous montrons ici, pour la première fois, une démonstration expérimentale d'une largeur de bande aplanie de CGSF / DFG réalisée par un léger désaccord des longueurs d'onde de la pompe par rapport à la condition d'accord de phase. De plus, en utilisant deux pompes rapprochées dans un processus cGSF/DFG dans un guide d'onde de PPLN, on arrive à générer deux pics de SH et un pic de SF. Profitant de cela, un signal a été émis à trois ondes complémentaires (*idlers*) dans la bande C en utilisant la combinaison de cSHG / DFG et le processus CGSF / DFG.

Même si un réseau PPLN à période uniforme a été utilisé afin d'augmenter l'efficacité par l'utilisation du coefficient du tenseur non-linéaire le plus élévé via QPM, le problème réside dans une bande passante étroite limitant le doublage de fréquences. La largeur de bande étroite limite le choix des longueurs d'onde de pompe dans un processus de conversion en cascade et par conséquent la longueur d'onde du signal converti est également fixée pour une longueur d'onde de pompe donnée. L'objectif de cette thèse est d'améliorer la bande passante de doublage de fréquences qui est nécessaire pour deux raisons principales: d'une part, afin de réaliser l'accordabilité de conversion de longueurs d'onde d'un signal à pour n'importe quel canal dans la bande de communication, et d'autre part, afin d'émettre un signal sur plusieurs canaux simultanément en employant plusieurs lasers de pompage à l'intérieur de la large bande passante ainsi obtenue par cGSF/DFG. Dans cette thèse, la démonstration expérimentale d'une structure artificielle en quasi-accord de phase avec des périodes variables dans un matériau de PPLN a été faite pour la première fois, afin de fournir une bande passante plus large pour la GSH, ce qui facilite la flexibilité dans la conversion de longueurs d'onde sur la bande C.

Le premier dispositif de PPLN conçu est proposé et démontré dans cette thèse et sert à la conversion de longueurs d'onde sur une large bande. Il possède un domaine apériodique au centre d'un autre réseau, qui liui est périodique. Ce PPLN déphasé ou apériodique (a-)PPLN a une réponse double pic en GSH avec une augmentation de la bande passante par rapport à un PPLN uniforme. Il est démontré qu'en utilisant le réglage en température, on peut faire varier les conditions d'accord de phase du a-PPLN et ainsi on peut améliorer davantage la largeur de bande de la GSH. L'émission d'un triplet d'ondes complémentaires est également démontré et pour la première fois, les signaux complémentaires sont accordés sur 40 canaux dans la bande C avec emplacement accordable tout en gardant un espacement uniforme entre les canaux dans un

système de multiplexage WDM assisté par désaccord en longueur d'onde de la pompe et par le réglage en température.

Bien que le système de réglage de la température permette de résoudre le problème de la bande passante étroite de la GSH ainsi que de l'accordabilité de conversion, la vitesse du changement de température est insuffisante pour certaines applications WDM qui nécessitent un traitement du signal ultra-rapide. Par conséquent, un appareil à haut débit indépendant de la température a été démontré pour la première fois dans la présente thèse. Ceci est réalisé en utilisant un réseau apodisé possédant quelques domaines à tailles variables « step-chirped grating (SCG) », qui a une largeur de bande intrinsèque de GSH de 30 nm chevauchant la bande C. Ce dispositif permet d'éviter la nécessité d'utiliser le réglage en température et conduit à la conversion de longueurs d'onde accordables et l'émission flexible de canaux. De plus, l'utilisation d'une seule longueur d'onde accordable de pompe dans le SC-PPLN, permettant la conversion d'un signal dans la bande C à un doublet d'ondes complémentaires et accordables par processus cSHG/DFG est démontré pour la première fois. Enfin, en profitant de la grande largeur de bande SH-SF, pour la première fois, on obtient une émission hautement accordable "agile" d'un signal à sept ondes complémentaires s'étendant à travers la bande C, avec position variable dans le réseau de communication est réalisé sur la base d'un procédé combinant cSHG/DFG et cSFG/DFG. En réglant les deux longueurs d'onde de pompe sur moins de 6 nm dans le large bande passante SH-SF, l'émission est réalisée à travers ~70 canaux WDM dans un espacement de 50 GHz sur le réseau WDM.

ABSTRACT

The telecommunication networks are facing increasing demand to implement all-optical network infrastructure for enabling the wide deployment of new triple play high-speed services (e.g. IPTV, Video On Demand, Voice over IP). One of the challenges with such video broadcasting applications is that these are much more distributed and multi-point in nature unlike the traditional point-to-point communication networks. Currently deployed high-speed electronic components in the optical networks are incapable of handling the unprecedented bandwidth demand for real-time multimedia based broadcasting. The solution essentially lies in increasing the transparency of networks i.e. by replacing high speed signal processing electronics with all-optical signal processors capable of performing signal manipulations such as wavelength switching, time and wavelength division multiplexing, optical pulse compression etc. all in optical domain. This thesis aims at providing an all-optical solution for broadband wavelength conversion and tunable broadcasting, a crucial optical network component, based on quasi-phase-matched wave mixing in nonlinear materials. The quasi phase matching (QPM) technique allows phase matching in long crystal lengths by employing domain-inverted gratings to periodically reverse the sign of nonlinearity, known as periodic poling. This results into new frequency components with high conversion efficiency and has been successfully implemented towards various processes such as second harmonic generation (SHG), sum- and difference- frequency generation (SFG and DFG).

Conventionally, the optical networks has an operation window of ~35 nm centered at 1.55 μm, known as C-band. The wavelength conversion of a signal channel in C-band to an output channel also in the C-band has been demonstrated in periodically poled lithium niobate (PPLN) waveguides via the process of difference frequency mixing, cascaded SHG/DFG and cascaded SFG/DFG. While a DFG process utilized a pump wavelength in 775nm regime, it suffered from low efficiency due to mode mismatch between the pump and the signal wavelengths; whereas the technique based on cSHG/DFG or cSFG/DFG eliminated the mode mismatch problem with pump(s) lying in the 1.55 μm wavelength regime. In this thesis, for the first time a flattened bandwidth of cSFG/DFG have been experimentally realized by slight detuning of the pump wavelengths from their phase matching condition. Moreover, employing two closely spaced pumps in a cSFG/DFG process in a PPLN waveguide, a signal has been broadcast to three idlers in C-band.

Although a uniform period PPLN grating increases efficiency by the use of highest nonlinearity tensor coefficient via QPM, it suffers from the limitation of a narrow bandwidth of frequency doubling. The narrow bandwidth restricts the choice of pump wavelengths in a cascaded conversion process and consequently the converted signal wavelength is also fixed for a given signal wavelength. Enhancing the frequency doubling bandwidth is necessary for mainly two reasons: firstly, to achieve the tunability of wavelength conversion of a signal to any channel in the communication band; and secondly, to broadcast a signal to several channels simultaneously by employing multiple pump lasers within its broad bandwidth. In this dissertation, the experimental demonstration of an engineered quasi-phase matched structure with varying periods has been done for the first time to provide increased bandwidth of SH, which facilitates the flexibility in the wavelength conversion over C-band.

The first engineered PPLN device proposed and demonstrated in this thesis for broadband wavelength conversion has an aperiodic domain in the center of an otherwise periodic grating. This phase-shifted or aperiodic (a-) PPLN has a dual-peak SH response with an increase in bandwidth compared to a uniform PPLN. It has also been shown that using temperature tuning, the phase matching conditions of the aPPLN can be varied and its SH bandwidth can be further enhanced. The triple-idler broadcasting is shown and for the first time, the idlers are tuned across 40 channels in C-band with flexible location and mutual spacing in the WDM grid assisted with pump detuning and temperature tuning.

Although the temperature-tuning scheme solves the problem of narrow SH bandwidth and tunability of conversion, the slow speed of temperature change makes it inadequate for ultra-fast WDM applications. Therefore, a temperature-independent broadband device has been demonstrated for the first time in this dissertation, using a step-chirped grating (SCG), which has an inherent 30-nm SH bandwidth overlapping the C-band. This device obviates the need of temperature tuning and leads to tunable wavelength conversion and flexible broadcasting. Employing a single tuned pump wavelength in the SC-PPLN, conversion of a signal in C-band to tunable dual idlers via cSHG/DFG process is demonstrated for the first time. Also by taking advantage of the broad SH-SF bandwidth, for the first time, agile broadcasting of a signal to seven idlers spanning across C-band with variable position in the grid is realized based on cSHG/DFG and cSFG/DFG processes. By tuning the two pump wavelengths over less than 6 nm, broadcasting is achieved across ~70 WDM channels within the 50 GHz spacing WDM grid.

TABLE OF CONTENTS

LIST OF TABLES

LIST OF FIGURES

LIST OF ACRONYMS

APE	Annealed Proton Exchange
aPPLN	Aperiodically Poled Lithium Niobate
ASE	Amplified Spontaneous Emission
BW	Bandwidth
C-band	Conventional band (optic communication)
CW	Continuous Wave
DFG	Difference Frequency Generation
EDFA	Erbium-Doped Fiber Amplifier
FH	Fundamental Harmonic
FWHM	Full-Width Half Maximum
FWM	Four-Wave Mixing
HF	Hydrofluoric acid
LN	Lithium Niobate (LiNbO3)
MgO	Magnesium Oxide
NLO	Nonlinear Optic
OSA	Optical Spectrum Analyzer
PC	Polarization Controller
PPLN	Periodically Poled Lithium Niobate
QPM	Quasi Phase Matching
SC	Step-Chirped
SFG	Sum Frequency Generation
SH	Second Harmonic

SHG	Second Harmonic Generation
SOA	Semiconductor Optical Amplifiers
Ti:$LiNbO_3$	Titanium Indiffused Lithium Niobate (Ti:LN)
WC	Wavelength Converter
WDM	Wavelength Division Multiplexing
WG	Waveguide

LIST OF SYMBOLS AND NOTATIONS

A	Amplitude
a	Duty ratio
BW	Device bandwidth
c	Speed of light in vacuum
d	Nonlinear coefficient
d_{eff}	Effective nonlinear coefficient
E	Electric field
i	$\sqrt{-1}$
I	Intensity
k	Wavenumber
L	Grating length
L_c	Coherence length
n	Number of segments
n_e	Refractive index of extraordinary polarized wave
n_o	Refractive index of ordinary polarized wave
n_ω	Refractive index at ω
P	Polarization
P^L	Linear Polarization
P^{NL}	Nonlinear Polarization
P_0	Input power
r	displacement vector
R	Reflectivity

T	Temperature
w	Beam spot size
W	Width of waveguide
α	Propagation loss
β	Propagation constant
η	Efficiency
δ	Wavelength detuning
Δk	Phase-mismatch parameter
Δn	Refractive index difference
$\Delta\Lambda$	Chirp step
κ	Coupling factor
Λ	Period of inverted domain grating
ω	Frequency
λ	Wavelength
λ_c	Central wavelength
Φ	Phase
ε_0	Permittivity of free space
μ_0	Permeability of free space
$\chi(i)$	Susceptibility of order (i)

CHAPTER 1
INTRODUCTION

1.1 Motivation

Fiber optic communication systems with dense WDM channel spacing have become the established form for long-haul data transmission. As the number of independent wavelengths in the network is limited to approximately 160 [1], wavelengths must be reused which can lead to conflicts at routing nodes and, hence, network congestions. To meet the explosive demand for Internet bandwidth required for high definition video broadcasting or triple play broadband services [2], there is a need to find solution for such network congestion problems. One of the solutions is to make the networks transparent i.e. by replacing high speed signal processing electronics with all-optical signal processors capable of performing signal manipulations such as wavelength switching, time and wavelength division multiplexing, optical pulse compression etc. all in optical domain. Nonlinear (NL) optics based quasi-phase-matched (QPM) devices such as periodically poled lithium niobate have been widely researched for all-optical wavelength conversion and signal processing because of their high speed, low noise performance and no dependence on bit rate and signal modulation format.

While all-optical wavelength conversion in QPM devices has been extensively investigated to achieve higher efficiency, the unavailability of a single device which can demonstrate the broadcasting and multicasting functions is real problem. Moreover, the temperature needs to be maintained carefully, if these devices are to be used in the network, a task which requires the availability of control systems and often leads to additional power consumption. A practical solution would be to design a temperature-independent conversion device which can freely operate over the entire communication band. The aim of this dissertation is to develop temperature-insensitive broadband nonlinear optical QPM device for flexible wavelength broadcast applications in next generation all-optical communication systems, using appropriate step-chirped designs to ease the fabrication process for the engineered inverted domain structures in lithium niobate.

This chapter reviews the developments in the field of nonlinear frequency conversion, introduces the concepts of various phase-matching techniques and gives an overview of the dissertation.

1.2 Literature Review

Nonlinear optics describes the interaction of materials with light in the presence of intense optical fields which became available only after the invention of the laser in 1960 [3]. The first nonlinear optical process observed was second harmonic generation in an experiment by Franken *et al.*, 1961 [4] who observed the generation of 347.2 nm wavelength radiation in a crystal of quartz irradiated by intense beam at a wavelength of 694.3 nm light from a ruby laser. Thereafter in 1962, Bloembergen and Armstrong [5] formulated the interactions between coherent light waves in an anisotropic nonlinear medium and solved the coupled amplitude equations for conversion of fundamental power to higher harmonics. These nonlinear interactions require phase matching between the interacting waves for efficient energy transfer which is otherwise difficult to achieve because of the material dispersion. The phase matching for three wave interaction in nonlinear crystals can be classified into three different types. In a type-I interaction, two FH photons of ordinary polarization combine to produce a SH photon with extraordinary polarization. Second type of phase matching known as type II requires two lower frequencies to be orthogonally polarized, and generated wave along one of the two polarization states. The third type of interaction known as type-0 phase matching involves all three waves with same polarization. Type-I and type-II phase matching can be realized by birefringent phase matching whereas type-0 phase matching cannot be produced in an as-grown nonlinear crystal and requires engineering of the nonlinearity profile, as will be discussed later in this section.

In 1962 Giordmaine and Maker [6, 7] introduced the most popular phase matching scheme involving orthogonal polarizations in birefringent crystals in which the birefringence exactly compensates for the material dispersion. Since then several models for generalised harmonic generation in case of plane finite monochromatic beams have been constructed and many experimental techniques have been developed owing to the discovery of new sources of light and nonlinear media [8, 9]. The effect of focusing of the interacting beams on second harmonic generation (SHG) was first considered by Kleinman and Boyd in their famous papers of 1966 and 1968 [10, 11]. Due to the restrictions in using birefringent phase-matching which limits nonlinear interaction to specific nonlinearity tensor components, an alternative technique known as quasi-phase-matching was proposed by Armstrong to correct the phase mismatch by incorporating a periodic inversion of sign of nonlinearity in the crystal, as schematically shown in Figure 1-1 [5]. Advantage of quasi-phase matching is that any interaction within the transparency range of the

material can be non-critically phase matched, such as type-0 phase matched interaction, which is otherwise not permitted by birefringent phase matching. Another benefit is that the interacting waves can be chosen so that efficient coupling occurs through the largest element of the $\chi^{(2)}$ tensor. Moreover, quasi-phase matching allowed longer crystal lengths and turned quadratic nonlinear optics into an effective approach to generate coherent radiation at frequencies not attainable directly by available lasers.

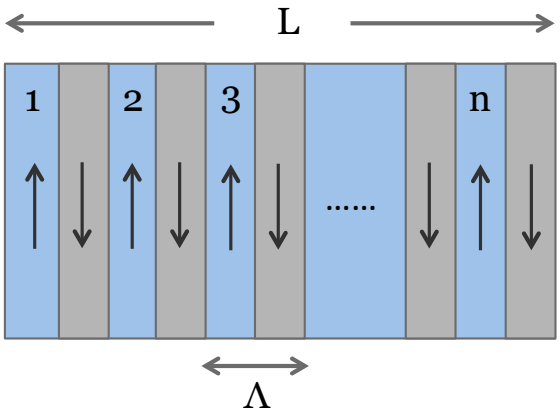

Figure 1-1: Schematic of a quasi-phase matched periodic nonlinear structure of length L. The arrows show reversed polarization of the adjacent domains. The length Λ of the grating period can be altered to obtain phase matching at desired wavelength.

The early experiments on QPM were based on stacking polished plates of nonlinear material such as Gallium Arsenide (GaAs) together while alternating the sign of susceptibility by 180° rotation of the orientation of successive plates to create a continuous monotonic growth of nonlinear-frequency generation process [12]. This technique was however very time consuming and suffered from the reflection losses at plate interfaces. Birefringent phase matching was thus more popular for SHG experiments because of its simplicity when compared to the complex fabrication process for QPM structures with control on the micron scale over long lengths. Although multi-domain oxide ferroelectrics have been known as a potential medium for quasi phase matched harmonic generation due to change in the sign of the nonlinear susceptibility with domain reversal (Miller 1964) [13], the real breakthrough in QPM experiments occurred in 1991 through the introduction of lithographically patterned devices and electric field poling methods. These involve patterning a periodic electrode on one surface of the crystal, and applying a

voltage to reverse the domains in the electroded regions [14]. The electrical poling method facilitated fabrication of both waveguide and bulk periodic structures and provided longer interaction lengths leading to orders of magnitude higher performance than those fabricated with the stacking of plates method. This technique was then successfully applied by Yamada *et al.* (1994) [15], in waveguides and by Burns *et al.* (1994) [16], Webjorn *et al.* (1995) [17], Myers *et al.* (1995) [18] and Miller *et al.* (1997) [19] for efficient SHG in bulk periodically poled lithium niobate (PPLN) crystals.

Over the past two decades, lithium niobate (LN) in the form of PPLN, a domain engineered LN crystal with periodic inversion of ferroelectric domains, has gained popularity as a material of choice for QPM nonlinear harmonic generation. This is due to its large nonlinear coefficient d_{33}, long interaction lengths and noncritical phase matching at arbitrary wavelengths of interest in a wide transparency range covering the visible and extending into the mid-IR. Further, easy lithographic patterning and the commercial availability of large crystals of optical quality at low costs due to a matured poling technology have made available high conversion efficiency nonlinear devices based on LN. On the negative side, LN has low damage threshold and is prone to photorefractive damage at relatively low intensities [20] which leads to distortion of beams passing through the crystal thereby disturbing the phase matching condition. Studies have revealed that doping of LN with MgO or working at elevated temperatures proves to be effective in increasing the photorefractive damage threshold [21, 22].

Fabricating waveguides in PPLN has been quite popular to improve the conversion efficiencies by two to three orders of magnitude over the bulk devices by maintaining high optical intensities of the interacting beams over considerable distances [23, 24]. Compared to a bulk device, waveguides eliminates the trade-off between a small spot size and long interaction length, which makes the technique highly efficient even with a few milliwatts of pump power [23]. Incidentally, with an average pump power of 50 mW, the intensity of light in the LN waveguides can reach 100 kW/cm^2 and can give rise to photorefractive optical damage in the material [24]. Devices in the bulk configuration are thus desirable for several 100's of watts of CW powers in high power laser systems to avoid reaching the limits imposed by optical damage. Although the efficiency of waveguide devices is very high compared to bulk devices, when the total output power is the main concern, bulk devices score above waveguides. Further, by focusing the laser beam tightly in a nonlinear bulk crystal, the conversion efficiency can be enhanced. An optimum

focusing condition for Gaussian beams derived by Boyd and Kleinman (BK) (1968) [9] represents a compromise between tight confinement and long interaction length. Moreover, with the advent of picosecond and femtosecond pulsed lasers, higher conversion efficiencies are achieved even in the bulk as higher peak intensities are obtained in pulse mode.

As apparent from the above discussion, QPM efficiency increases by allowing long interaction lengths and the use of highest nonlinearity coefficient d_{33} in LN, which is otherwise not feasible in birefringence phase matching. However, the problem associated with quasi-phase matched wavelength conversion is the narrowband nature of SHG, as the bandwidth is inversely dependent on the grating length. For several applications, such as wavelength conversion for optical networks, the device response should be made broadband and flat across the telecom band. To make these devices broadband is rather difficult, as it requires techniques to induce chirp by varying the poling period in a very special way to allow it to be fabricated with existing techniques. Chirping the grating structure can broaden the bandwidth of SHG but leads to ripples in frequency response and there are fabrication problems due to very small random changes in the grating period. Several nonlinear devices with aperiodic gratings have been proposed for bandwidth broadening or pulse compression [25]. Imeshev *et al.* engineered the amplitude and phase response of SHG in Fourier synthetic QPM gratings [26] while Schober *et al.* proposed non-collinear quasi-phase-matched interactions alongwith spectral angular dispersion for broadband SHG of ultrashort optical pulses [27]. A chirped, fanned PPLN QPM grating has also been used for continuously tunable compensation of linear chirp in an input pulse [28]. Arbore *et al.* demonstrated the use of chirped-period-poled lithium niobate to generate second-harmonic of ultra-short pulses that are stretched or compressed relative to input fundamental harmonic pulses [29]. The continuous chirp requires complicated fabrication techniques and while the bandwidth is broadened there are ripples in the frequency response. An effective method for broadband SHG based on apodized step-chirped gratings in PPLN waveguides has been investigated theoretically by Tehranchi and Kashyap, which facilitates the fabrication process by increasing the step changes in the period. Bandwidth flattening was achieved by apodizing the grating and slightly detuning the pump wavelengths from their QPM condition [30, 31].

The earlier work on nonlinear optics based wavelength conversion devices was intended for obtaining compact and efficient short wavelength laser sources. Several experiments based on PPLN have been demonstrated including generation of cw green and blue light from diode

pumped solid state lasers etc. [17, 19, 32]. However, the technology soon established itself in interesting applications in optical communications and information processing. Difference frequency mixing in PPLN waveguides was investigated in detail as a popular choice for optical parametric devices by the groups of Sohler [33] and Fejer [33, 34]. Myers *et al.* demonstrated high power and high repetition-rate multi-grating OPOs [35, 36]. Meanwhile, other nonlinear devices such as semiconductor optical amplifiers (SOA's) based on cross-gain or cross-phase modulation were being investigated for optical gating and switching applications in networks [37, 38]. These devices suffered from problems of low extinction ratio, low bit rates and could not preserve signal phase information. The coherent approach for preserving phases is possible with wave mixing phenomenon based on second- or third-order nonlinearities. Out of these, the third order processes such as four wave mixing (FWM) is limited by its low efficiency due to a small value of the $\chi^{(3)}$ component. Using second order nonlinearity, DFG based wavelength conversion of a signal near 1.55 μm in the same band using an intense pump located in 775nm region was successfully demonstrated in periodically poled $\chi^{(2)}$ waveguide devices [39-41]. However, a very low conversion efficiency was obtained in DFG process as to generate an idler in the C-band it requires the pump wavelength to operate in 775nm band which is far off from the signals lying in the C-band. The efficient coupling into a waveguide is difficult to achieve due to mode-mismatch between the pump and signal beams. Due to this drawback of DFG based approach, research was soon directed to another technique based on cascaded second harmonic generation and difference frequency generation (cSHG-DFG), which allows the pump to be positioned within the 1.55 μm communication band [42, 43].

Cascaded second-order interactions in PPLN waveguides provide an effective solution and was numerically studied in single- and a more efficient double-pass configurations by K. Gallo *et al.* in 1999 [44]. Nevertheless, another approach for C-band wavelength conversion based on cascaded sum frequency generation (cSFG-) and DFG has attracted much attention. This approach requires a signal wavelengths in the 1.5-μm band while the two input pumps can be located just outside the 1.5-μm band, out of the broad bandwidth of the nonlinear device [45, 46]. Cascaded SFG-DFG is more advantageous than cascaded SHG-DFG for ultrafast-signal processing in WDM networks [47, 48]. Recently, Furukawa *et al.* [49] and Bogoni *et al.* [50] demonstrated all optical wavelength conversion of 160 Gb/s and 320 Gb/s picosecond optical signals, respectively, based on cSFG/DFG process in PPLN waveguide. The wavelength

conversion demonstrated in the devices based on cascaded quadratic nonlinearity was to generate one idler corresponding to each of the input signals. However, with ever-increasing data transmission capacity, WDM networks require tunable wavelength broadcasting by replicating a signal to several channels to facilitate flexible routing, switching and dynamic reconfiguration of the information carried by different channels. Chou *et al.* first implemented an engineered phase-reversal grating $\chi^{(2)}$ device in 1999 using multiple pumps for multiple idler generation based on DFG [51]. Later in 2003, Asobe *et al.* also demonstrated a DFG-based multiple channel wavelength conversion device with a continuously phase-modulated structure in a PPLN [52]. These two devices illustrate the broadcast conversion scheme owing to the freedom of pump wavelength location in a broad DFG bandwidth. However, cSHG-DFG and cSFG-DFG processes in a QPM periodic structure has a narrow pump bandwidth and the tunability of the pump is restricted. It was found that a much broader frequency doubling bandwidth is obtained in a type-I process utilizing d_{31} nonlinear coefficient [53]. Making use of this coefficient, a broadband wavelength conversion and broadcast device in PPLN were demonstrated by employing multiple pumps and type-I QPM for both SHG and DFG [54, 55]. With the type-I QPM nonlinear processes of cSHG-SFG/DFG, Gong *et al.* demonstrated wavelength broadcasting of a signal to seven fixed idlers employing two pump wavelengths [56]. The problem with these devices is low conversion efficiency owing to the use of non-preferred nonlinear coefficient (d_{31}) in a type-I QPM process. Also for practical optical communication networks, the tunability of multiple-QPM-based wavelength broadcasting is essential to provide variable number and location of output channels. Therefore, there is scope for improvement in the use of PPLN devices for wavelength broadcasting applications, to obtain a broad bandwidth and high efficiency utilizing the highest nonlinear coefficient d_{33} in a type-0 QPM process.

The research work in this Thesis is directed towards improving existing PPLN wavelength converters to optimize their functionality using simple device designs for practical applications in optic communication. The main contributions of this Thesis are in broadband flexible multicasting which are proposed and demonstrated, with the convenient fabrication of a few-sections of step-chirped periodic poled lithium niobate. Unlike a type-1 process, utilizing a type-0 process in a multi-peak temperature tuned PPLN with a broadband chirped PPLN, we benefit from both tunablity in bandwidth and high conversion efficiency. Experimental demonstration of

flattening of the ripples in the bandwidth of converted signals is done by slightly detuning the pump wavelengths from their optimum phase matching values.

1.3 Wavelength conversion and multicasting in optical networks

Transparent all-optical networks can provide high-speed large-bandwidth solutions over current networks which are limited by the speed of the optoelectronic hardware. Active signal routers enable re-assignment of the wavelength channels in WDM networks and hence improves flexibility in traffic management by avoiding network congestion. Thus, all-optical wavelength shifters or converters are most promising for future optical networks.

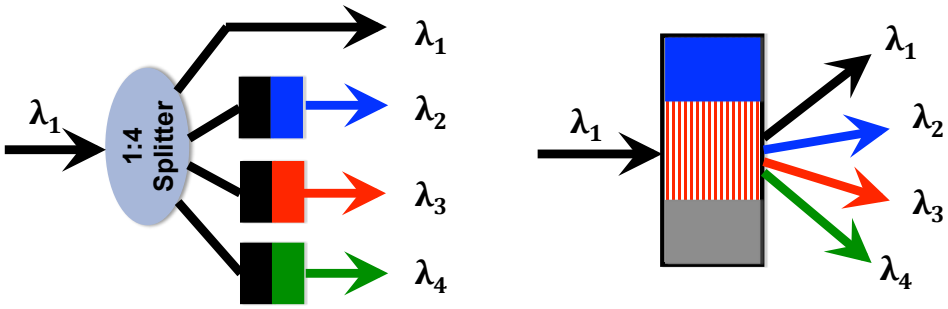

(a) (b)

Figure 1-2: A multicast converter: (a) Using splitters and WCs; (b) Using a single multicast WC.

Whilst a wavelength converter (WC) sends the signal channel to one destination channel, when coupled with optical multicasting, it proves to be an even more powerful feature in the global information transfer services. Multicasting or broadcasting refers to sending multiple copies of a single data channel to several destination channels spread over the grid. One way to realize multicasting is repeated-unicasting which means sending the same signal to multiple destinations in succession, which is definitely a slow and quite an inefficient method. Another simpler

solution is to split the optical signal to replicate multicast data. Multicast nodes can be classified into wavelength convertible multicast and non-wavelength convertible ones. In non-wavelength convertible multicast-nodes the data can only be switched into the space domain while in the wavelength convertible case it can be switched or replicated in space and the wavelength domain using a wavelength converter. A multi-wavelength converter is therefore capable of simultaneously replicating a signal on an input wavelength to several output wavelengths. Figure 1-2 describes schematic of two such wavelength convertible-multicasts. In the traditional approach of Figure 1-2 (a), multicast routers make use of optical power splitters and wavelength converters to replicate input data into different output wavelengths. In such a configuration, an input signal is first split into the required number of copies, and then each copy is wavelength converted to the desired wavelength using a dedicated converter. With the advances in WDM technology in which more and more wavelengths per fiber get unlocked, the design of such multicast switches becomes more and more challenging due to the increase in the number of WCs, switching elements, and splitters. Therefore, an improved design of a multicast router is desired which can provide full functionality with reduced switching and conversion complexity, as shown in Figure 1-2 (b), where a single device generates multiple copies with distinct wavelengths. Various methods for all-optical wavelength conversion have been implemented including: super-continuum in nonlinear fiber [57, 58], delay interferometers in SOA, FWM in SOA [59], which can be configured as a multicast device, however each of them has some shortcomings such as low extinction ratio, low bit rates and non-preservation of signal phase, compared to the mature technology of QPM nonlinear converters [60-69]. In this Thesis, research has been directed to develop a single nonlinear QPM device, which broadcasts a signal to several distinct channels via cascading of the second-order nonlinear process, as will be described in detail in the next chapters.

1.4 Overview of the dissertation

This dissertation is organized as follows:

Chapter 2 presents a theoretical review of the second order nonlinear optical processes beginning with the description of nonlinear polarization and susceptibility. Solutions of a set of coupled nonlinear equations are analyzed for the second harmonic generation, whereas coupled equations are provided for sum frequency and difference frequency generation process. The cascaded

second order interactions for same band wavelength conversion, which are important in optical communication networks are discussed.

In Chapter 3, the standard electric field poling procedure to fabricate periodic and aperiodic structures in nonlinear ferroelectric crystals is presented, focusing on periodically poled lithium niobate (PPLN). The structure of lithium niobate and the mechanism model behind the domain inversion in ferroelectrics is described. The details are then given for various steps followed in poling procedure and the chemical-etching method for domain visualization.

Chapter 4 discusses broadband wavelength conversion in PPLN waveguides based on cascaded SFG/DFG process. It is shown that the broadband conversion efficiency response can be flattened significantly by slight detuning of the pump wavelengths from their phase-matched conditions with only slight loss in efficiency. A signal is broadcast to three idlers in a periodic and an apodized chirped grating by launching two pump wavelengths in its SH/SF bandwidth utilizing cSHG/DFG and cSFG/DFG nonlinear processes.

In chapter 5, a specially designed phase-shifted narrowband PPLN structure is investigated for wavelength conversion and broadcasting scheme. Generation of variable number of peaks in the second harmonic spectrum is obtained employing the dual-peak nature of the SH tuning curve of the device. By changing the device temperature, the phase matching conditions are changed and a tunable SH response is obtained. The broadcasting of a signal to multiple idlers is experimentally demonstrated and the spacing and location of the idlers is varied by detuning the pump wavelengths and tuning the device temperature.

Chapter 6 describes a step-chirped (SC) grating specially fabricated in an LN substrate to obtain a broadband SH/response covering the optical communication C-band without the need for temperature tuning. Moreover, in this temperature independent scheme, multicasting of a signal to two and seven idlers is shown by launching pump lasers in the wide conversion bandwidth of SC-PPLN. Further, it is demonstrated that these multiple-idlers can be freely tuned over the 1.55 micron C-band targeting selective output channels in the WDM network grid by tuning of pump wavelengths.

In chapter 7, the summary of the work is presented and directions for future work are provided.

CHAPTER 2
THEORY OF NONLINEAR FREQUENCY MIXING

2.1 Overview

The work on all-optical wavelength conversion and broadcasting developed in this thesis are implemented by cascading second-order nonlinear processes. In order to gain an understanding of the underlying theory, the derivation of the nonlinear susceptibility and various symmetry conditions are provided. In the following section, various phase matching techniques employed for efficient harmonic generation are discussed. Thereafter, description of coupled nonlinear equations for various second-order nonlinear processes is given. The SHG efficiency for pump, both non-depleting and depleting, is calculated and two other second-order processes of sum frequency generation and difference frequency generation which are basis of experiments reported in this dissertation are reviewed. An introduction is given in the end for cascading of second-order nonlinear optical conversion, which is an established technique for optical communication applications.

2.2 Nonlinear susceptibility and symmetry conditions

When an electromagnetic wave passes through a dielectric material, the electric field associated with it causes displacement in the centers of positive and negative charge of constituent atoms which leads to an induced polarization in the material. Since the electromagnetic wave creates a time-varying electric field in the material, an oscillating polarization is induced. As provided in several texts [70, 71], the functional relationship between the time-varying polarization $\boldsymbol{P}(t)$ and applied electric field $\boldsymbol{E}(t)$ can be mathematically written as:

$$P(t) = \varepsilon_0 \chi^{(1)} E(t) + \varepsilon_0 \left(\chi^{(2)} [E(t)]^2 + \chi^{(3)} [E(t)]^3 + ... \right) = P^L + P^{NL} \qquad (2.1)$$

where, ε_0 is the free space permittivity, and $\chi^{(m)}$ is the m^{th} order susceptibility tensor. The first term of the expansion is the linear polarization term which is responsible for linear phenomenon in the material such as the linear refractive index. The linear polarization oscillates at the same frequency of the applied electric field. The second- or higher-order terms in the series give rise to

nonlinear effects which make the generated polarization contain frequencies other than the input field frequency. This leads to several nonlinear phenomena such as second harmonic generation and third harmonic generation, depending on the second- and third-order susceptibility tensor involved, respectively. In this dissertation, the focus is on second-order nonlinear optical processes, hence the second-order tensor $\chi^{(2)}$ component is of interest. Second-order nonlinear optical interactions can take place only in material which do not exhibit inversion symmetry i.e. non-centrosymmetric crystals. $\chi^{(2)}$ is a third rank tensor and for a medium with loss and dispersion, it depends on the frequencies of the applied electromagnetic fields and also the generated frequencies. To get a better understanding of nature of frequency-dependent susceptibility tensor, the electric field vector of optical wave is represented as a sum over '*n*' number of frequency components

$$\tilde{E}(\vec{r},t) = \sum_n A(\omega_n).\exp(i(k_n.\vec{r} - \omega_n t)), \tag{2.2}$$

where $k_i = n(\omega_i)\omega_i / c$ is the wavenumber, $A(\omega_n)$ is slowly varying field amplitude, and the displacement vector $\vec{r}$ has three scalar components in *xyz* Cartesian coordinates. Using similar notation, the complex nonlinear polarization is represented as

$$\tilde{P}(\vec{r},t) = \sum_n P(\omega_n).\exp(i(k_n.\vec{r} - \omega_n t)), \tag{2.3}$$

where the summation extends over all frequency field components. The $\chi^{(2)}$ tensor components relate the nonlinear polarization to the product of field amplitudes according to the equation

$$P_i(\omega_n + \omega_m) = \varepsilon_0 \sum_{jk} \sum_{(nm)} \chi^{(2)}_{ijk}(\omega_n + \omega_m, \omega_n, \omega_m) E_j(\omega_n) E_k(\omega_m). \tag{2.4}$$

Each of the indices *ijk* refer to the Cartesian components *x*-*y*-*z* of the field polarizations. For summation over frequencies, the individual frequencies ω_n, ω_m can vary but their sum $\omega_n + \omega_m$ is kept fixed. To completely describe a three-wave interaction specified by Eq. 2.3, 12 $\chi^{(2)}$ tensors each having 27 Cartesian components, so as many as 324 elements must be known. Fortunately, a number of symmetry conditions reduce the number of independent components of the tensor. For example, for sum frequency generation of two input frequencies ω_1, ω_2 so that $\omega_3 = \omega_1 + \omega_2$, the nonlinear polarization is written as:

$$P_i(\omega_3) = \varepsilon_0 \sum_{jk} \left[\chi_{ijk}^{(2)}(\omega_3, \omega_1, \omega_2) E_j(\omega_1) E_k(\omega_2) + \chi_{ijk}^{(2)}(\omega_3, \omega_2, \omega_1) E_j(\omega_2) E_k(\omega_1) \right] \tag{2.5}$$

which reduces to

$$P_i(\omega_3) = 2\varepsilon_0 \sum_{jk} \left[\chi_{ijk}^{(2)}(\omega_3, \omega_1, \omega_2) E_j(\omega_1) E_k(\omega_2) \right] \tag{2.6}$$

due to the intrinsic permutation property of susceptibility tensor:

$$\chi_{ijk}^{(2)}(\omega_m + \omega_n, \omega_m, \omega_n) = \chi_{ikj}^{(2)}(\omega_m + \omega_n, \omega_n, \omega_m) \tag{2.7}$$

There are other symmetry conditions as well which simplify the tensor components:

(1) Real valued for a lossless media: $\chi_{ijk}^{(2)}(\omega_3, \omega_2, \omega_1) = \chi_{ikj}^{(2)*}(-\omega_3, -\omega_2, -\omega_1)$, implied by real fields, so only half of the tensor elements are independent.

(2) Overall permutation symmetry: $\chi_{ijk}^{(2)}(\omega_3, \omega_1, \omega_2) = \chi_{jki}^{(2)}(\omega_1, \omega_2, \omega_3)$ i.e. the indices can be interchanged when the corresponding frequencies are also changed. This occurs because the medium does not differentiate between applied and generated fields, the behavior depends only on the frequencies of mixing waves. This reduces number of independent components to 27.

(3) Kleinman symmetry: $\chi_{ijk}^{(2)}(\omega_3, \omega_1, \omega_2) = \chi_{jki}^{(2)}(\omega_3, \omega_1, \omega_2) = \chi_{kij}^{(2)}(\omega_3, \omega_1, \omega_2)$ when the frequencies being mixed lie sufficiently far from resonant frequencies of the nonlinear media, the susceptibility tensor components are not strongly dependent on frequency and thus the indices can be freely interchanged irrespective of the related frequencies.

(4) Spatial symmetry: The ordered state of a nonlinear crystal exhibits several symmetries such as rotation about an axis, mirror plane symmetry, etc. The incident fields will encounter similar atom arrangements under the effect of symmetry operations of the crystal. The corresponding $\chi^{(2)}$ tensor components can be shown to be related to each other thus reducing the independent count of the nonlinearity elements.

A contracted notation of the $\chi_{ijk}^{(2)}$ is used by replacing it with a *d*-coefficient in the case of SHG where the two input field frequencies are same, making the *j, k* indices interchangeable in $\chi_{ijk}^{(2)}(\omega_3, \omega_1, \omega_1)$ tensor. Thus the pair of *j, k* indices are replaced by a single index term *l* using the following convention:

jk:	11	22	33	23,32	13,31	12,21
l:	1	2	3	4	5	6

In the new notation, $d_{il} = \frac{1}{2}\chi^{(2)}_{ijk}$ and the Cartesian components of induced polarization for a SHG process are represented in frequency domain by

$$\begin{bmatrix} \tilde{P}_x^{(2\omega_1)} \\ \tilde{P}_y^{(2\omega_1)} \\ \tilde{P}_z^{(2\omega_1)} \end{bmatrix} = 2\varepsilon_0 \begin{bmatrix} d_{11} & d_{12} & d_{13} & d_{14} & d_{15} & d_{16} \\ d_{21} & d_{22} & d_{23} & d_{24} & d_{25} & d_{26} \\ d_{31} & d_{32} & d_{33} & d_{34} & d_{35} & d_{36} \end{bmatrix} \begin{bmatrix} \left(\tilde{E}_x^{(\omega_1)}\right)^2 \\ \left(\tilde{E}_y^{(\omega_1)}\right)^2 \\ \left(\tilde{E}_z^{(\omega_1)}\right)^2 \\ 2\tilde{E}_y^{(\omega_1)}\tilde{E}_z^{(\omega_1)} \\ 2\tilde{E}_x^{(\omega_1)}\tilde{E}_z^{(\omega_1)} \\ 2\tilde{E}_x^{(\omega_1)}\tilde{E}_y^{(\omega_1)} \end{bmatrix} \tag{2.8}$$

In this equation, the nonlinear *d*-coefficients are 18 in number for a crystal with least symmetries. If Kleinman symmetry condition is applied, the number of *d*-coefficients are reduced to 10 due to the equality relationships: $d_{14} = d_{25} = d_{36}$; $d_{12} = d_{26}$; $d_{13} = d_{35}$; $d_{15} = d_{31}$; $d_{16} = d_{21}$; $d_{23} = d_{34}$; $d_{24} = d_{32}$. In case of the spatial symmetries of crystal, the number of non-zero independent *d* coefficients decreases to even fewer number. For example, the *d-matrix* of a crystal of class 3m such as lithium niobate has only 3 non-zero distinct elements d_{31}, d_{33}, and d_{22} and the complete *d*-matrix is:

$$d_{il} = \begin{bmatrix} 0 & 0 & 0 & 0 & d_{31} & -d_{22} \\ -d_{22} & d_{22} & 0 & d_{31} & 0 & 0 \\ d_{31} & d_{31} & d_{33} & 0 & 0 & 0 \end{bmatrix}. \tag{2.9}$$

2.3 Phase matching

For efficient nonlinear frequency mixing processes, phase matching between the input and generated waves is required to coherently accumulate the output field over the medium length. Physically, it means that all the interacting waves travel with same phase velocity and the contribution to the second harmonic generated at each point in nonlinear medium adds up in phase with the contributions generated at any other point. This is difficult to achieve in general, as the medium offers dispersion so that waves at different frequencies experience different refractive indices leading to a difference in phase velocities. Considering the simplest three-wave

interaction case of second harmonic generation, the fundamental and second harmonic fields while traveling through a distance z in a $\chi^{(2)}$ medium, accumulate a phase of $\varphi_\omega(z) = k_\omega z = (\omega n_\omega/c)z$ and $\varphi_{2\omega}(z) = k_{2\omega}z = (2\omega n_{2\omega}/c)z$ respectively. The phase of the fundamental wave can exactly compensate for the difference with the second harmonic field at frequency 2ω when the refractive indices n_ω and $n_{2\omega}$ are equal so that the energy gets efficiently transferred to the generated optical wave. However, the difference in the phase velocities leads to a non-zero phase mismatch of $\Delta\varphi_{SH} = (k_{2\omega} - 2k_\omega)z$ which produces oscillations in the SH power. The maximum SH is achieved at an interaction length over which the phase mismatch becomes equal to π, defined as coherence length L_c:

$$L_c = \frac{\pi}{(k_{2\omega} - 2k_\omega)} = \frac{\lambda_{2\omega}}{2(n_{2\omega} - n_\omega)} \tag{2.10}$$

This coherence length is limited to a few microns in most nonlinear media which is insufficient for getting useful power levels of the SH field. This makes realizing phase matching very important. There are two different techniques called birefringent phase-matching and quasi-phase-matching, which have been extensively used to overcome the phase-mismatch problem.

2.3.1 Birefringent phase matching

The birefringent phase matching is made possible because the refractive index experienced by a wave in the medium depends on its polarization and propagation direction. Normally, high frequencies have higher refractive indices compared to the lower frequencies. If the interacting waves of different frequencies are polarized differently, their corresponding phase velocities can be equalized using birefringence to satisfy the phase matching condition. Keeping in mind material dispersion, the polarization of input and generated waves can be appropriately selected to achieve birefringent phase matching. The refractive indices for ordinary and extraordinary polarization are represented as n_o and n_e, respectively. For a negative uniaxial crystal ($n_e < n_o$) the high frequency wave should be polarized along the extraordinary axis and for a positive uniaxial crystal ($n_e > n_o$) the high frequency wave should be polarized along ordinary axis, to compensate for phase mismatch. There are certain limitations to using this approach for phase matching. In the polarization directions where the nonlinear interaction is phase matched, the nonlinear coefficient can be small or even zero. If the propagation is not along the principal axis of the crystal, there is loss of efficiency due to the walk-off experienced by the extraordinary

polarization. Moreover, the birefringent phase matching can only be employed for certain set of wavelengths decided by the dispersion curves of the nonlinear material.

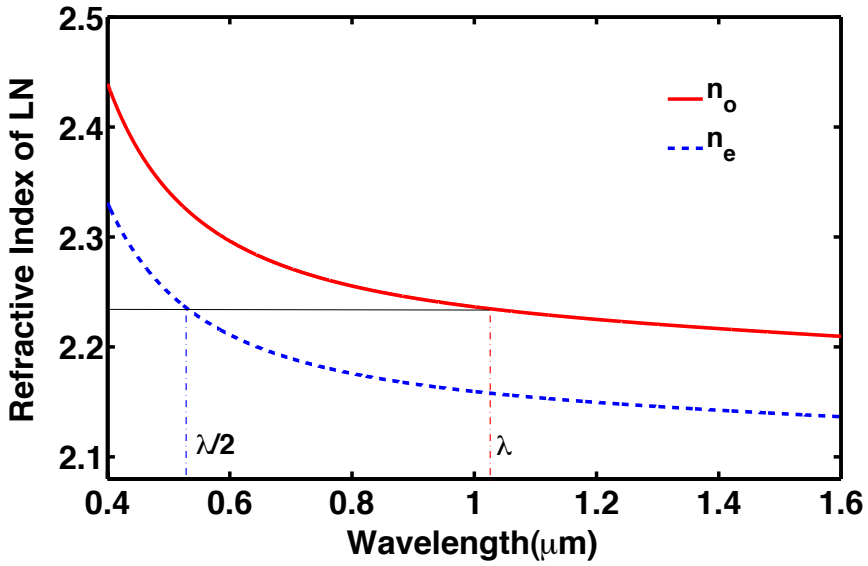

Figure 2-1: Dispersion curves for the ordinary n_o and extraordinary refractive index n_e of lithium niobate at room temperature.

Material dispersion in Lithium Niobate:

Lithium niobate is an example of a uniaxial birefringent crystal having an extraordinary refractive index n_e less than the ordinary refractive index n_o. These refractive indices depend on the incident wavelength and the temperature of the crystal, given by the following Sellmeier equations [72].

$$n_o^2 = 4.9048 + \frac{0.11775 + 2.2314\times10^{-8}F}{\lambda^2 - (0.21802 - 42.9671\times10^{-8}F)^2} + 2.1429\times10^{-8}F - 0.027153\lambda^2$$

$$n_e^2 = 5.35583 + 4.629\times10^{-7}F + \frac{0.100473 + 3.862\times10^{-8}F}{\lambda^2 - (0.20692 - 0.89\times10^{-8}F)^2} + \frac{100 + 2.657\times10^{-5}F}{\lambda^2 - (11.34927)^2} - 1.5334\times10^{-2}\lambda^2 \quad (2.11)$$

where the dependence on temperature T is given by $F = (T\text{-}24.5)(T\text{+}570.82)$.

The dispersion curves for the ordinary and extra-ordinary refractive indices for lithium niobate at room temperature T=25 are shown in Figure 2-1. Here the red curve corresponds to the ordinary refractive index and blue dashed trace for the extraordinary refractive index. For a particular set of FH wavelengths with ordinary polarizations and SH wavelengths with extraordinary polarizations, shown by λ and $\lambda/2$ in Figure 2-1, the two refractive indices happen to be equal which implies that birefringence phase matching can be used to generate an efficient second harmonic in lithium niobate. The phase matching wavelength can be slightly adjusted by doping to alter the refractive index, varying the temperature or launching the pump laser at an angle with the crystal axis [9, 73, 74].

The phase matching for three wave interaction in nonlinear crystals can be classified into three different types. Type I phase matching refers to the case when the two fundamental frequencies are of the same polarization and the generated frequency is of orthogonal polarization. In negative uniaxial crystals this is possible for the input frequencies having ordinary polarization and the sum frequency with extraordinary polarization. Second type of phase matching known as type II requires less birefringence to phase-match and is such that the two lower frequencies are orthogonally polarized, and generated wave along one of the two polarization states. The third type of interaction known as type-0 phase matching involves all three waves with same polarization. Type-0 phase matching can not be produced in an as-grown nonlinear crystal and requires engineering of the nonlinearity profile, as discussed in the following section.

2.3.2 Quasi-phase matching

The conventional phase matching technique based on birefringence suffers many drawbacks. Its strong dependence on material properties requires a specific combination of temperature and wavelength for phase matching. Also there is restriction on the components of nonlinear susceptibility tensor to only those elements which couple orthogonally polarized modes. Quasi-phase matching (QPM) is an alternative of birefringent phase matching and extends the capability of a nonlinear medium for wavelength conversion at *any* frequency in its transparency window using the highest nonlinearity tensor component. QPM is desirable for harmonic generation as it allows for non-critical phase matching and also eliminates the Poynting vector walk off. Feng *et. al.* (in 1980) first demonstrated the alternating nonlinearity in a single crystal of lithium niobate [75]. This is based on inverting the sign of nonlinearity after each coherence length to

compensate for the accumulated phase mismatch between the interacting waves. The periodic phase correction obtained by the artificial engineering of the nonlinearity causes the SH power to build up in a stepwise fashion, as illustrated by green trace in Figure 2-2. The quadratic growth shown as the blue dash-dotted line and the oscillatory red-dashed trace correspond to the phase-matched and phase-mismatched case, respectively.

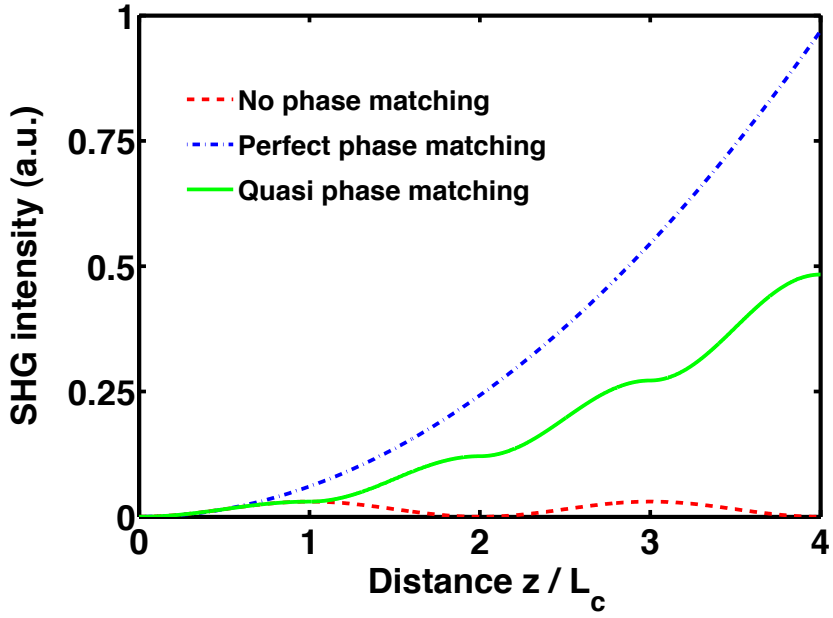

Figure 2-2: Spatial variation of SHG intensity for three different phase matching conditions. (a) Perfectly phase matched interaction grows quadratically shown by blue dash-dotted trace. (b) The red dashed curve shows oscillatory transfer of power to SH in a phase-mismatched case. (c) Growth of SH power in steps achieved by quasi-phase-matching is shown by green trace. Here L_c is the coherence length of the nonlinear crystal.

Even though the increase in the SH power seems less steep than the birefringent phase matched case of blue trace, QPM turns out to be more advantageous since it uses the largest nonlinearity coefficient which is not permitted in birefringent phase matching.

The modulation of the effective nonlinearity tensor component $d(z)$ is known as "QPM grating" and can be described by a rectangular wave in space with a period Λ and magnitude ± 1. In Fourier domain, this wave has frequency components at all harmonics of the fundamental grating vector $k = 2\pi / \Lambda$ and the series is represented as:

$$d(z) = d_{eff} \sum_{m=-\infty}^{\infty} G_m \exp(iK_m z) \tag{2.12}$$

where $K_m = \frac{2\pi m}{\Lambda}$ is the magnitude of grating wave vector of m^{th} order harmonic, d_{eff} is the magnitude of the nonlinearity tensor component responsible for the QPM interaction. The coefficients G_{m} for the duty ratio D takes the form

$$G_m = \frac{2}{\pi m} \sin(m\pi D) \tag{2.13}$$

Any harmonic of the grating vector can be used for achieving phase matching, however, the strongest nonlinear interaction is via the nonlinearity $d_Q = (2/\pi) d_{eff}$ for m=1 and optimum duty cycle D=1. The phase matching condition for the first order QPM is $\Delta k_Q = k_1 + k_2 - k_3 - 2\pi/\Lambda$. While each of the type-0, type-I and type-II phase matching is possible using QPM technique, the most advantageous for lithium niobate is type-0 QPM as the d_{33} nonlinear coefficient offers the highest conversion efficiency.

2.4 Coupled nonlinear equations

The wave equation for a nonlinear medium derived from Maxwell's equations is:

$$\nabla^2 \vec{E} + \varepsilon_0 \varepsilon_r \mu_0 \frac{\partial^2 \vec{E}}{\partial t^2} = \mu_0 \frac{\partial^2 \vec{P}_{NL}}{\partial t^2} \tag{2.14}$$

where μ_0 is the vacuum permeability, ε_0 is free space permittivity and $\varepsilon_r = 1 - \chi_0$ is the relative permittivity. The nonlinear polarization $\vec{P}_{NL}$ is the driving term for generation of new frequencies depending on the non-zero susceptibility tensor components, as discussed in the previous section.

For a second order interaction involving three monochromatic plane waves propagating along the z direction in a lossless medium, the form of the electric field and nonlinear polarization is inserted in (2.14) from (2.1) and (2.8). The solution of the nonlinear equation considering a "slowly varying envelope approximation" (SVEA) leads to a set of three first order coupled differential equations for the three interacting field amplitudes:

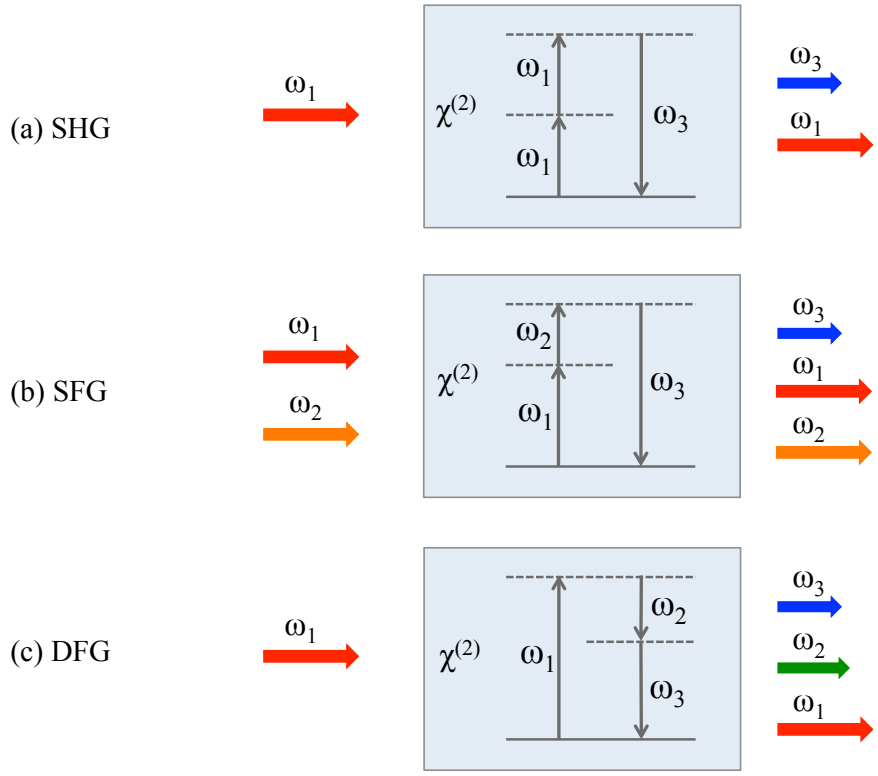

Figure 2-3: Schematic of different second order nonlinear processes: (a) SHG- second harmonic generation, (b) SFG- sum frequency generation, and (c) DFG- difference frequency generation.

$$\begin{aligned}
\frac{dA_1}{dz} &= -\frac{2i\omega_1}{n_1 c} d_{eff} A_3 A_2^* e^{-i\Delta kz} \\
\frac{dA_2}{dz} &= -\frac{2i\omega_2}{n_2 c} d_{eff} A_3 A_1^* e^{-i\Delta kz} \\
\frac{dA_3}{dz} &= -\frac{2i\omega_3}{n_3 c} d_{eff} A_1 A_2 e^{i\Delta kz}
\end{aligned} \tag{2.15}$$

where $\Delta k = k_1 + k_2 - k_3$ The effective nonlinear coefficient d_{eff} is obtained from the d-matrix of Eq. (2.9). As described in Figure 2-3, three kinds of interactions are studied in this dissertation: second harmonic generation (SHG), sum frequency generation (SFG) and difference frequency generation (DFG).

2.5 Second Harmonic Generation

The most common nonlinear process involving the interaction of three electromagnetic waves is second harmonic generation (SHG) when the two incident photons of same frequency ω_1 generate a frequency $2\omega_1$. This process is described schematically in Figure 2-3(a). For SHG, the set of coupled nonlinear equations are reduced to two equations:

$$\frac{dA_1}{dz} = -\frac{2i\omega_1}{n_1 c} d_{eff} A_3 A_1^* e^{-i\Delta kz} \qquad (2.16\text{ a})$$

$$\frac{dA_3}{dz} = -\frac{2i\omega_3}{n_3 c} d_{eff} |A_1|^2 e^{i\Delta kz} \qquad (2.16\text{ b})$$

where, A_1 is the input pump and A_3 is the SH output amplitude. To study the SH nonlinear interaction, these coupled equations are solved for low conversion efficiency limit and high conversion efficiency limit.

2.5.1 Non depleting pump case

In the low conversion efficiency case, the pump amplitude A_1 can be taken to be constant. In that approximation, the Eq. (2.16 b) can be integrated over z to obtain the SH amplitude A_3 at

$$A_3(L) = -\int_0^L \frac{2i\omega_3}{n_3 c} d_{eff} |A_1|^2 e^{i\Delta kz} dz = -\frac{2i\omega_3}{n_3 c} d_{eff} |A_1|^2 \left(\frac{e^{i\Delta kL} - 1}{i\Delta k} \right) \qquad (2.17)$$

Knowing the amplitude, the intensity is then calculated by the relation: $I = 2n_3 \varepsilon_0 c |A|^2$,

$$I_3 = \frac{2\omega_3^2 d_{eff}^2}{\varepsilon_0 n_1^2 n_3 c_0^3} I_1^2 \left| \frac{e^{i\Delta kL} - 1}{i\Delta k} \right|^2 = \frac{2\omega_3^2 d_{eff}^2}{\varepsilon_0 n_1^2 n_3 c_0^3} I_1^2 L^2 \, sinc^2 \left(\frac{\Delta kL}{2} \right) \qquad (2.18)$$

where Δk is the phase mismatch term. In case of circular FH and SH beams of spot size W_1 and W_3 respectively, the power can be obtained from intensity as:

$$P_3 = I_3 \pi W_3^2 = \frac{2\omega_3^2 d_{eff}^2 L^2}{\pi \varepsilon_0 n_1^2 n_3 c_0^3} \frac{W_3^2}{W_1^4} P_1^2 \, sinc^2 \left(\frac{\Delta kL}{2} \right) \qquad (2.19)$$

This approximation is accurate for conversion efficiencies upto ~10% [70]. It is apparent from this relation that the generated SH power is proportional to square of input pump power and square of length of the medium. The argument of *sinc* function shows that the SH power also

depends on the total phase mismatch ΔkL between the two waves. The effect of the phase term is illustrated by the Figure 2-4 which plots the SH power variation with the de-phasing term showing the importance of close to perfect phase matching necessary to attain efficient SHG. The efficiency decreases as the phase mismatch term ΔkL increases. Likewise, as the source wavelength shifts from the phase matching wavelength, the output falls drastically following a $sinc^2$ curve, with some oscillating side bands of low efficiency.

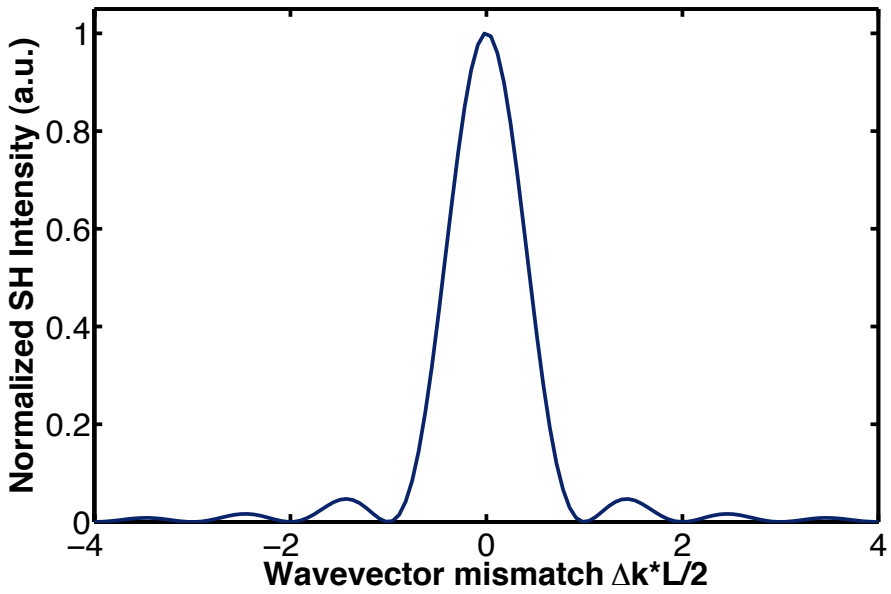

Figure 2-4: Effects of wavevector mismatch on the efficiency of SHG.

For a perfect phase-matching, $\Delta k = 0$ and the SH power increases quadratically with the length of the crystal. The spatial variation of the field intensity of generated wave in phase-matched case is demonstrated in Figure 2-2 by blue dash-dotted curve. If the SH process is not phase-matched, there is a periodic transfer of power between the driving nonlinear polarization and the generated second harmonic. The length over which the two waves remain in phase is known as the coherence length, defined as $L_c = \pi / \Delta k$. After this length the reverse power transfer begins. Therefore in case of phase mismatch, the efficiency of SHG oscillates along the propagation distance with a period twice of coherence build up length L_c. This is demonstrated by the red-dashed trace in Figure 2-2. To overcome this phase mismatch condition, birefringent phase-

matching or quasi-phase matching technique discussed in section 2.3 must be applied. In the QPM technique, just as the phase difference tries to reach π, the sign of nonlinear coefficient is reversed in nonlinear materials with ferroelectric properties. The process of polarity reversal is known as poling. The nonlinearity coefficient is thus not a constant, but allowed to vary with distance as *d(z)*. The coupled equations for quasi phase matching remains the same, except with a modified value of nonlinear coupling coefficient d_Q and wave-vector mismatch $\Delta k_Q = 2k_1 - k_3 - 2\pi m/\Lambda$, where Λ being the poling period for QPM. The grating wave-vector nulls the wave-vector mismatch and the QPM condition is satisfied. For quasi phase matched m^{th} order interaction, the effective nonlinear coefficient becomes $d_Q = (2/m\pi)d_{eff}$. The largest nonlinear coefficient for lithium niobate (LN), d_{33} = 27 pm/V gives an effective nonlinear coefficient for QPM, d_Q = 17.2 pm/V, which is 3.5 times larger than the nonlinear coefficient d_{31} (4.9 pm/V) for birefringence phase matching in LN. The simulations for uniformly poled QPM crystal is similar except that instead of using two different refractive indices for the calculations, only the extraordinary refractive index coefficient is used and the component of nonlinear coefficient tensor used is d_{11} or d_{22} and in LN crystals, d_{33}.

2.5.2 Pump-depleting case

According to the Eq. 2.19 the SH intensity grows as square of pump intensity. The quadratic intensity variation plot doesn't stop the efficiency to go beyond 100%, which is not in agreement with the energy conservation law and the condition of a constant input pump no longer holds true. Therefore at higher pump powers, fundamental pump power depletion which occurs along the length of the nonlinear material by transferring the power to second harmonic, is considered to solve the coupled equations of (2.16). In the high-conversion limit, the coupled equations are represented in normalized coordinates as [5]:

$$\frac{du_1}{d\zeta} = -2u_1u_3$$
$$\frac{du_3}{d\zeta} = u_1^2 \qquad (2.20)$$

The solution to the above set of equations gives the depleted pump and SH amplitudes as:

$$u_1(\zeta) = u_1(0)\sec h\left[\sqrt{2}u_1(0)\zeta\right]$$
$$u_3(\zeta) = \frac{1}{\sqrt{2}}u_1(0)\tanh\left[\sqrt{2}u_1(0)\zeta\right] \qquad (2.21)$$

The SH power is calculated from the amplitude u_3 following a similar treatment of pump non-depleting case which gives:

$$P_3 = P_1\tanh^2\left(\frac{\sqrt{2}\omega_1 d_{eff}\left(P_1/W_1^2\right)}{\varepsilon_0 n_1^2 n_3 c^3}L\right) = P_1\tanh^2\left(\Gamma L\right) \qquad (2.22)$$

When the conversion efficiency is low, $\tanh^2(\Gamma L) \approx \Gamma^2 L^2$ and Eq. (2.18) reduces to the SH power in Eq. 2.19 for the non- depleted pump case.

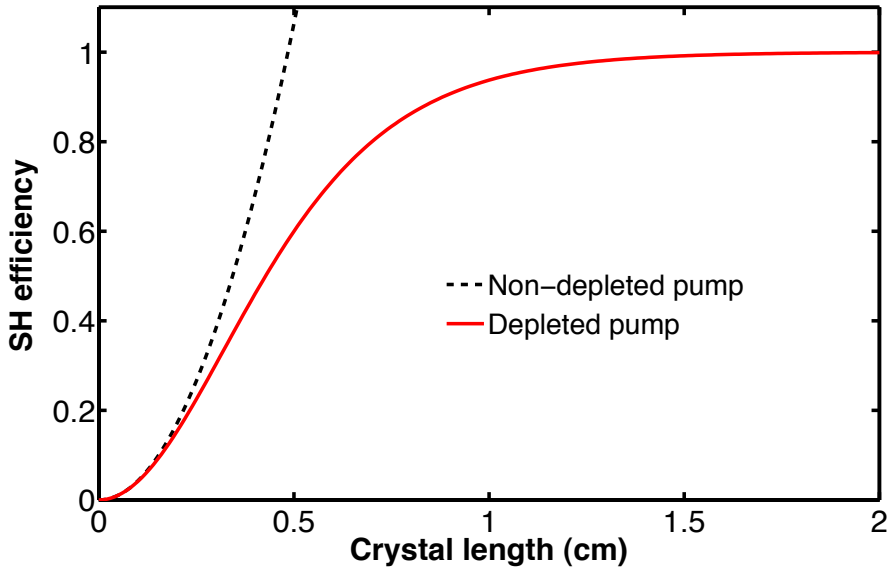

Figure 2-5: Theoretically calculated second-harmonic efficiency variation with the crystal length. The quadratically varying dashed curve shows the "no depletion" approximation while the red solid curve asymptotically reaching 100% efficiency in the "pump depleted" case.

The theoretical simulation of variation of SH efficiency with the input intensity in the pump non-depleting and depleting case is shown in the Figure 2-5. As expected, the conversion efficiency in pump depletion case can not exceed 1. It can be inferred from this figure that the non depleted

pump applies only till 10% efficiency, beyond which the pump-depletion effect must be considered.

2.5 Sum frequency generation

Schematic of a sum frequency generation interaction is shown in Figure 2-3(b) which involves the generation of a photon with frequency ω_3 by combining two lower frequencies, ω_1 and ω_2 where $\omega_3 = \omega_1 + \omega_2$. The SFG is advantageous to obtain a tunable source in the ultraviolet region by mixing a fixed wavelength visible pump and a wavelength-tunable visible laser used as a second pump [45]. The expression for the nonlinear polarization driving this process is written using Eq. (2.4)

$$P(\omega_1 + \omega_2) = 2\varepsilon_0 \chi^{(2)} E_1 E_2 \tag{2.23}$$

The derivation of conversion efficiency of a SFG process is done by solving the set of three coupled equations (2.15) in the non-degenerate case. Considering no depletion of the pumps, the SF intensity in the low conversion limit is obtained as:

$$I_3(L) = \frac{2\omega_3^2 d_{eff}^2}{\varepsilon_0 n_1 n_2 n_3 c_0^3} I_1(0) I_2(0) L^2 \sin c^2\left(\frac{\Delta kL}{2}\right) \tag{2.24}$$

where $\Delta k = k_1 + k_2 - k_3 - 2\pi/\Lambda$ is the phase mismatch between the pump frequencies and generated sum frequency wave. The complete solution of the coupled equations for SFG, as provided in ref. [5], takes the form of a Jacobian-elliptic function.

2.6 Difference frequency generation

The output frequency of a difference frequency mixing process is the difference of the two input frequencies so that the driving polarization is given by

$$P(\omega_1 - \omega_2) = 2\varepsilon_0 \chi^{(2)} E_1 E_2^* \tag{2.25}$$

As seen in the photon energy-diagram for DFG process in Figure 2-3(c), a photon at difference frequency $\omega_3 = \omega_1 - \omega_2$ is created by the destruction of a photon at ω_1 and the creation of another photon at lower frequency ω_2.

The coupled nonlinear equations for DFG process are:

$$\frac{dA_1}{dz} = -\frac{2i\omega_1}{n_1 c} d_{eff} A_3 A_2 e^{-i\Delta kz}$$
$$\frac{dA_2}{dz} = -\frac{2i\omega_2}{n_2 c} d_{eff} A_3^* A_1 e^{i\Delta kz} \qquad (2.26)$$
$$\frac{dA_3}{dz} = -\frac{2i\omega_3}{n_3 c} d_{eff} A_1 A_2^* e^{i\Delta kz}$$

where the wavenumber mismatch is given by the expression, $\Delta k = k_1 - k_2 - k_3 - 2\pi / \Lambda$.

The DFG process is also known as a parametric amplification process due to amplification of one of the input frequencies while emitting the difference frequency. The solution of the nonlinear coupled equations solved for constant pump amplitude, results in monotonically increasing amplitudes of the difference frequency and the amplified input field. The following expression is obtained for the DF with a constant signal and an undepleted pump:

$$I_3^{DF}(L) = \eta_{norm}^{DF} I_1(0) I_2(0) L^2 \sin c^2 \left(\frac{\Delta kl}{2} \right) \qquad (2.27)$$

where the factor η depends on the effective nonlinearity, interacting wavelengths and the refractive indices of the medium at various wavelengths. Each of the second-order nonlinear processes described here, involve two input photons and one output frequency, but the dominating interaction is decided by the phase matching conditions which are different for each process.

The quasi-phase matched DFG based nonlinear device such as PPLN has been extensively employed as a wavelength converter for optical telecommunication wavelengths by inputting a pump at wavelength λ_p in the 775nm range and signal wavelength λ_s in 1550nm range [40, 41]. The idler wavelength λ_i generated by DF mixing has wavelength lying in the 1550 nm waveband, symmetrically opposite in frequency to the signal with respect to the pump frequency.

2.7 Cascaded second order nonlinear optical conversion

The DFG based wavelength conversion involves the pump and signal wavelengths in different wavelength regions. Due to the mode-mismatch, it is difficult to efficiently couple them together into a guided wave PPLN device. The use of a cascaded second-order interaction namely

SHG/DFG was proposed to overcome this problem [76, 77]. In such a process, described schematically in the Figure 2-6(a), the pump wave (ω_p, λ_p) and the signal wave (ω_s, λ_s) are both located in the 1550 nm band. The pump first generates a SH at frequency $2\omega_p$ which interacts with the signal wave via a DF process to generate the idler wave at $\omega_i = 2\omega_p - \omega_s$. Due to the wide bandwidth of a DFG process, the process phase matched for SHG is also automatically phase matched for the cascaded SHG+DFG process. The same band wavelength conversion is a more practical approach as it allows use of the erbium doped fiber amplifier and lasers, specially developed for optical communications, to act as the strong input pumps.

In cSHG/DFG the small acceptance bandwidth for SHG, defined by the QPM condition, restricts the fundamental wavelength tolerance, it is difficult to implement broadband wavelength conversion. Since the pump is located within the 1.55 μm wavelength range, several channels remain unavailable for idler positioning. To overcome this restriction, in recent years waveband conversion has also been demonstrated by cascaded SFG/DFG process in quasi-phase-matched LN waveguides in which the pumps can be positioned outside the 1.55 μm spectral window of optical communication band [78]. As illustrated in Figure 2-6(b), the two pump frequencies ω_{p1} and ω_{p2} combine to generate a sum frequency wave at $\omega_{p1} + \omega_{p2}$, which in turn mixes with the signal frequency ω_s in a difference frequency process to create the converted signal (idler) at frequency $\omega_i = \omega_{p1} + \omega_{p2} - \omega_S$. The corresponding phase mismatch terms of SFG and DFG process are given by $\Delta k_{SF} = k_{p1} + k_{p2} - k_{SF} - 2\pi / \Lambda$, and $\Delta k_{SF} = k_{SF} - k_S - k_i - 2\pi / \Lambda$, respectively, where k_{p1}, k_{p2}, k_{SF}, k_S, and k_i are the propagation constants of the first and second pumps, sum frequency, signal and converted signal (idler) waves and Λ is the QPM period. The nonlinear coupled equations for the cascaded SFG/DFG process can be written as [44]:

$$\frac{dA_{p1}}{dz} = -\frac{2i\omega_{p1}}{n_{p1}c} d_{eff} A_{SF} A_{p2}^{*} e^{-i\Delta k_{SF} z},$$
$$\frac{dA_{p2}}{dz} = -\frac{2i\omega_{p2}}{n_{p2}c} d_{eff} A_{SF} A_{p1}^{*} e^{-i\Delta k_{SF} z},$$
$$\frac{dA_{SF}}{dz} = -\frac{2i\omega_{SF}}{n_{SF}c} d_{eff} A_{p1} A_{p2} e^{i\Delta k_{SF} z} - \frac{2i\omega_{SF}}{n_{SF}c} d_{eff} A_{S} A_{i}\, e^{i\Delta k_{SF} z},$$
$$\frac{dA_{S}}{dz} = -\frac{2i\omega_{S}}{n_{S}c} d_{eff} A_{SF} A_{i}^{*} e^{i\Delta k_{DF} z}, and \qquad (2.28)$$
$$\frac{dA_{i}}{dz} = -\frac{2i\omega_{i}}{n_{i}c} d_{eff} A_{SF} A_{i}^{*} e^{i\Delta k_{DF} z}.$$

Here, (A_{p1}, n_{p1}), (A_{p2}, n_{p2}), (A_{SF}, n_{SF}), (A_S, n_S), and (A_i, n_i) are the amplitudes and refractive indices of the medium at the first and second pumps, sum frequency, signal and converted signal (idler) waves, respectively. $d_{eff} = (2/\pi)d_{33}$ is the effective nonlinear coefficient of PPLN. For wavelength conversion based on the cascaded SHG/DFG process, the degenerate case of eq. (2.28) with $\omega_{p1} = \omega_{p2}$ is numerically solved.

The SFG/DFG based converters have found target applications in broadband wavelength conversion and multiple-channel wavelength conversion. Such converters are also advantageous due to their wider conversion bandwidth obtained by increasing the pump wavelength difference and being a suitable device to perform ultrafast optical signal processing in optical networks [43, 45, 79-81]. Wavelength conversion by cSFG/DFG in PPLN is greatly desirable to construct much more dynamic and flexible future optical networks. Various techniques including the use of pump detuning for uniform gratings and the use of fixed pumps for engineered QPM grating structures considering counterpropagating cascaded SFG/DFG have already been investigated, which offer advantages of flat and broad conversion bandwidth and higher efficiency for the same band wavelength conversion [82]. The wavelength converters based on cascaded SHG/DFG and SFG/DFG in PPLN are compact, have low signal-to-noise degradation and are transparent to bit rate and signal modulation formats, making them ideal choice for the future all-optical communication networks [60, 83, 84].

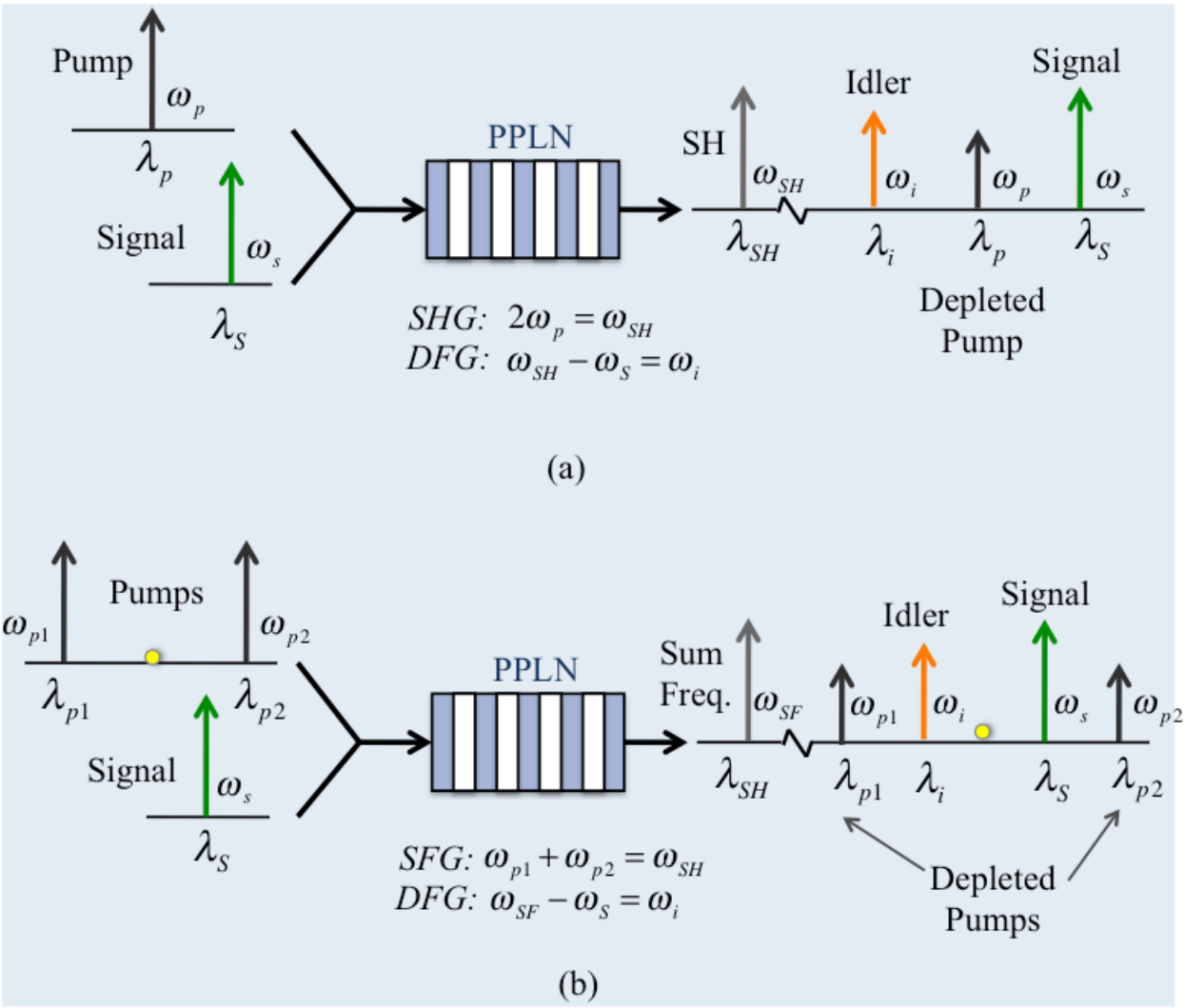

Figure 2-6: Wavelength conversion based on (a) cascaded SHG/DFG using one pump laser and (b) cascaded SFG/DFG employing two pump lasers.

Engineered Conversion Bandwidth: Chirped Gratings

By using the cSFG/DFG process, the limitation due to small tolerance in pump wavelength of a cSHG/DFG process is relaxed and the conversion bandwidth is further broadened by increasing the pump spacing [85]. However, the QPM bandwidth of a SFG process in PPLN is not sufficient to cover the entire C-band of optic communication which is required for tunable wavelength conversion and for wavelength multicasting. Therefore, using engineered QPM structures for

broadband SHG, the devices have been implemented for multichannel wavelength conversion wherein multiple pumps were simultaneously used to broadcast a signal to several idlers benefitting from a broad SH/SF bandwidth [51, 56, 86, 87].

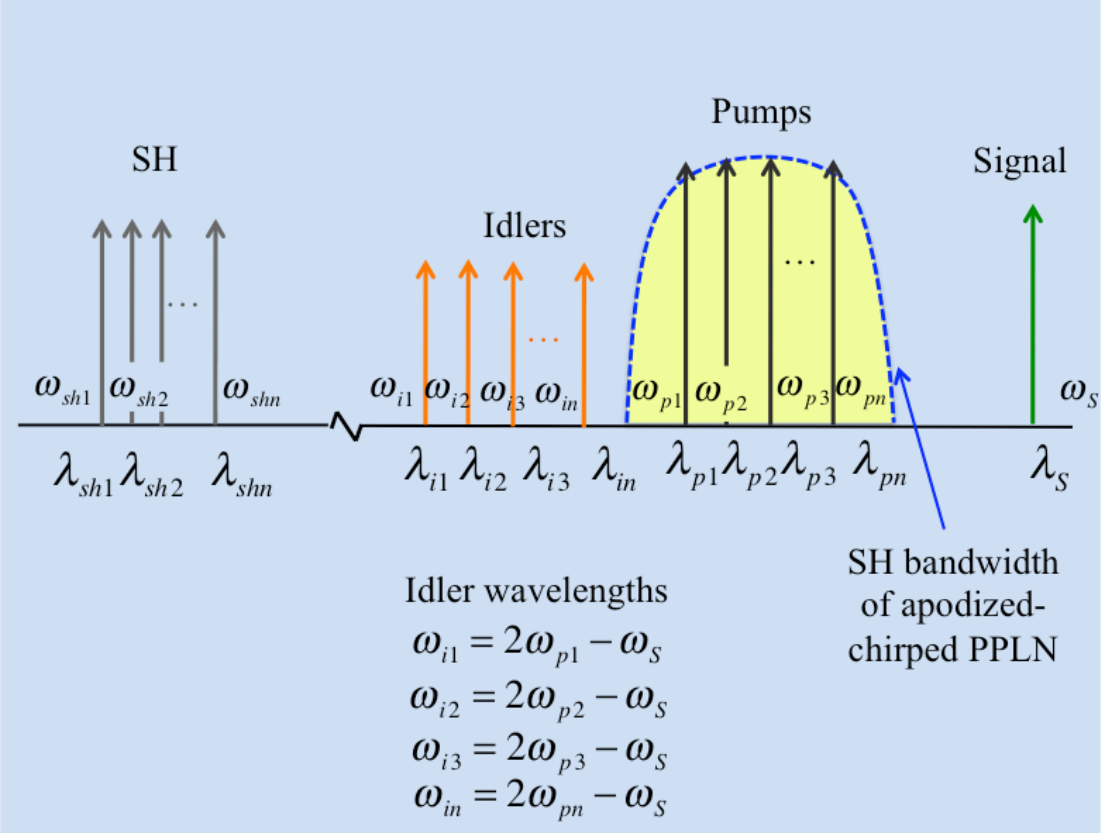

Figure 2-7: Multichannel wavelength broadcast scheme based on cascaded SHG/DFG process using multiple pumps in an engineered QPM device to perform simultaneous multiple SH generation for multiple pumps.

Inducing a chirp in the period of the nonlinear QPM structure broadens the SH-SF bandwidth, as different sections of the grating get phase matched to different wavelengths. The linear chirp requires very small changes in the grating period (nms) which are difficult to fabricate, therefore step changes in the period have been employed to obtain broad QPM bandwidth albeit with ripples in the response [88]. The apodization of the duty ratio in such step-chirped gratings have been proposed to flatten the efficiency response. The chirped or apodized step-chirped PPLN gratings provide flexibility of locating the pump wavelengths to generate idlers in a cSHG/DFG or cSFG/DFG process at desired wavelengths in the WDM grid for any fixed signal wavelength.

In the cSHG/DFG scheme, each of the multiple pump wavelengths generate a SH output and the signal mixes with the corresponding SHs to generate multiple DF outputs. The schematic of spectrum at the output end of the multichannel wavelength broadcast device is shown in the Figure 2-7. This is also beneficial for a variable-input variable-output wavelength conversion.

2.8 Conclusion

In this chapter, descriptions of nonlinear electric susceptibility and coupled-mode equations for second order nonlinear processes including SHG, SFG, and DFG and for cascaded wavelength conversion such as cSHG/DFG and cSFG/DFG were provided. The concepts of phase-matching and quasi-phase matching were discussed in the context of the three-wave interactions. While the implementation of DFG requires an out-of band pump (around 775 nm) for frequency mixing within the 1.5 μm band, the cascaded processes involving cSHG/DFG and cSFG/DFG allow pump wavelength(s) to remain within the communication band. The benefits of using an engineered chirped PPLN grating for tunable wavelength conversion and multichannel wavelength broadcast were also discussed.

CHAPTER 3
PERIODIC POLING OF LITHIUM NIOBATE

3.1 Overview

The presence of birefringence is a prerequisite for phase matching in nonlinear optical harmonic generation in naturally occurring nonlinear crystals [9]. However, some of the highly nonlinear materials, such as GaAs, are not birefringent or their refractive indices do not match for conversion at desired wavelengths. In this case, ferroelectric nonlinear materials such as potassium titanyl phosphate (KTP) or lithium niobate (LN) came out as the most promising candidates for frequency conversion applications, wherein the polarized nature of ferroelectrics allowed domain switching for quasi-phase matched optical frequency conversion [15]. The process of periodically inverting the orientation of domains in a material is called periodic poling. These nonlinear optical devices e.g. periodically poled lithium niobate (PPLN) require high precision fabrication techniques to attain domain structures with ~micron dimensions. Various methods have been used in the past for poling the nonlinear crystals which include domain inversion during crystal growth, chemical indiffusion with titanium on the surface, direct electron beam writing, electric field poling (EFP), UV assisted electric field poling etc. [89]. Amongst these techniques, room temperature EFP is the most convenient and least expensive as it does not need a specific environment or sophisticated equipment for high precision domain engineering. The speed of poling is also much faster in comparison with direct writing methods. The choice of material for poling depends on several factors like high nonlinearity, wide transparency range, and availability [14, 90]. In this dissertation, we have used lithium niobate because it satisfies the above criteria and is already popular in the telecom industry as electro-optic modulators. This chapter begins by explaining the underlying mechanism behind the ferroelectric domain switching with lithium niobate as an example. This is followed by a discussion on the poling technique used for making the PPLN crystals reported in this thesis. The detailed description of this process involves photolithographic imprinting of periodic gratings, employing an optimized high-voltage pulse shape, in-situ optical monitoring of the poling process using crossed-polarizers, and wet-etching of the surface a of poled crystal leading to a surface relief pattern [63, 91].

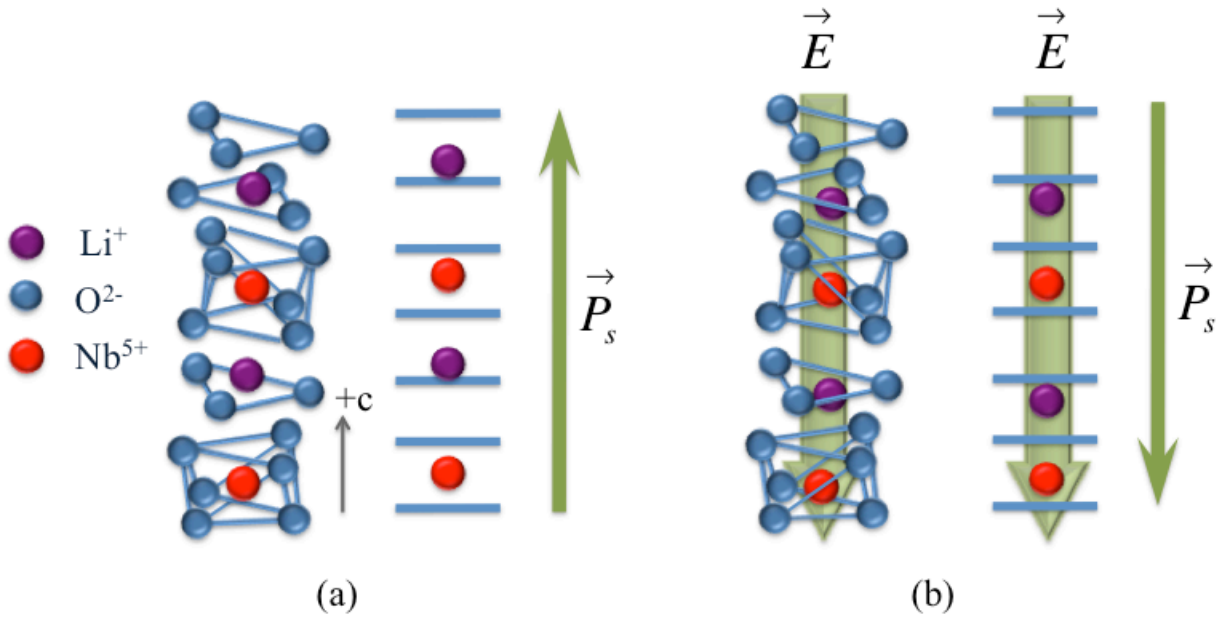

Figure 3-1: LiNbO3 in (a) as-grown state and (b) domain inverted

3.2 Lithium Niobate structure

Lithium Niobate has a trigonal crystal structure, lacks inversion symmetry and exhibits ferroelectricity, piezoelectric effect, pyroelectricity, negative uniaxial birefringence and nonlinear optical polarizability. Below its ferroelectric Curie temperature (1200 °C) [92], the structure of lithium niobate consists of planar sheets of oxygen in the form of distorted hexagonal closed packing [93, 94]. Two-third of the octahedral sites are equally filled with lithium and niobium cations and one-third of the lattice sites are vacant. In ferroelectric phase ($T<T_c$), the position of lithium atoms (violet spheres) and niobium atoms (red spheres) with respect to the oxygen octahedral and their location along the +c axis with respect to oxygen layers are shown in Figure 3-1(a). The crystal thus has a three fold rotation symmetry about its c-axis and additionally displays mirror symmetry about three planes at 60^o which classifies $LiNbO_3$ as a member of 3m point group and R3c space group. The positioning of the positive ions relative to oxygen planes gives rise to the internal dipole moment. The orientation of these dipoles can be inverted by making the positive ions cross the negative oxygen layers which requires applying high electric

fields along the c-axis, as can be seen in Figure 3-1(b). This can also be done at temperatures close to the curie point when $LiNbO_3$ reaches the paraelectric phase.

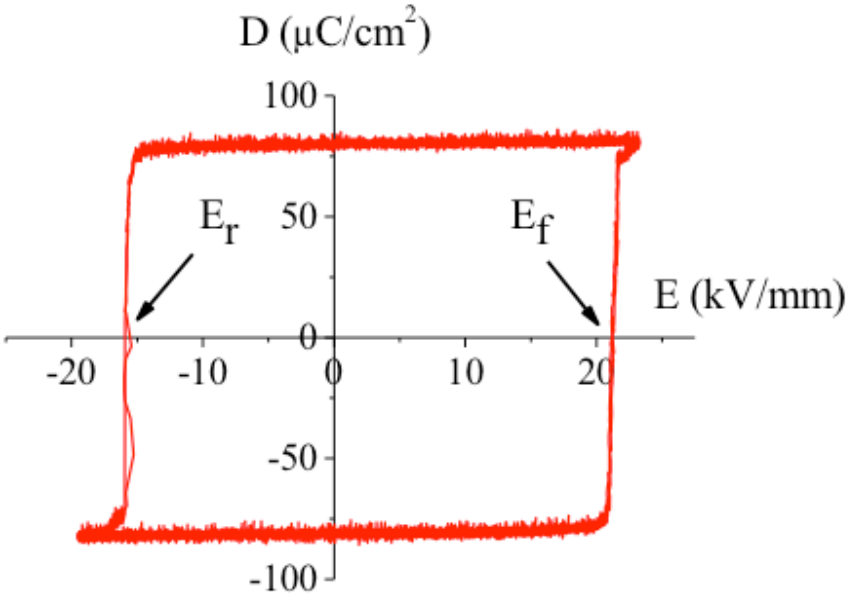

Figure 3-2: Ferroelectric hysteresis loop, D: displacement, E: applied electric field, E_f: coercive field, E_r: coercive field in the reverse direction. [96]

Determining the direction of c-axis to identify +z face for voltage application:

In the hexagonal unit cell of lithium niobate, the c-axis is defined as the axis along which the crystal exhibits 3-fold rotation symmetry (Proc. IRE 37, 1949) [95]. The polarity of the c-axis can be identified by compressing the crystal and the face which becomes negative upon compression is the +c direction. As an alternative, cooling the crystal will point the +c direction out of the face that becomes positive during the cooling process. This can be explained by considering of motion of Li and Nb ions in the oxygen octahedra. The ferroelectric or room temperature phase of lithium niobate is illustrated in Figure 3-1(a). Upon mechanical compression or heating, the ions move closer to the oxygen plane centers (paraelectric phase) thus reducing the net polarization. This leaves excess negative charge on +c face making it negative. On the other hand, cooling the crystal will pull the metal ions closer to the ferroelectric positions, further from the oxygen layer, thus increasing the net polarization. The +c face then becomes positively charged. This effect was

then used to identify the polarity of the LN crystal by blowing hot air on the crystal and checking the voltmeter deflection connected to its two surfaces.

3.3 Ferroelectric domain inversion

A ferroelectric material belongs to paraelectric family that shows a spontaneous electric polarization in the absence of a field and the direction of polarization can be switched by applying an external electric field. Ferroelectric materials are useful for achieving quasi-phase-matching by periodically reversing the direction of polarization. The behavior of a ferroelectric material changes to a paraelectric one, eliminating the spontaneous dipole moment, above a certain temperature known as the phase-transition or Curie temperature. The polarization in ferroelectrics also depends on the history of applied field and hence exhibit an hysteresis curve shown in Figure 3-2 [96]. Here, the term P_s refers to spontaneous polarization, P_r is remnant polarization and E_c is the value of the coercive field. P_r is always <= P_s in ferroelectric crystals. For commercially available $LiNbO_3$ wafers, which are supplied as single-domain crystals, the remnant polarization is equal to the spontaneous polarization.

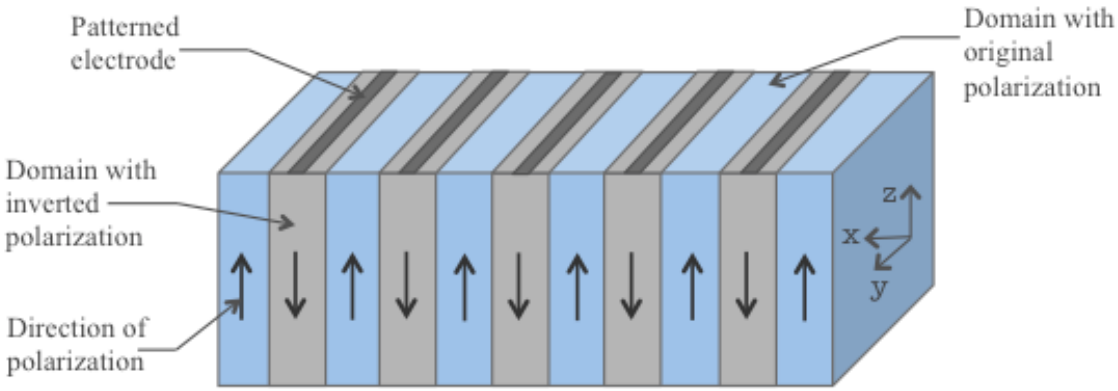

Figure 3-3: A model electric field periodically poled domain structure

The symmetry conditions in such inherent crystals create a polar axis leading to two- antiparallel directions of inbuilt polarization. Depending on the crystal structural configurations, usually ferroelectrics have two or more orientational states e.g. Barium titanate ($BaTiO_3$), has six equivalent axis of spontaneous polarization, whereas uniaxial crystals such as lithium tantalate $LiTaO_3$ and lithium niobate $LiNbO_3$ has two states of dipole orientation. By applying a field

higher than the coercive field the sense of dipole orientation can be switched from one to another. This fundamentally means displacement of positive and negative ions under the influence of an external field, as described in Figure 3-1. In this section, a description of the domain dynamics in ferroelectrics, in particular lithium niobate, under the effect of external field is given.

Model description of domain inversion:

The investigations on periodically poled $LiNbO_3$ crystals have led to a deeper understanding of physics behind the poling process. A typical periodically poled structure is schematically illustrated in Figure 3-3, where the domain walls are seen as straight lines parallel to the z-axis from electrode surface to the bulk of the crystal. The possible mechanism behind domain reversal is the growth of an existing domain by sideways domain wall motion or via a random nucleation of a new domain and its propagation in the polar direction. A phenomenological study of domain walls, also confirmed by experimental results has shown that the domains lying in the y-z symmetry planes and normal to the crystal x-axis are most energetically favorable [97]. Usually, the domains have larger width than the width of patterned electrodes indicating the presence of polarization charge in the insulated surface regions. This could be attributed to the partial screening of polarization charges that allow local electric fields to be high enough to reverse the polarization in the insulator coated regions. Further, the domains are centered under the electrodes, which indicates that the nucleation sites occur under the electrodes. There are however, intrinsic nucleation centers in the crystal leading to some defects in the domain patterning. The propagation velocity of domain walls is dependent on the average z-component of the electric field on the x-z cross section of domain [98]. Based on the previous studies, the mechanism of domain switching by the application of n external field can be explained in four stages shown in Figure 3-4:

(a) *Domain nucleation under the electrodes*

The formation of inverted domains due to the external fields is initiated by the nucleation sites under the electrodes, as shown in Figure 3-4(a). The nucleation sites are located on either face of the lithium niobate sample grouped in clusters with a typical density of 1000 nuclei/mm^2. The density of nucleation sites is strongly influenced by the choice of electrode (metal/liquid) and the electrode period. In case of liquid electrodes with a 10 μm period, the nucleation site density increases as much as 200 times compared to plain lithium niobate. At applied fields below the

coercive field, the nucleation site density is field- and time- dependent. The formation of domain nucleation sites has been a subject of numerous discussions and a classical model proposed by Landauer estimated enormously high values of energy required to form a critical nucleus in the case of $BaTiO_3$ [99]. This eliminates the possibility of nucleation by thermal fluctuations. It was thus assumed that certain centers exist in the crystal which trigger the nucleation by formation of unregulated micro- or nano-domains on the polar surfaces. The detection of such microstructure centers even in otherwise single-domain state of $LiNbO_3$ has proved this assumption right [100]. Spontaneous appearance of antiparallel domains on polar faces may be related to the high screening fields leading to partial polarization within the surface layer.

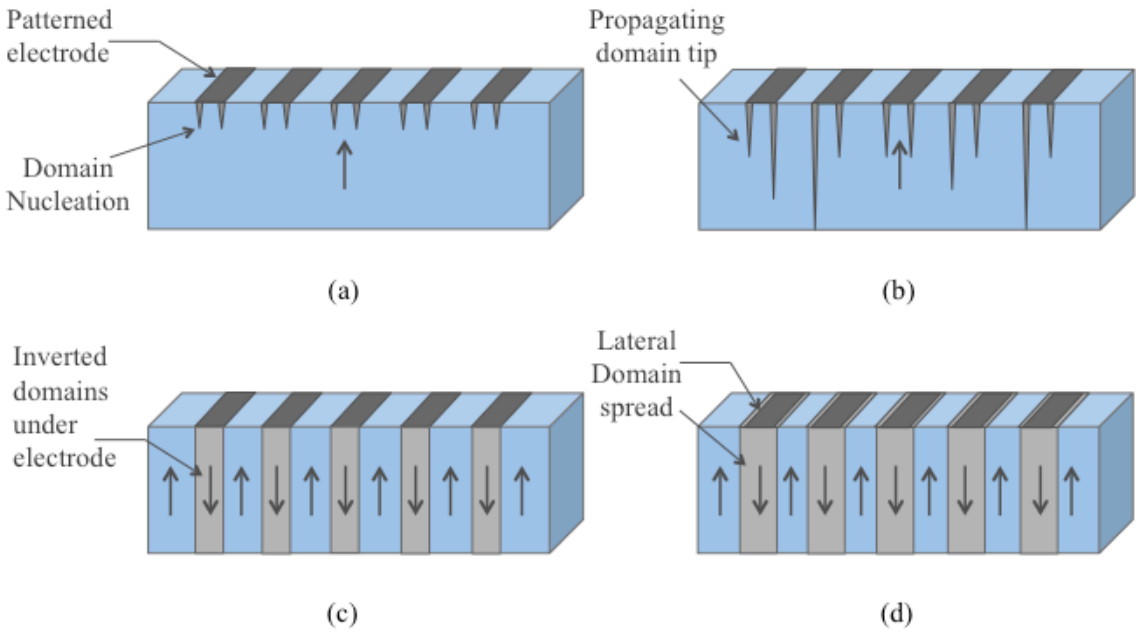

Figure 3-4: Various stages of domain kinetics during electric field poling process. (a) domain nucleation, (b) domain tip propagation, (c) domain coalescence and (d) domain wall lateral movement and stabilization.

(b) *Domain tip propagation along the direction of field*

A domain nucleus formed near the polar face of the lithium niobate can be represented as a six-walled pyramid with an hexagonal base and its apex just below the surface. The growth of domains begins when due to the external field the tip of domain nucleus starts propagating along

the polar axis towards the opposite face of the crystal, as described in Figure 3-4(b). The experimental study of relationship between velocity of tip and the applied field asserts that domain merging occurs during tip propagation stage when the tips under adjacent electrodes combine and form a single large domain [98, 101]. For crystals with high nucleation site densities, the merging takes place between tips which originate under the same electrode. However, in case of low density of nucleation sites, the closest tips are from separate electrode stripes, therefore merging results in larger domain size and reduction in the effective nonlinearity. Experiments have associated this to substrate inhomogeneity leading to errors in the fabrication period which reduces efficiency of the PPLN device [100]. Also the unscreened polarization charge on the walls of neighboring domain walls increases the electric field in regions between them leading to the merging of domain tips. When the tips of isolated domain reach the opposite face, the domain walls straighten out and terminate forming an hexagonal shape.

(c) *Coalescence of domains tending to a single-domain state*

The domain reversal completes at the termination stage when the close proximity tips originating under the same electrode merge as they reach the opposite electrode. At the subsequent stage, illustrated in Figure 3-4(c), a wider domain is rapidly formed by coalescence of the adjacent domains walls coming in direct contact with each other. This takes place on the *y* face of domains growing along the electrodes. During this process, the domain also starts to spreads out from under the electrode at the site where coalescence first began, resulting in duty cycle non-uniformity. This can be attributed to inadequate adhesion of resist on $LiNbO_3$ substrate, which can lead to some conduction between the photoresist and the surface of the $LiNbO_3$, allowing charge buildup and domain reversal.

(d) *Lateral movement of the domain walls*

The last stage of poling, just before the domains get stabilized, is the spreading of the domains out of the electrodes, as shown in Figure 3-4(d). Miller and Weinreich had proposed an on-wall nucleation mechanism for the sideways 180° domain wall motion in Barium Titanate [102]. According to their model, wall motion is a result of nucleation at the existing parent 180° domain walls, therefore the nucleation rate dictates the domain wall velocity. Experimental results at field values near the coercive strength, conform with the nucleation model which predicts that sideways domain velocity obeys an exponential law. The wall velocity dependence on field is

thus given by $\upsilon \propto \exp(-\delta / E)$ where, the activation field for sideward motion depends on electrode material, crystal thickness, temperature etc. [103, 104]. This dependence tends to take a power law form at very high fields. The exponential decreasing behavior can also be explained by screening of polarization charge. The domains tend to spread out under the electrodes but the unscreened spontaneous polarization charge on the crystal face lowers the average field near the propagating wall, which slows down its growth and prevents excessive spread of domains beyond the electrodes.

At this stage, the domains formed are unstable and exhibit a time-dependent coercive field [105]. If the external field is switched off immediately after polarization reversal, the domains can spontaneously revert back to their original orientation, the process is called 'backswitching'. The domain flip back usually occurs within ~60 ms, when the reverse coercive field decays from ~ -17.5 kV/mm to 0 kV/mm, as shown in hysteresis loop of lithium niobate in Figure 3-2. To prevent backswitching, a positive field greater than the reverse coercive strength (17.5 kV/mm) in the direction of the spontaneous polarization for a duration greater than 60 ms was applied in our poling experiments.

3.4 Liquid Electrode Poling Technique

Amongst several other methods tried for periodic domain switching, lithography based liquid electrode poling is most suitable for mass production at low cost of engineered gratings in lithium niobate. In this section, the steps followed for poling the LN samples are described in detail.

3.4.1 Photolithographic domain patterning

To prepare the PPLN samples mentioned in this dissertation, 0.5 mm thick optical grade LN wafers from Crystal Technology Inc. were purchased. The photolithographic printing of periodic and aperiodic gratings is done in six steps: cleaning, spin-coating, soft baking, mask exposure, development and hard baking. The whole process was carried out in a class-100 clean room facility of micro-fabrication laboratory at Polytechnique Montreal. The 3" LN wafers were first cut into four equal pieces on a dicing machine using diamond grit blades. To avoid the dust of LN sticking onto its surface during dicing, a layer of resist was coated on the wafers prior to dicing. These quarters of the full wafer were then used for the photolithography process, as described in Figure 3-5.

a. Cleaning Wafers

The first step in the photolithography process is cleaning the sample using a series of solvents in order to remove the grease, dirt or any other particles. To obtain good quality of photoresist layer it is essential to remove all the contamination from the surface of sample. The presence of large particles on the photoresist layer can also lead to defects in poling or even sample breakdown during the high voltage application. The LN sample was first put in Acetone for about 5 minutes, agitating constantly. This step removed most of the particles present on the sample. The sample was then transferred to a beaker containing isopropanol (IPA), which was constantly shaken for 5 minutes to remove the residue of Acetone. Finally running deionized (DI) water was used to remove the IPA from the sample. The sample was quickly dried by blowing dry N_2 so as not to leave any stains of evaporated solvents on it. Unlike silicon and other substrates, the LN sample was not put on a hot-plate for complete dehydration after chemical cleaning as it would further attract dirt or breakdown due to pyroelectric charge buildup.

b. Spin-coating Resist

After cleaning, a positive photoresist was coated on the +z face of the $LiNbO_3$ samples. The polarity of lithium niobate wafer was determined by applying pressure or heat on the crystal and monitoring the deflection of a multimeter, as described in section 3.2. It has been found that Shipley S1813 or AZ5214E are the most suitable photoresists for coating on lithium niobate. The cleaned sample was placed on the spin mount and an adhesive assistant HMDS was spin-coated before coating the photoresist as it facilitates in bonding the resist to LN to act as a good insulator during poling. The photoresist was then dropped carefully in the center without forming any bubbles to cover two-third of the sample. Spinning was done at a speed of 4000rpm for 30sec to get a uniform layer of 1.5 micron thickness. The presence of any particles would leave comets shaped pattern of the resist. These comets were eliminated by working in cleaner environments and by filtering coating solutions as part of the resist dispensing process. Also, eliminating wait time between cleaning and spin coating helped in preparing good samples.

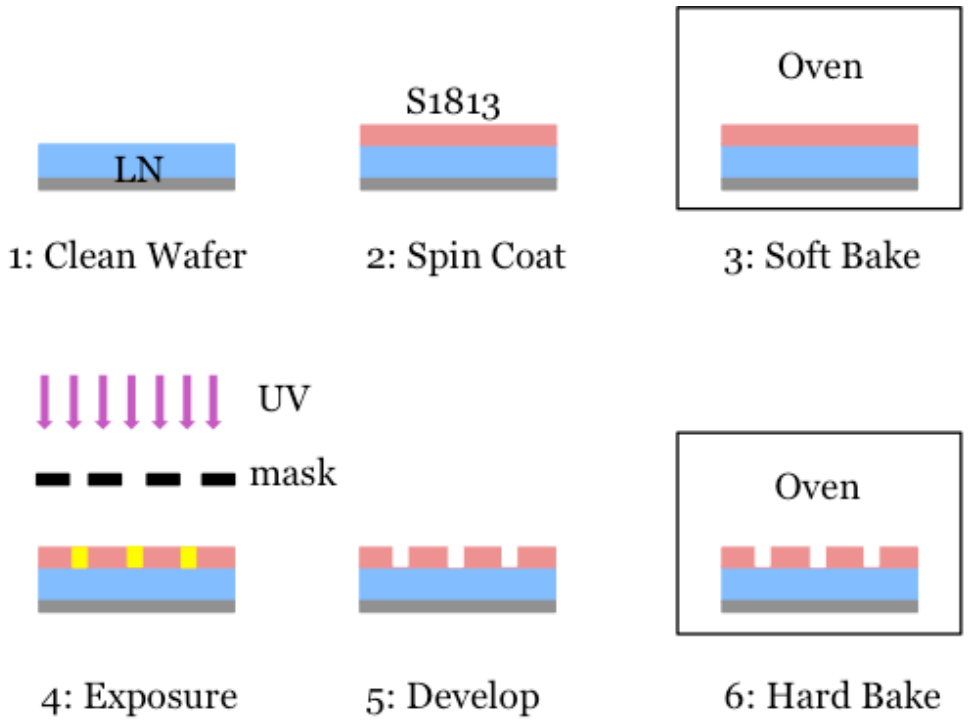

Figure 3-5: Schematic of photolithography process of LN

c. Soft baking

Soft baking is done to remove the solvents from the photoresist coating and prepare it for photo-imaging. Being pyroelectric, lithium niobate is highly sensitive to temperature change and starts cracking if kept on a hot-plate. The samples were thus placed in a cavity and baked in an oven. The cavity was made by using aluminum foil under the samples in a petri-dish, putting a metallic wire-mesh on top of the samples and by folding the foil around the edges. The sample was then put inside an oven set at room temperature in the beginning. The temperature was slowly increased at a ramp of 1°C /min to reach 90°C. The sample was then left for 30 minutes at 90°C and the oven was turned off afterwards. The oven cooled down in 1 hour, and then the door was slowly opened in steps to bring the oven temperature down to the room temperature. Soft baking is a critical step in obtaining good quality photolithography patterning. Over-soft-baking with higher temperature or spending more than 30 minutes in the oven degrades the photosensitivity of resists which reduces its developer solubility. In such cases, the sample could not be developed even after spending several minutes in the developer solution. Under-soft-baking solvents left in

the photoresist prevent light from reaching the sensitizer leaving the resist incompletely exposed. The sample is then readily attacked by the developer in both exposed and unexposed areas.

d. UV Exposure through periodic mask

One of the most important steps in the photolithography process is mask alignment and optimum exposure to UV radiation. A positive mask with the desired grating pattern was designed in an engineering drawing software Autosketch and fabricated at a laser machining facility in Polygrames research center at Ecole Polytechnique. In one mask, typically 6 channels of 2cm length and 2 mm width with similar periods were designed. The period of grating was calculated using the QPM condition for the desired conversion wavelength. To obtain a final 50:50 mark-space ratio (open area to covered area) on the periodically poled sample, the optimized ratio of mask in our process was 25:75. The ratio also depends on the grating profile and the UV exposure time.

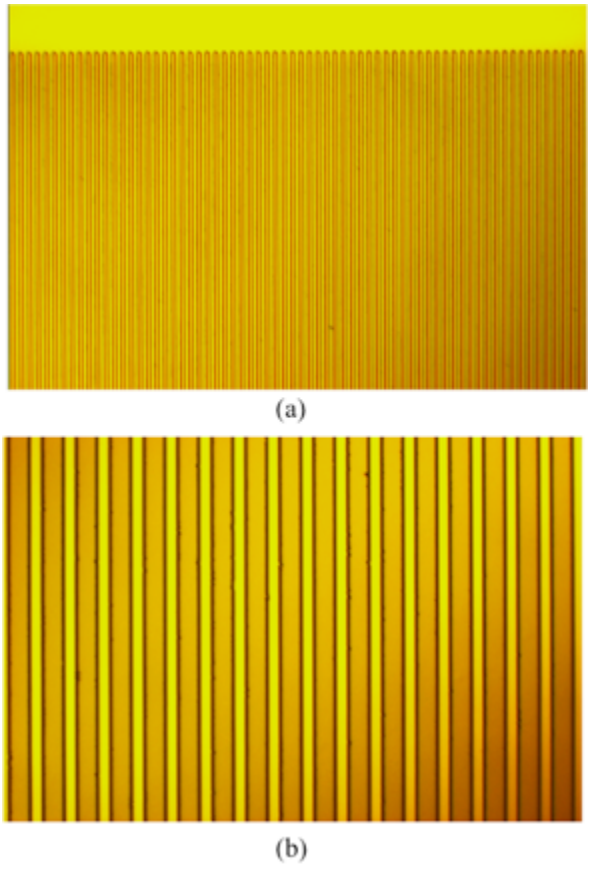

Figure 3-6: Microscopic images of photolithographic pattern on photoresist of period 18.6 microns after development.

As the LN domains tend to grow along the y-axis, the periodic mask was carefully aligned keeping the channels length along the x-cut of the wafer for transferring the pattern onto the resist coated $LiNbO_3$ wafer surface. We used Karl Suss MA4 photo-mask aligner, where the resist-coated wafer was brought into physical contact with the mask. The wafer was held on a vacuum chuck, and the whole assembly rises until the wafer and mask came in contact with each other. The photoresist was then exposed with a high intensity ultraviolet light through the pattern on the mask. Because of the contact between the resist and mask, very high resolution is possible in contact printing. The UV lamp at 355nm with an intensity of 3.5 mW/cm^2 was employed for about 20 seconds to a total exposure of 75 mJ. The intensity of an old UV lamp decays over time, so the exposure time was calculated after a trial exposure each time. Under-exposure results in poor quality of lithography with wiggly edges instead of straight lines while over exposure increases the mark-space ratio of the grating patterns.

e. Development

One of the final steps in the photolithography process was development, where the UV exposed resist was washed away by a developer solution leaving open windows of the underlying substrate. For the positive photoresist we employed, the developed sample contains an exact copy of the pattern on the mask. For the S1813 photoresist, MF319 was used as a developer solvent. For properly exposed samples, the development process was completed in around 60 seconds whereas underexposed samples would take longer or could not be developed with even several minutes of exposure to the developer. The development in MF319 was followed by washing the samples in running DI water for 1 minute and then blowing dry with N_2. In case of overexposed samples, the development was faster and also resulted in a larger size of the grating windows. The gratings of the first sample were visualized under a microscope and the exposure time for next samples was adjusted if the gratings were not properly developed. Figure 3-6 shows the microscopic images of the lithographically printed wafers after developing the sample for 1 minute.

f. Hard Baking

Hard baking of the photoresist is the final step in the photolithographic process. The samples were again put inside a cavity made of aluminum and a wire-mesh to avoid crystal cracking occurring with sudden temperature changes. The baking temperature was optimized to be at

120°C for 40 minutes in an oven. The temperature of the oven was increased using a ramp of 1°C/min till it reached 120°C. The oven was turned off in 40 minutes and allowed to cool down by itself. Hard baking of the resist is necessary in order to harden the photoresist and improve adhesion of the photoresist to the wafer surface thereby enhancing the insulation of the $LiNbO_3$ wafer for poling. The samples were ready for the poling process after this step.

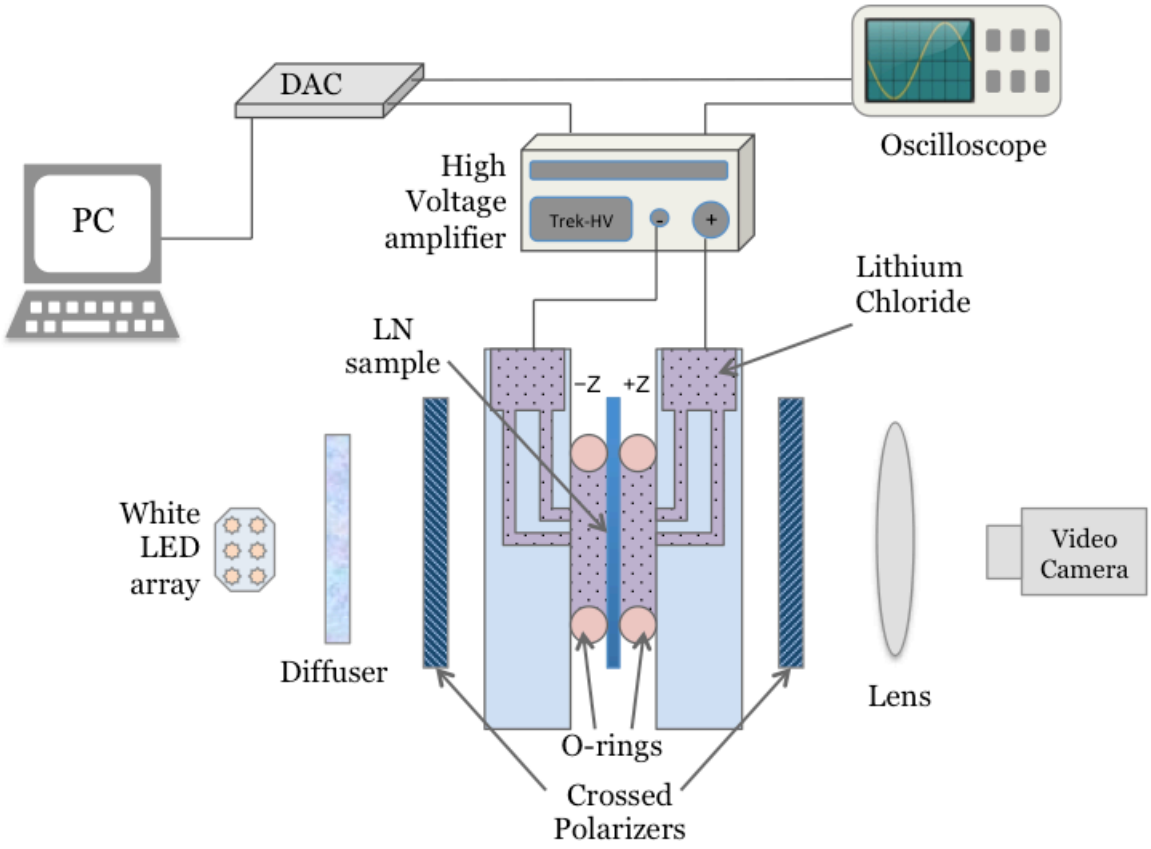

Figure 3-7: Schematic of poling experiment setup showing the high voltage application circuit and in-situ optical monitoring using crossed polarizers, DAC: data acquisition card, PC: computer.

3.4.2 Poling

The poling setup, as schematically described in Figure 3-7, consisted of a pulse generator circuit, a plexi-glass sample holder, an oscilloscope for measuring applied voltage and poling current, and a crossed polarizer assembly with a lamp for optical monitoring. A Labview program was written to control a data acquisition card (DAQ) used to send the voltage pulses and to measure

and record the poling current. A Trek-20 high voltage (HV) amplifier was used to amplify the input voltage pulse with a fixed gain of 2000 to generate the high electric fields required for domain inversion in lithium niobate.

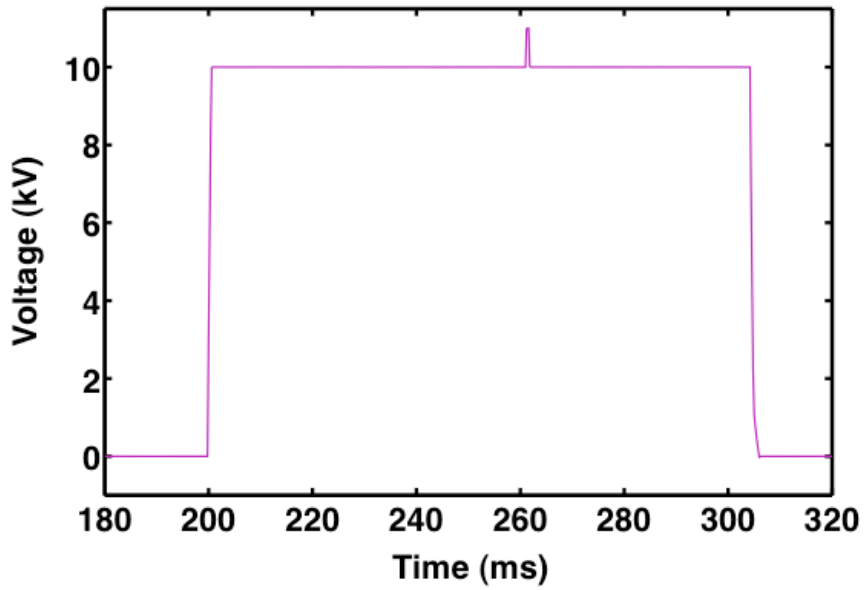

(a)

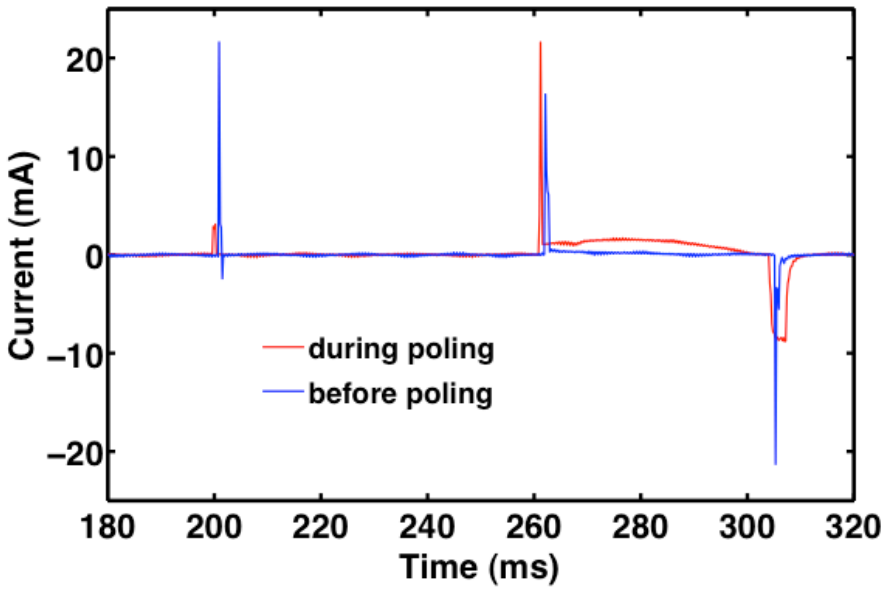

(b)

Figure 3-8: Applied voltage and observed current during the poling process

The sample was mounted in the plexi-glass fixture using O-rings on both surfaces to form an enclosure for the liquid electrolyte, shown schematically in the Figure 3-7. The edges of the lithographically printed sample were covered by a Teflon tape to avoid crystal breakage due to leaked charges during poling. A saturated solution of lithium chloride was used as the electrolyte, which was filled through the capillaries on the two blocks of sample holder to be in direct contact with the lithium niobate through the windows in the grating pattern.

The positive end of the HV output was connected to the +z side while the ground wire was connected to the as bought original –z side of the crystal. The shape, the pulse duration and the duty cycle of applied voltage pulses are deciding factors in controlling the domain reversal process. Undesirable effects of back-switching and domain merging/overpoling can be avoided by using a special voltage pulse shape.

Backswitching, as mentioned in section 3.3, refers to a partial or total de-poling of the crystal after switching off the external field. There are three stages of the applied pulse to achieve a complete domain reversal. This includes a warming up stage, a poling stage and a stabilization stage. The warming up stage has slightly less voltage (20 kV/mm) than the coercive field (21.5kV/mm) of LN to prevent the damage due to an abruptly elevating field. The poling stage has slightly higher field (22 kV/mm) than the coercive field but lower than the breakdown field (~26 kV/mm) which is responsible for domain nucleation and growth. The final stage of stabilization has a slightly lower field (same as the first stage) which is to avoid the backswitching problem. The optimized durations of the first and last stages were 60 ms each, whereas the poling stage was of $t_p = 0.5ms$ duration. The total number of pulses sent through the circuit depends on the amount of charge required to be deposited on the faces for complete domain reversal. This threshold charge is calculated by multiplying the total area A of the sample to be poled by the spontaneous polarization of lithium niobate, i.e., $Q = 2 \times P_s \times A$. The value of spontaneous polarization for lithium niobate is $P_s = 0.78\ \mu C/mm^2$. A poling current flows through the circuit due to the time-dependent change in spontaneous polarization during poling. It was measured using the DAQ card and the required number of pulses was calculated using the formula:

$$Q = \int I\, dt = I_p \times t_p = 2 \times P_s \times A \tag{3.1}$$

$$n = 2 \times P_s \times A\ /(I_p \times t_p) \tag{3.2}$$

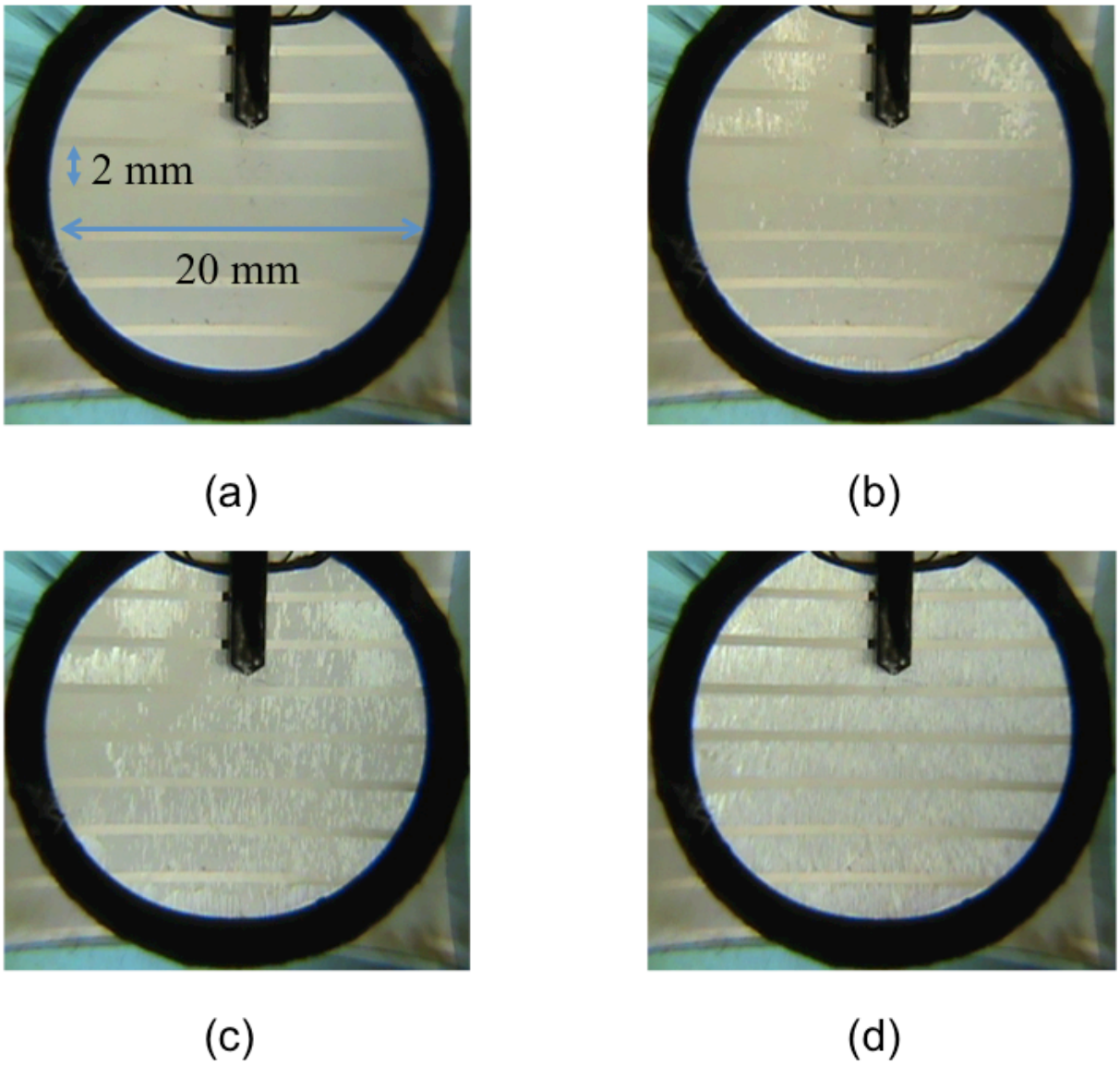

Figure 3-9: Images of poled grating patterns taken at various steps of poling (see text).

The voltage waveform applied for poling is shown in Figure 3-8(a) while a typical current trace is shown in Figure 3-8(b) where the blue trace shows the observed current before poling and the red trace shows the observed poling current during poling usually in μA. The straightforward relation given in equation (1) and (2) applies to periodic gratings of equal duty ratio. The calculation of required charge and thus the number of pulses becomes complicated for aperiodic chirped grating structures. In these cases, monitoring the current across the poled sample is not accurate. To monitor and control the overpoling of the domains under liquid electrodes, in-situ optical

monitoring was proposed by Shur *et al.* [106] and Missey (in 2000) [107]. The strain at inverted domains results in optical birefringence which is directly related to internal fields of the crystal. This results in imaging contrast of the two polarization states when viewed through crossed polarizers [108]. The onset of nucleation and growth of domains during the poling process was thus observed via a crossed polarizer setup and a camera to look at the scattering produced by inverted periodic structures.

The camera images of the patterned sample, (a) before, (b & c) during and (d) after poling are shown in Figure 3-9. During the optical monitoring of the poling process, it was observed that domain inversion started randomly across the grating channels soon after sending the first voltage pulse, however, there was a higher probability near the O-ring contact points due to the internal fields generated from the applied pressure. This led to the onset of poling reversal in neighboring domains which began to grow further until the whole area was poled by the domains spreading out from other nucleation sites. If the pulses were continuously applied even after all the domains were poled, the sideways domain propagation led to merging of the close proximity domains creating large overpoled regions of single orientation domain.

3.4.3 Surface relief of PPLN

The high conversion efficiency of quasi-phase-matched nonlinear conversion depends upon the uniformity of the periodic domain inverted structure of the ferroelectric. Visualizing the domains and studying the growth of domain walls using various techniques has been done by several research groups to assess the quality of poled devices. Some of the optical microscopy techniques that have been reportedly used for domain study are second harmonic generation microscopy [109], electrostatic force microscopy [110, 111] by interaction between a permanent negative charge of a scanner tip and distribution of the field on the domain inverted region, near-field scanning optical microscopy [97] using a polarization and phase sensitive near-field scanning microscope to measure the induced birefringence at the domain walls, and atomic force microscopy with different spatial resolutions [112]. Most common but a destructive diagnostic technique that has been extensively used is wet or chemical etching technique for revealing the domains near the surface [113]. This is made possible due to the differential rates of etching for the positive and negative surface of the crystal. Differential etching reveald the surfaces with lower etch-rates compared to the surface having a higher etch rate. The surface patterns thus

formed can be easily visualized under a microscope. Prolonged etching usually leads to undesired surface damage of the crystal which makes it unsuitable for nonlinear experiments involving waveguides close to the surface. However, controlled etching in bulk ferroelectric lithium niobate is common as the acid reacts with the –z surface and does not affect +z facet. Several etchants have been researched for revealing domains in LN such as hydrofluoric acid (HF), sulphuric acid (H_2SO_4), nitric acid (HNO_3), potassium hydroxide (KOH), potassium fluoride (KF) etc. The preferential etching of the –z surface in aqueous HF is explained by the surface protonation phenomenon, i.e. the replacement of surface hydroxide (OH^-) by fluoride (F^-) (initial dehydroxylation of the negatively charged surface by H^+ attack and then the reaction of subsequent positively charged surface with HF_2^- anions). This explains the faster etching rate of the –z surface as the positively charged proton is easily absorbed by the –z face, and also with an increase in concentration of acidic protons the etching rate increases. The short metal-oxygen bond on +z is indeed more stable than the longer bond on the –z face. It has been reported that 48% HF is the optimum etchant for LN, which was thus used to etch the samples reported in this thesis. The schematic of a revealed grating pattern before and after the etching procedure is given in Figure 3-10 which shows raised islands of +z surface in the background of the –z LN surface after the original –ve surface was etched in HF solution.

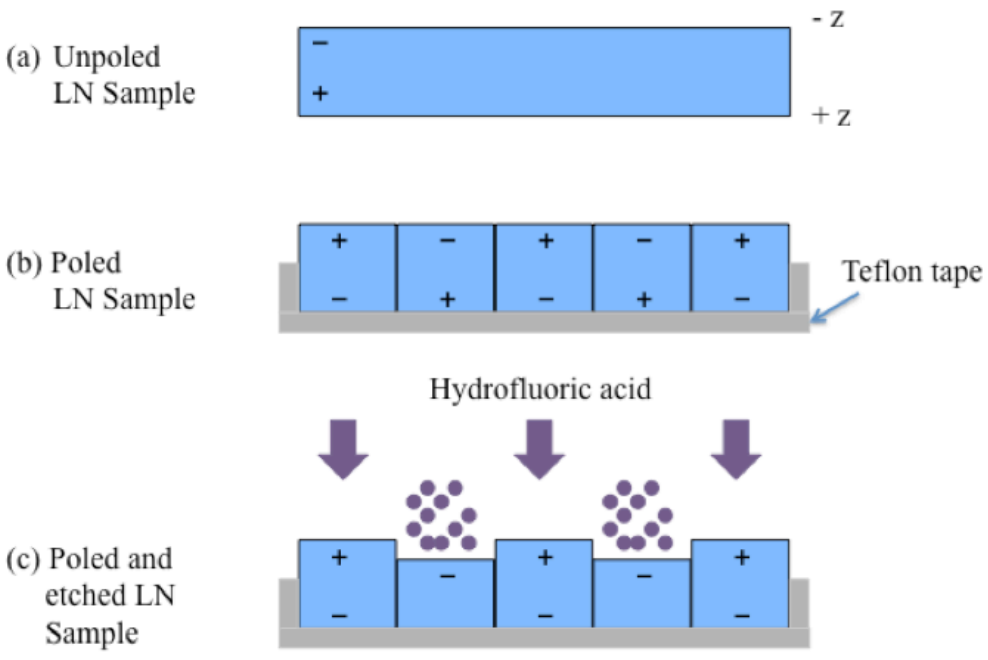

Figure 3-10: Schematic of revealing poled features in LN using HF etchant

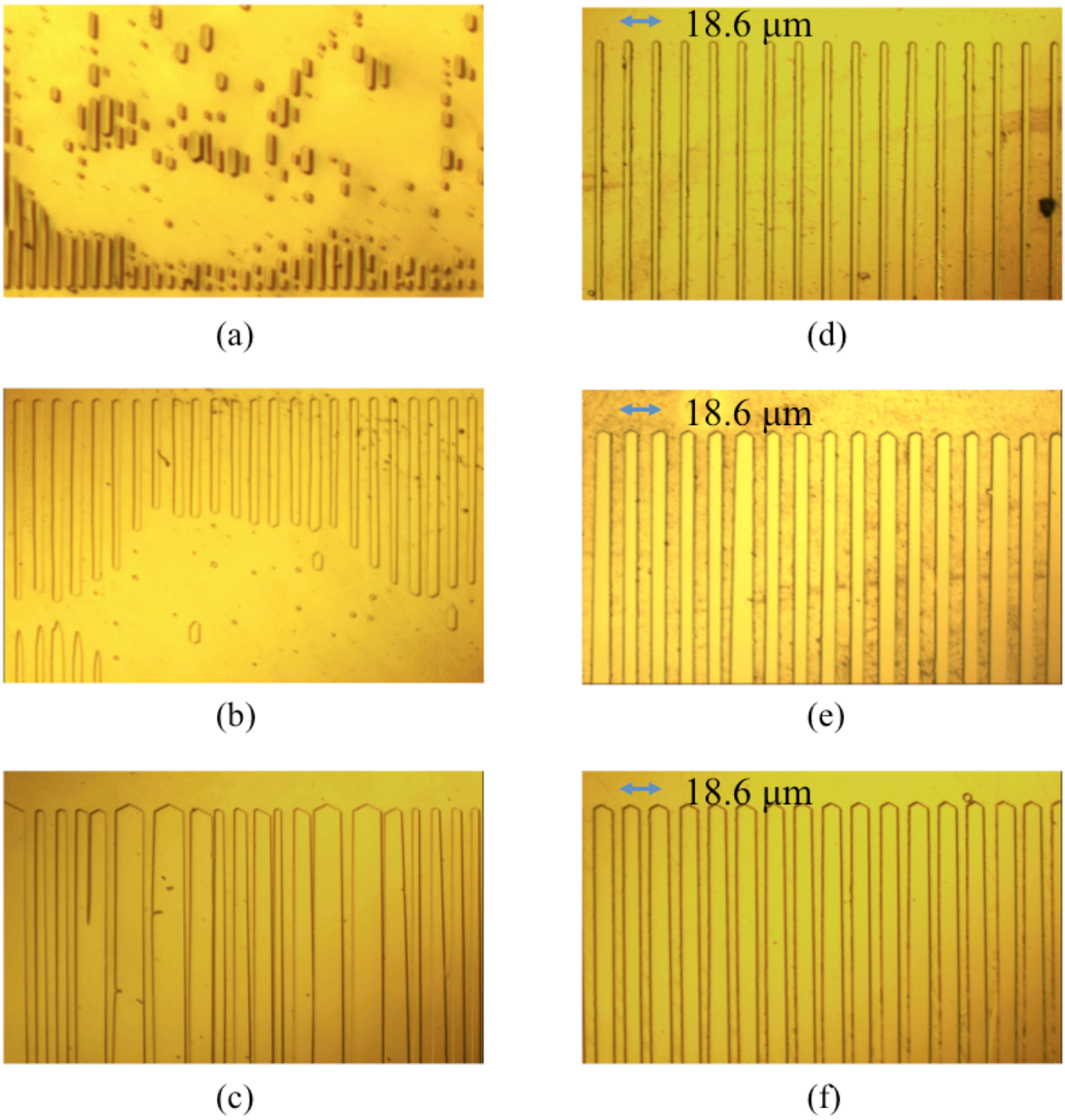

Figure 3-11: Microscope images of the revealed grating patterns on periodically poled lithium niobate after etching in HF for 5 minutes. The images shows: (a) onset of domain reversal at random nucleation sites; (b) under-poling of the periodic grating structure; (c) merging of grating patterns due to over-poling; (d)-(f) shows good poling with (d) <50% duty ratio; (e) ~50% duty ratio and (f) >50% duty ratio.

The detailed etching process followed for visualizing PPLN domains is explained as follows. Before etching, the PPLN sample is cleaned with acetone and ethanol to remove the residual of photoresist on it. A solution of 48% Hydrofluoric (HF) acid is then used as the etchant for revealing the surface relief grating and to examine the uniformity and quality of the domain pattern. The original +z face of the crystal is protected using a Teflon tape and the sample is then immersed in the HF and kept in a PTFE container for 5 minutes. The sample is cleaned thoroughly using deionized water after etching and blow dried with N_2. The domain patterns are then observed through a microscope camera. Some of the images are shown in the Figure 3-11.

Subsequent processing of the poled sample is required before it can be used for SH characterization. The sample is cut into rectangular pieces to separate the unpoled area surrounding the poled grating channels. A diamond dicing saw was used for cutting the crystal. Then the input and output faces were polished to efficiently couple the light into the polished crystal edge face. For polishing the sample was sandwiched between two identical lithium niobate crystal pieces and mounted on the holder used for end polishing. The polishing was done in four steps by successively using 30 μm, 6 μm, 1 μm, and 0.1 μm grain size polishing plates. Each plate was rotated clockwise and anticlockwise for approximately 10 minutes at a spin rate of 30 rpm. The rigorous polishing procedure minimizes the scattering losses due to any edge roughness and the losses that remained were mainly due to Fresnel reflections (~14% on each surface). No anti-reflection coating was deposited on the samples to reduce the Fresnel reflection loss.

3.5 Errors in duty cycle

There are in general two types of structural errors possible in the periodically poled structures: (a) error in Period of the grating and (b) error in Duty cycle of the grating. The former usually occurs when domain inverted gratings are formed by direct writing methods such as e-beam or laser beam writing. Whereas, in case of photolithography based periodic poling described in this dissertation, the average period is uniformly maintained across the crystal. However, there are local perturbations in the position of domain boundaries which give rise to errors in the domain width or the duty cycle in the otherwise uniform period of the grating. This kind or random duty cycle error decreases the efficiency of the QPM device by decreasing the effective nonlinear coefficient. The decrease in the SH conversion efficiency can be explained by considering again

the equation 2.12: $d_Q = d_{33} G_m$ where d_Q is the amplitude of the relevant spatial harmonic variation of $d(z)$, d_{33} is the largest coefficient of the nonlinearity tensor of LN, and $G(m) = (2/m\pi) \sin(m\pi R)$ is the Fourier coefficient of $d(z)$ series for the QPM order m. At the optimum value of duty ratio R i.e. 50%, the first order QPM gives the highest nonlinearity term as shown in Figure 3-12. First order quasi phase matching depicted by the red trace shows that the nonlinearity decreases with a deviation of duty ratio from its optimum value. The nonlinearity due to the third order QPM is given by the black trace which maximizes at two other values along with the 50% duty ratio. The contribution to nonlinearity due to even orders illustrated by blue and red trace disappear for 50% duty ratio but maximize at 25% and 12.5% ratio, respectively.

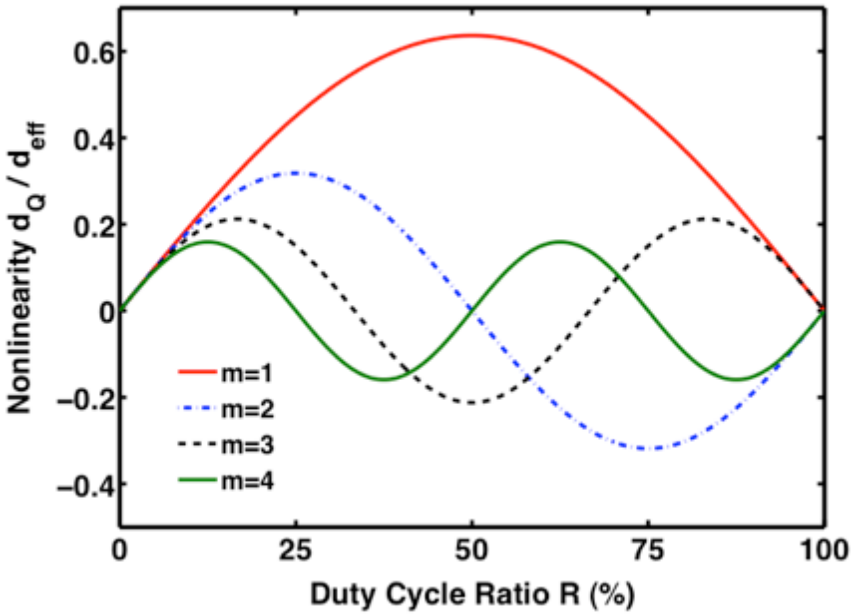

Figure 3-12: Variation of QPM nonlinearity with duty cycle ratio for first four orders of quasi phase matching.

3.6 Conclusion

This chapter introduced the concepts of ferroelectric domain inversion, focusing on the model of the mechanism behind poling reversal. The structure of lithium niobate was discussed along with the various properties such as its nonlinearity, birefringence etc. Subsequently, the electric field

poling process was described in detail as the technique used to prepare the PPLN crystals for the experimental results reported in this thesis. This comprised of a review of various steps such as photolithography imprinting of photoresist on lithium niobate to transfer a desired grating pattern, application of high voltage pulses for domain nucleation and growth in the direction of applied field, monitoring the poling process using crossed polarizers and then the assessment of the fabricated grating patterns by chemical etching in HF acid.

CHAPTER 4
ULTRA BROADBAND FLATTOP WAVELENGTH CONVERSION BASED ON CASCADED SFG-DFG IN PPLN WAVEGUIDES

4.1 Overview

Wavelength conversion is of great importance in WDM optical networks [114, 115]. Several schemes for all-optical wavelength conversion have been realized in the quasi phase matched nonlinear crystals [116]. The difference frequency generation (DFG) based wavelength conversion technique in PPLN waveguides gained attention due to simultaneous conversion of broadband wavelength channels with no signal-to-noise degradation irrespective of the signal modulation format [117]. However, for efficient DFG devices there is a need for high power, tunable pump lasers in not so readily available in 750-800 nm wavelength range and also there are losses associated with ineffective coupling of the two different spectral ranges in a single-mode waveguide. Another wavelength conversion scheme based on cascaded second harmonic generation and difference frequency generation (cSHG-DFG) proved to be an effective technique to overcome the shortcomings of a DFG interaction [118]. It involved the pump and signal wavelengths both in the 1.55 μm C-band to generate the output idler as a result of difference frequency (DF) mixing of the signal with the pump SH. This scheme however has the limitation of the pump wavelength occupying one of the channels in the C-band.

The cascaded sum and difference frequency generation (cSFG-DFG) technique, on the other hand, requires two pump wavelengths which can be located out of the C-band for converting a signal to the idler. The cSFG-DFG scheme also allows the control over the conversion bandwidth by changing the pump wavelength difference and is beneficial for optical signal processing [45]. The principle behind the wavelength converter device based on cSHG/DFG and cSFG/DFG is illustrated in a photon diagram of Figure 4-1. The theoretical analysis of a cSFG/DFG process shows that as the pump wavelength difference for cSFG-DFG process is increased, it leads to ripple in the conversion bandwidth with a decrease in efficiency in the center of bandwidth response [46]. For WDM applications, there is a need to not only enhance the conversion bandwidth of the QPM converters but also achieve a flat response in the entire 1.55 μm C-band.

It has been theoretically demonstrated that flattening of the efficiency response in cSFG-DFG can be achieved by slight detuning of one of the pump wavelengths [46].

In this chapter, firstly, wavelength conversion based on cSHG-DFG and cSFG-DFG in an MgO doped PPLN waveguide is experimentally demonstrated using the input pumps and signal wavelengths in the 1.55 μm band. Thereafter, experimental demonstration of flattening of the response of cSFG-DFG conversion by detuning of the pump wavelengths from their phase matching condition is presented. We also propose and demonstrate three-channel all-optical broadcasting in a PPLN waveguide using simultaneous cSHG-DFG and cSFG-DFG processes. Comparison of the PPLN waveguide with an aperiodically poled lithium niobate (aPPLN) is made to demonstrate the advantage of a broadband device for WDM broadcasting applications.

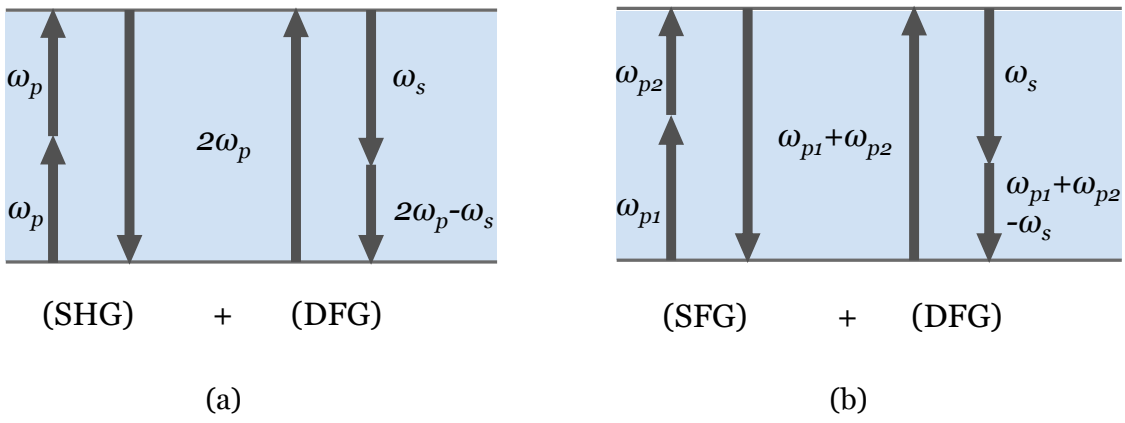

Figure 4-1: The schematic photon diagram of (a) cascaded second harmonic generation and difference frequency generation; (b) cascaded sum frequency generation and difference frequency generation.

4.2 Experimental demonstration of Cascaded $\chi^{(2)}$(SHG) - $\chi^{(2)}$ (DFG)

A 45 mm-long MgO-PPLN waveguide device is used for the wavelength conversion experiments described in this chapter. MgO doping increases the photorefractive damage threshold of LN and allows the design of PPLN for room temperature operation [21, 22]. The waveguide was fabricated using the annealed proton exchange (APE) method [23]. To fabricate the APE waveguide, a channel mask of thickness ~ 0.1 μm for the selected proton exchange is imprinted on the z-cut lithium niobate using lift-off or etching techniques. Then the crystal with patterned

mask is immersed for several minutes in a proton source such as molten benzoic acid at a temperature ranging from 160°C to 240°C for the PE. Afterwards, the crystal is thermally annealed to reduce the propagation loss and recovering the nonlinearity [23, 119]. The device is periodically poled using the liquid electrode poling method described in chapter 3.

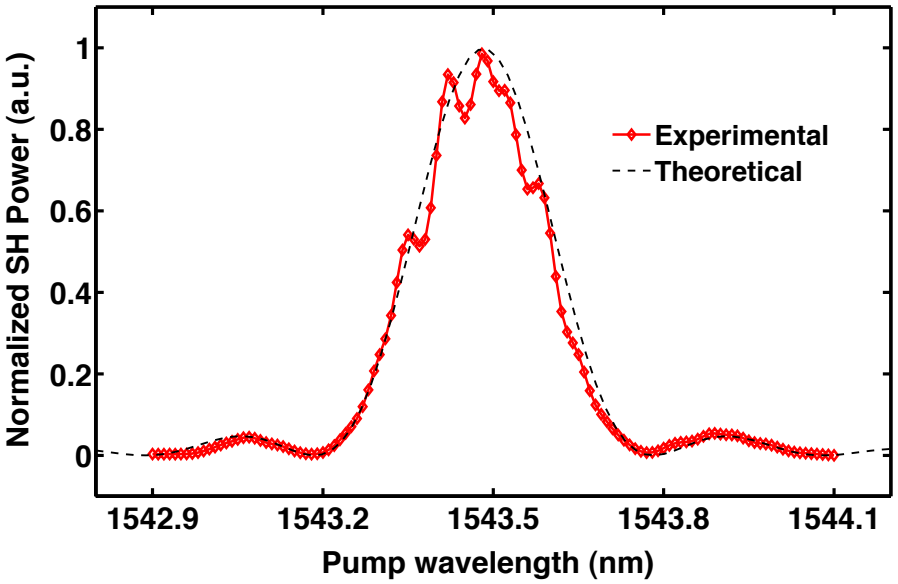

Figure 4-2: Experimental and theoretical second harmonic response of the 45 mm long MgO-doped-PPLN waveguide.

The PPLN was kept on a temperature controlled (TC) mount for stabilizing the temperature during the experiments. It was then characterized for nonlinear SH conversion efficiency by using a tunable laser operating in the 1.55 μm range. The laser was amplified using an Erbium doped fiber amplifier (EDFA) and its polarization was adjusted along the maximum nonlinearity coefficient d_{33} of lithium niobate for type-0 phase matching $e+e\rightarrow e$. The SH output is measured using an optical spectrum analyzer. The experimental result of SH bandwidth obtained by tuning the pump laser is shown by the red trace in the Figure 4-2 and the theoretical sinc dependence curve is given by the black dashed trace. The slight deviation of the experimental curve from a perfect fit could be attributed to the partial phase-shifts in the QPM device occurring due to fabrication errors in the poling period.

The QPM peak of the SH conversion is obtained at 1543.43 nm at 23.6ºC. The peak SH power is 11.06 mW at 124 mW power of the input pump, giving a 71.5 %/W SH conversion efficiency. For comparison, the calculated efficiency is ~280 %/W for non-depleted-pump, loss-less PPLN waveguides of length L given by $\eta_{\mathrm{SHG}} = P_{\mathrm{SH}} / P_p^2 = \kappa_{\mathrm{SHG}}^2 L^2$ using the typical value of coupling factor for SHG process, $\kappa_{\mathrm{SHG}} = 0.37\ \mathrm{W}^{-1/2}\ \mathrm{cm}^{-1}$ [120].

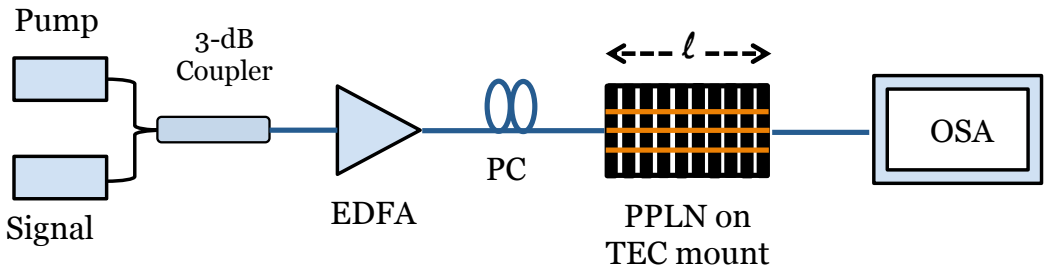

Figure 4-3: Experimental setup for cascaded SHG-DFG in MgO-PPLN waveguides. Here, the Pump and Signal are tunable laser sources in the 1550 nm range, EDFA: Erbium doped fiber amplifier, PC: polarization controller, OSA: optical spectrum analyzer. For cSFG-DFG, two pump lasers are launched along with the signal.

Using this MgO-PPLN waveguide device, conversion of a signal to an idler via the cSHG/DFG was also demonstrated. In a cSHG/DFG process, a pump wave of frequency ω_0 launched at the QPM peak of the PPLN device gets upconverted to a SH wave at $2\omega_0$ via the second-order nonlinearity $\chi^{(2)}$. A signal wave of frequency ω_s coupled into the PPLN simultaneously undergoes a DF mixing process with the pump SH to generate a converted wave at the difference frequency, $\omega_c = 2\omega_0 - \omega_s$. The converted idler frequency is symmetrically opposite to the signal frequency with respect to the pump frequency. Phase-matching between the interacting waves for both the SHG and DFG is required, which can be achieved by choosing appropriate grating period Λ, as described by the following equations:

$$4\pi n_{SH}\omega_0 / c - 4\pi n_0\omega_0 / c = 2\pi / \Lambda \qquad (4.1)$$

$$4\pi n_{SH}\omega_0 / c - 2\pi n_s\omega_s / c - 2\pi n_c\omega_c / c = 2\pi / \Lambda \qquad (4.2)$$

Here, n_0, n_s, n_{SH} and n_c are the refractive indices at the pump, signal, SH and converted signal (idler) frequencies.

In the next step, wavelength conversion based on cSHG-DFG is demonstrated in the MgO-PPLN waveguide using the experimental setup illustrated in Figure 4-3. It consists of two tunable laser sources in the 1550-nm band acting as pumps and a tunable source as a signal, which are combined by a WDM coupler and amplified by a 30-dBm Pritel EDFA to a total of 23-dBm power and then launched into a 45-mm MgO-doped PPLN waveguide. The fiber to waveguide coupling loss including the 13.5% reflection loss at the input and output ends for the PPLN sample is 8 dB, which can be attributed to the numerical aperture (NA) mismatch; compared to which the waveguide propagation loss is considered negligible. A polarization controller was used to adjust the polarization states of the pump and the signal to maximize the output idler efficiency. The PPLN was kept on a temperature controlled (TC) mount at a temperature of 23.6 ºC corresponding to the maximum SH. The output is measured using an optical spectrum analyzer.

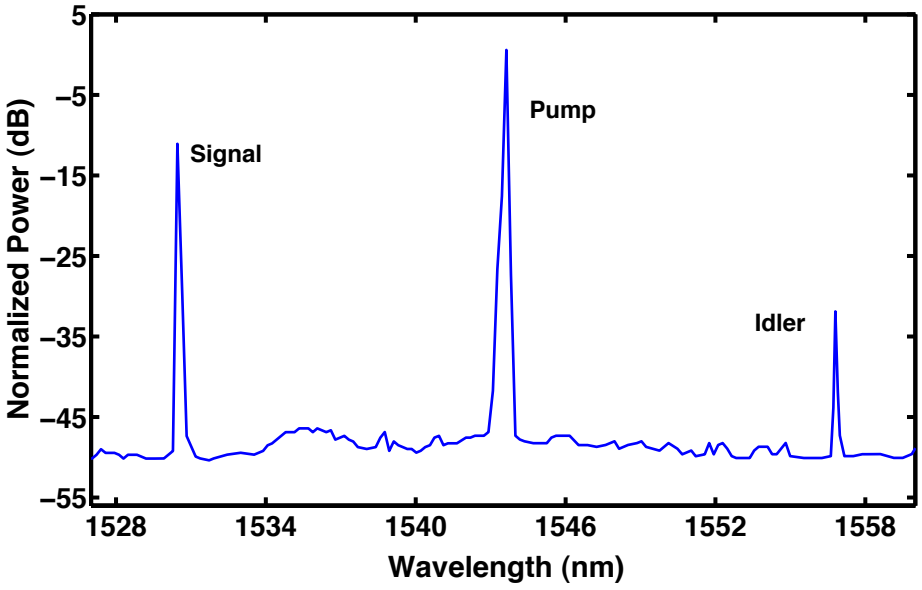

Figure 4-4: Experimentally observed spectrum for converting a signal at 1530.5 nm to an idler at 1556.8 nm via the cascaded SHG-DFG process by employing a pump at 1543.45 nm in the MgO-PPLN waveguide.

A typical spectrum observed at the end of the PPLN as a result of wavelength conversion in a cSHG/DFG process is shown in Figure 4-4. It depicts the conversion of a signal at 1530.5 nm to an idler wavelength at 1556.8 nm obtained by launching a pump laser at 1543.45 nm, the QPM wavelength of the MgO-PPLN waveguide. The peak power of the converted signal was -11.90 dBm for a launched signal power of 10.20 dBm and the pump power of 21.60 dBm. giving a conversion-efficiency (power ratio of idler and signal) for the cascaded process as 0.61% (-22.10 dB).

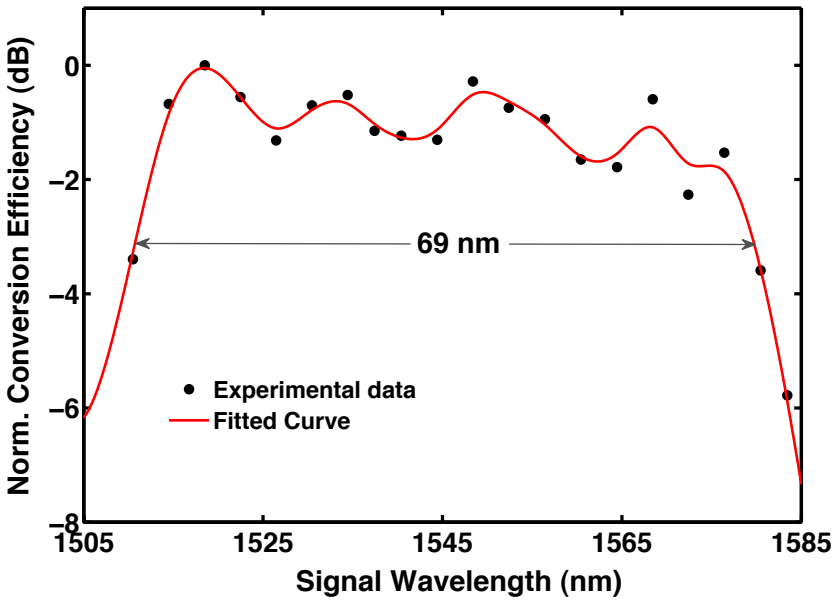

Figure 4-5: Conversion bandwidth of the cSHG-DFG process obtained by tuning the signal wavelength over 1507 nm - 1583 nm for a pump fixed at 1543.4 nm.

Similar idlers were generated by tuning the signal wavelength over ~80 nm while keeping the pump fixed at the QPM wavelength of 1543.4 nm. Figure 4-5 (black round markers) shows the plot of the normalized converted signal efficiency against signal wavelength for the cSHG-DFG, giving a 3-dB bandwidth of approx. 69 nm. The red solid line shows the spline curve fitting to the experimental data. Therefore it is shown that using cSHG/DFG process in a PPLN device, a signal anywhere in the wide conversion bandwidth of ~70 nm can be converted to an idler wavelength satisfying $\omega_c = 2\omega_0 - \omega_s$ using a fixed pump wavelength.

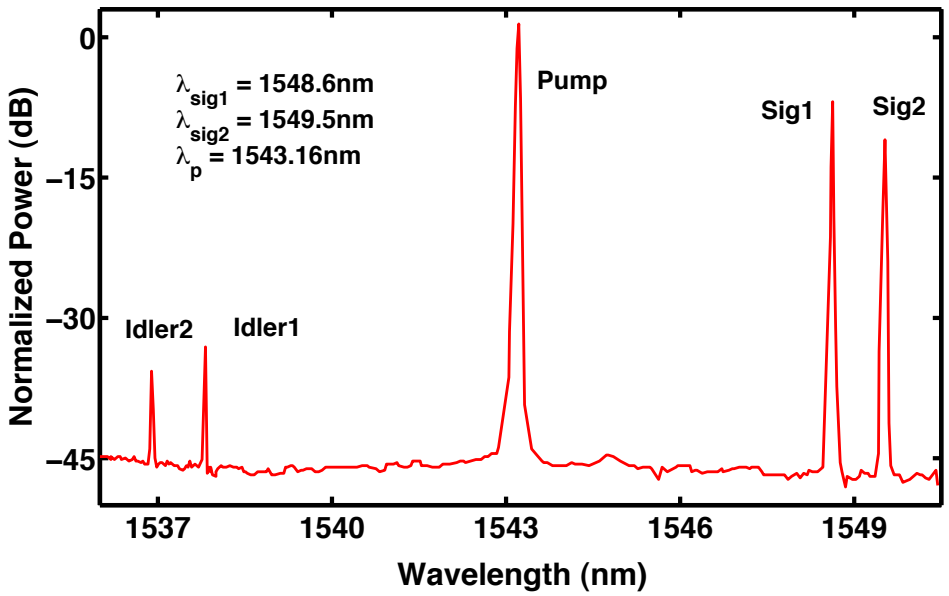

Figure 4-6: Experimentally observed spectrum of simultaneous conversion of two signals at 1548.6 nm and 1549.5 nm to respective idlers at 1537.8 nm and 1536.9 nm with the pump laser set at 1543.16 nm.

It is to be noted that the wide conversion bandwidth is due to the DFG phase matching condition. The narrow SH bandwidth of a uniform PPLN, on the other hand, puts a restriction on the choice of the pump wavelength. Therefore, the conversion of a signal channel is only allowed to a specific idler for the given PPLN device. Nevertheless, this scheme is beneficial for converting multiple signals to corresponding idlers in a single device using a pump laser. We launched two signal lasers and one pump laser, amplified using an EDFA, into the PPLN to generate two idlers. This experimentally observed spectrum is shown in Figure 4-6, where two signals at 1548.6 nm and 1549.5 nm are simultaneously converted to their respective idlers at 1537.8 nm and 1536.9 nm when the pump laser is set at 1543.16 nm. The results can be further extended to three or more signals, which is promising for WDM applications requiring the conversion of multiple signals to fixed idlers using a single all optical wavelength converter.

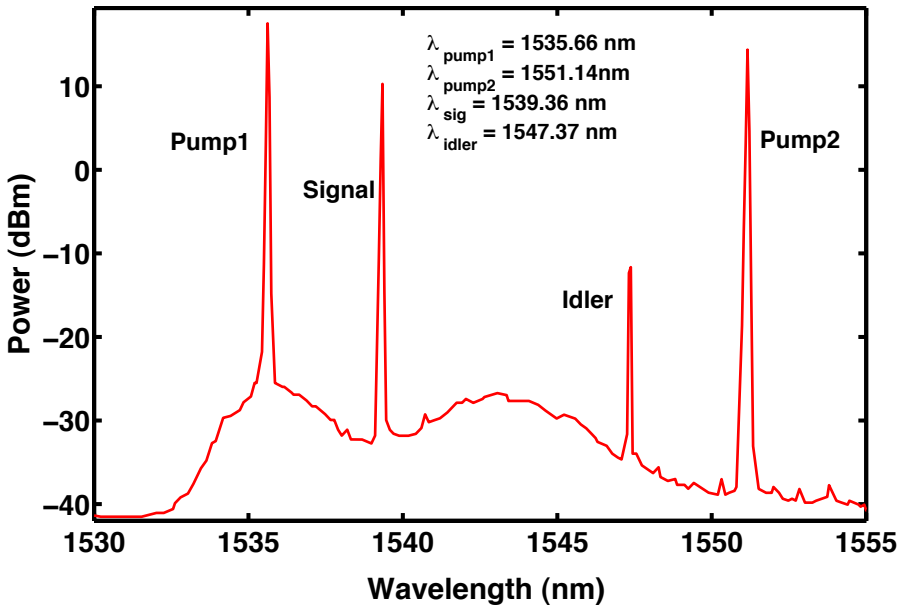

Figure 4-7: Experimentally observed spectrum of converting a signal at 1539.36 nm to an idler at 1547.37 nm via the cascaded SFG-DFG process by employing two pumps at wavelengths of 1535.66 nm and 1551.14 nm in the MgO-PPLN waveguide.

4.3 Experimental demonstration of Cascaded χ(2)(SFG) - χ(2) (DFG)

The cascaded SFG-DFG process takes place in two steps. Initially, two pump waves of frequencies ω_{p1} and ω_{p2} generate a SF wave at $\omega_{p1}+\omega_{p2}$. The SF wave at the same time mixes with a signal wave of frequency ω_s to create a converted wave at the difference frequency, $\omega_c=\omega_{p1}+\omega_{p2}-\omega_s$ when the QPM condition for DFG is satisfied. The experimental setup for cascaded SFG-DFG is similar to cSHG-DFG shown in Figure 4-3, with an additional tunable pump laser in the C-band.

For input pump powers of P_1 = 153.11 mW and P_2 = 56.23 mW, the SF output power obtained was 25.76 mW, giving an efficiency of 300 %/W. The experimental efficiency is calculated after taking into account the fiber-to-fiber coupling loss. The theoretical calculated efficiency for SFG in the non-depleted-pump lossless PPLN waveguide is given by $\eta_{\mathrm{SFG}}=P_{\mathrm{SF}}/(P_{p1}P_{p2})=\kappa_{\mathrm{SFG}}^2L^2$ which is ~1100 %/W using the typical value of coupling factor for SFG process, κ_{SFG} = 0.74 $\mathrm{W}^{-1/2}$

cm^{-1}. Figure 4-7 shows the measured spectrum obtained with an optical spectrum analyzer at the output of the MgO-PPLN waveguide. A signal at a wavelength of 1539.36 nm is converted to an idler at 1547.37 nm via the cascaded SFG-DFG process by employing two pumps at 1535.66 nm and 1551.14 nm in the MgO-PPLN waveguide. The idler is generated symmetrically opposite to the signal wavelength with respect to the center of the two pump wavelengths. The peak power of the converted signal was -10.34 dBm for a launched signal power of 11.19 dBm and with the pumps at 20.93 dBm and 17.54 dBm giving a conversion-efficiency (power ratio of idler and signal) for the cascaded process as 0.7% (-21.53 dB). For a non-depleted-pump, loss-less device of given length L, the theoretical idler power can be estimated from the following equation [120]:

$$P_c = P_s P_{p1} P_{p2} \kappa_{\mathrm{SFG}}^2 \kappa_{\mathrm{DFG}}^2 \frac{L^2}{4} \tag{4.3}$$

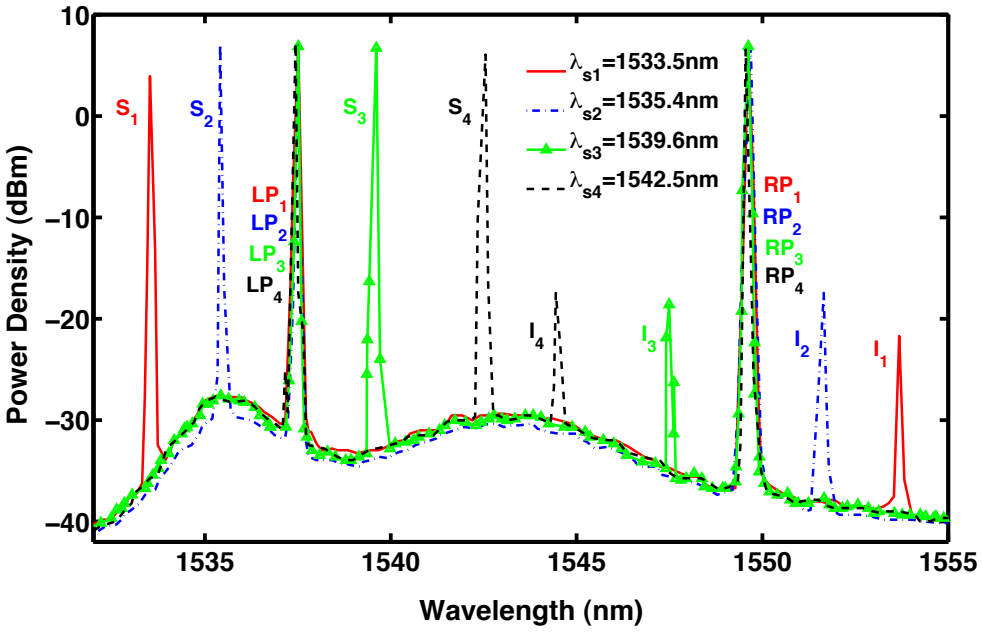

Figure 4-8: Overlap of four experimentally observed spectra of idler generation via cSFG-DFG process keeping the two pumps fixed 12.1 nm apart at 1537.4 nm and 1549.5 nm and varying the signal wavelengths over 9 nm. Here S_1 to S_4 represent the signal, LP_1 to LP_4 represent the left pump, RP_1 to RP_4 represent the right pump and I_1 to I_4 represent the converted idlers.

Here P_c is the converted signal power, P_s is the input signal power, P_{p1} and P_{p2} are the two pump powers, κ_{SFG} and κ_{DFG} are the coupling factors for SFG and DFG in PPLN waveguide, respectively and $\kappa_{DFG} = ½\ \kappa_{SFG}$. The typical value of the DFG coupling factor for PPLN waveguide is $\kappa_{DFG} = 0.37\ W^{-1/2}\ cm^{-1}$. Using the value of the parameters in equation (4.3), for the SFG-DFG process in PPLN waveguide, the maximum conversion efficiency (the power ratio of converted signal to input signal) was computed to be 0.97%, which compares favorably with our experimental result.

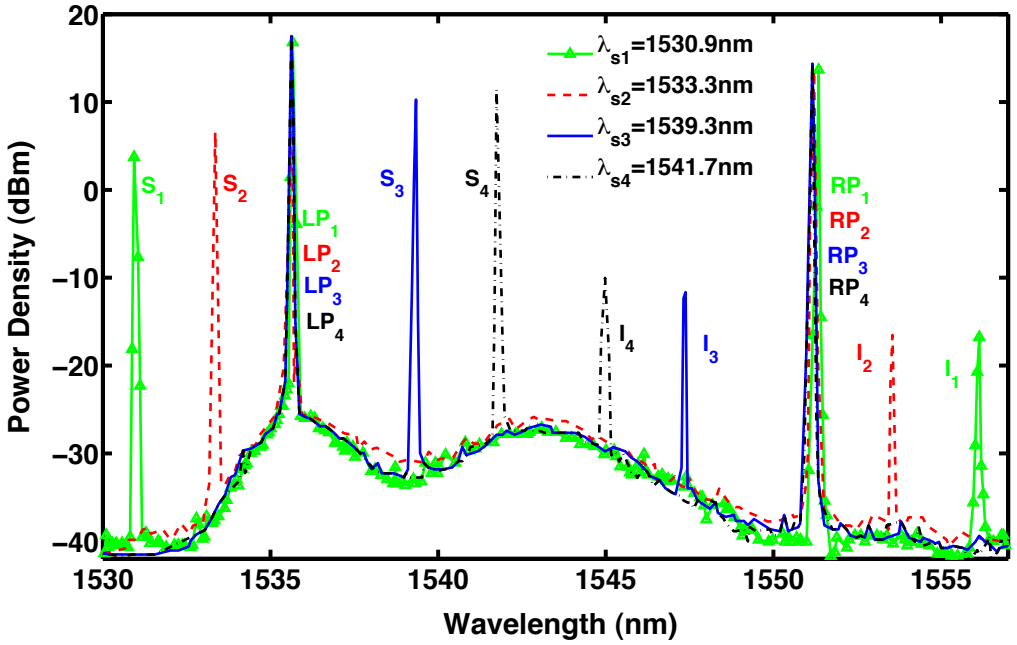

Figure 4-9: Overlap of four experimentally observed spectra of idler generation via cascaded SFG-DFG process keeping the two pumps fixed 15.5 nm apart at 1535.66 nm and 1551.14 nm and varying the signal wavelengths over ~11 nm. Here S_1 to S_4 represent the signal, LP_1 to LP_4 represent the left pump, RP_1 to RP_4 represent the right pump and I_1 to I_4 represent the converted idlers.

For converting a signal in a uniform PPLN based on cSFG-DFG process, the two pump wavelengths are selected so that their center (mean of wavelengths) is fixed at the device QPM peak i.e. at 1543.5 nm, whereas the mutual spacing of pump wavelengths can be varied. In Figures 4-8, 4-9 and 4-10, the experimental results have been shown for generating the output

idler by tuning the signal for three different cases of pump wavelength spacing. We employed a tunable signal across a 75-nm bandwidth from 1510 nm to 1585 nm for these experiments. For example, Figure 4-8 shows an overlap of four measured spectra of idlers generated across wavelengths 1553.5 to 1544.5 nm by varying the signal from 1533.5nm to 1542.5 nm, when the two pumps are fixed 12.1 nm apart at 1537.4 nm and 1549.5 nm. In terms of 50 GHz WDM network grid, the idlers span of 9 nm corresponds to 22 WDM channels. Tuning of the signal wavelength by "δ" nm leads to an equal "-δ" nm tuning of the idler wavelength. The noise observed in each of the spectra is due to the amplified spontaneous emission (ASE) of the EDFA.

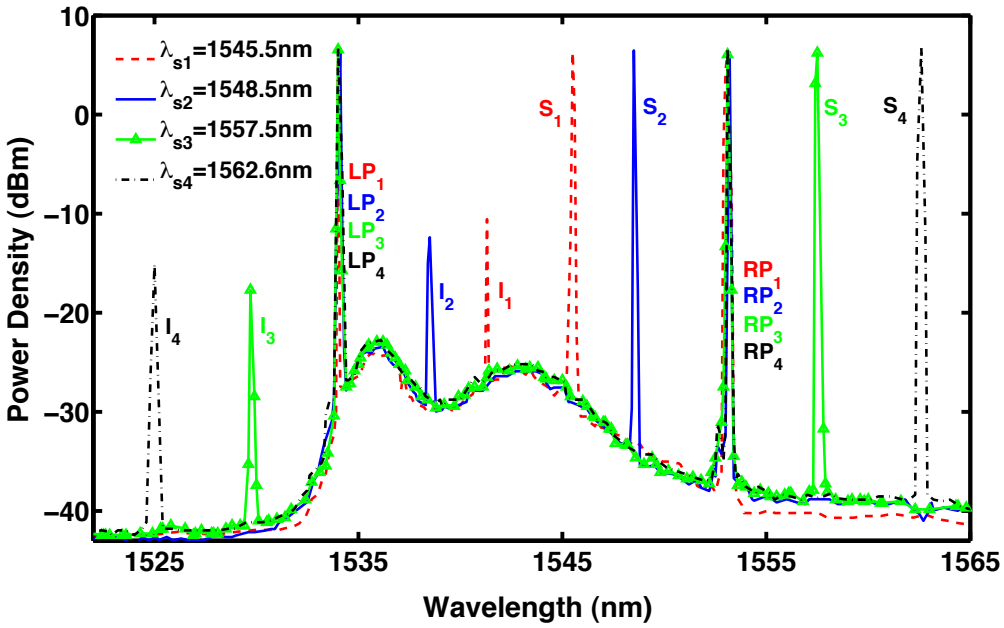

Figure 4-10: Overlap of four experimentally observed spectra of idler generation via cascaded SFG-DFG process keeping the two pumps fixed 18.9 nm apart at 1534.1 nm and 1553.0 nm and varying the signal wavelengths over ~17 nm. Here S_1 to S_4 represent the signal, LP_1 to LP_4 represent the left pump, RP_1 to RP_4 represent the right pump and I_1 to I_4 represent the converted idlers.

In another experiment, the pumps are equally detuned from their center at a wavelength of 1543.5 nm to achieve a separation of 15.5 nm, so that they are located at 1535.66 nm and 1551.14 nm. The results of cSFG-DFG based conversion of the signal are summarized in Figure 4-9, where in

four separate measurements the signal is tuned over 10.8 nm from 1530.9 nm to 1541.7 nm to generate idlers across 1556.1 nm to 1545.3 nm, the idlers spread of 10.8 nm corresponds to 26 WDM channels of 50 GHz spacing.

The pumps separation was further increased to 18.9 nm by tuning their wavelength to 1534.1 nm and 1553.0 nm. As illustrated in Figure 4-10 by four overlapping spectra, the idlers are generated at a span of ~17 nm from 1524.4 nm to 1541.5 nm when the signal is tuned from 1545.5 nm to 1562.6 nm. The idlers spread corresponds to 41 WDM channels of 50 GHz spacing.

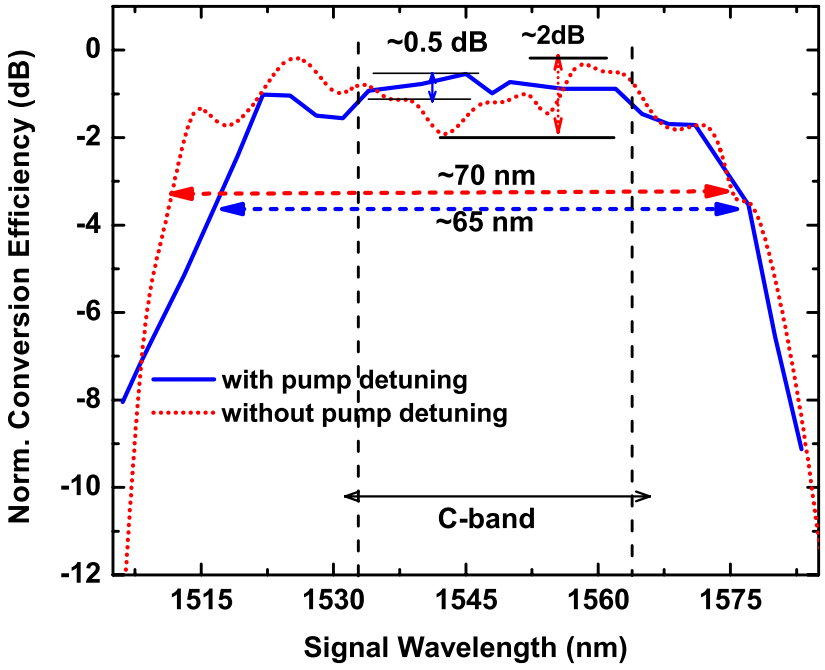

Figure 4-11: Normalized conversion efficiency versus signal wavelength in SFG-DFG for perfectly phase matched pumps (dotted line), and when the longer pump is detuned by 0.15 nm from the phase-matched wavelength (solid line).

4.4 Conversion bandwidth flattening by pump detuning

To obtain the conversion bandwidth response of the cSFG/DFG process, two pump wavelengths are chosen for maximum sum frequency generation and a tunable signal is swept across a 75-nm bandwidth, from 1510 nm to 1585 nm to be converted to the idler. The MgO-PPLN waveguide,

as already characterized, has a SF QPM peak at a wavelength of 1543.5 nm. For this measurement, the pumps are positioned 15.48 nm apart at 1535.66 nm and 1551.14 nm. Figure 4-11 (red-dotted trace) shows the plot of the normalized converted signal power against signal wavelength for the cascaded SFG-DFG, giving a 3-dB bandwidth of approx. 70 nm. We can observe a 2-dB overall peak-to-peak ripple giving higher conversion efficiency at the edges of the conversion bandwidth and lower in the center.

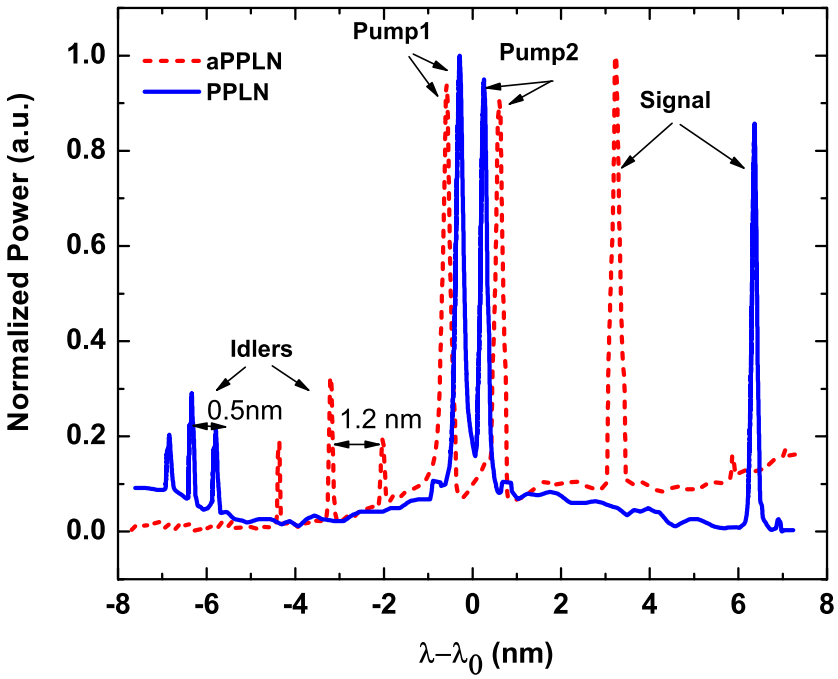

Figure 4-12: Measured spectrum using OSA: one signal is converted to three idlers using two closely spaced pumps for PPLN waveguide (solid line) and for aPPLN waveguide (dotted line). λ_0 is the phase matched wavelength for the SFG process which is 1543.5 nm for PPLN and 1534.34 nm for aPPLN waveguide.

In the case of the two separate pumps producing SFG-DFG, the SFG process is perfectly phase matched between the pump wavelengths while DFG process is phase matched at the two pump wavelengths and has a maximum phase mismatch at the center. As was already predicted theoretically, as the pump wavelengths are separated further apart in a SFG-DFG process, the

ripple in efficiency response increases and the conversion bandwidth is enhanced compared to the degenerate case of SHG-DFG [46]. This ripple in efficiency is not desirable in optical communication and hence it was theoretically proposed that the ripple could be overcome by slightly increased detuning of one or both pumps to longer wavelengths. The transformation of phase matching conditions of SFG and DFG decreases the phase mismatch at the center. This, however, results in small reduction in bandwidth and mean efficiency, which can be easily compensated for by using increased pump powers.

The experimental demonstration was performed by choosing the wavelengths of the two pumps at 1535.72 nm and 1551.35 nm where the second pump is detuned by 150 pm from its wavelength for perfect phase-matched SFG. The result is presented in Figure 4-11 (blue-solid trace) showing normalized conversion efficiency against signal wavelength. The maximum conversion efficiency of 0.33% (-24.83 dB) is achieved when signal is at a wavelength of 1540.01nm with 15.92 dBm input power and the idler is generated at 1546.98 nm with -8.91dBm output power. Therefore, the efficiency suffers almost a 3-dB penalty over the non-detuned pump case. In addition, the conversion bandwidth is decreased by 5 nm; however, a 1.5-dB decrease is noted in the peak-to-peak ripple in the wavelength range 1532 nm to 1564 nm covering over 90% of the optic communication C-band. The flattening of conversion bandwidth will prove significant in realizing such devices for practical applications.

4.5 Wavelength broadcasting in PPLN and aPPLN waveguides

Broadcasting refers to the conversion of a signal to several destination channels. All optical flexible wavelength broadcast based on simultaneous broadband SFG and SHG to generate multiple idlers was demonstrated recently in PPLN [56]. In this section, wavelength broadcasting devices are demonstrated based on cascaded second–order $\chi^{(2)}$ nonlinearities in 45-mm PPLN and aperiodically poled lithium niobate (aPPLN) waveguides in which one signal was converted to three different idlers when the two pumps are closely spaced within the SH bandwidth of devices producing one SF and two SH frequencies. The schematic of multiple-channel broadcast is illustrated in Figure 2-7 in chapter 2.

We already characterized the PPLN waveguide and obtained a QPM peak at a wavelength of 1543.5 nm with 71.5%/W SH conversion efficiency and 0.3 nm FWHM bandwidth, as shown in Figure 4-2. Figure 4-12 (blue solid line) shows the normalized spectrum for the broadcasting

experiment with three idler peaks at wavelengths of 1536.31 nm, 1536.82 nm and 1537.35 nm corresponding to the signal peak at 1549.51 nm when the two pumps were fixed at wavelengths of 1542.25 nm and 1543.75 nm. Using the PPLN waveguide, up to 0.5-nm idler separation was obtained.

To obtain widely separated multiple idler peaks, we performed a broadcasting experiments in an aPPLN, which has a broader SHG bandwidth. The 45-mm aPPLN waveguide was characterized for SHG using a single pump amplified by an EDFA. The input-output coupling loss for aPPLN waveguide is 12.6 dB. The peak SH conversion efficiency is -13.61 dB at 1534.34 nm with 24.06 dBm input pump power, giving a 17 %/W conversion efficiency for SHG over a 1-nm FWHM bandwidth. For the same length of waveguide, aPPLN gives lower conversion efficiency but a broader bandwidth than the PPLN. The broader bandwidth of SHG in aPPLN waveguide lets the two pumps be comfortably selected at wavelengths of 1533.59 nm and 1534.79 nm to obtain two SH and one SF peak farther apart for broadcasting with idler wavelengths separated distinctly. The red dashed-trace in Figure 4-12 depicts the normalized spectrum showing the wavelength broadcasting of the signal wavelength at 1537.44 nm to three idler peaks at wavelengths of 1529.81 nm, 1531.01 nm and 1532.15 nm having a spacing of around 1.2 nm, which is 140% wider, compared to the 0.5-nm spacing obtained using the fixed period PPLN waveguide. The conversion bandwidth refers to the bandwidth of the cascaded process i.e. tunability of signal wavelength, which is ~70 nm even for a uniform PPLN. However, it is the SH or SF bandwidth which decides the tunability of the pump wavelengths, to generate tunable idler for a fixed signal wavelength. For a uniform PPLN, the SH bandwidth of a 5cm PPLN device is usually 0.2 nm which restricts the pump to one particular wavelength. Broadband SHG or SFG response achieved in an aPPLN thus provides flexibility in selecting different pump wavelengths to get desired idler position or their mutual separation in a multicasting process.

4.6 Conclusion

In summary, same band wavelength conversion in the 1.55 μm wavelength range was achieved by the cascading of second order nonlinear processes of SHG/DFG and SFG/DFG in an MgO-PPLN waveguide. Ultra-broadband wavelength conversion over a 70 nm bandwidth in the cascaded SFG-DFG process was experimentally demonstrated in the 45-mm long MgO-PPLN waveguide. The 1.5-dB flattening of the conversion bandwidth in the C-band was experimentally

achieved by detuning of one of the pumps by only 150 pm, which could be useful for achieving balanced wavelength conversion in future optical communication networks. Also by utilizing simultaneous cascaded SFG-DFG and cascaded SHG-DFG, one signal was broadcast to three converted idlers by employing two adjacent pump lasers. The aPPLN waveguide gives widely separated idlers compared to PPLN waveguide, making it a better choice for all-optical network applications. However, merely 1 nm bandwidth of the aPPLN will not be sufficient to cover the whole C-band for WDM networks. The fixed pump wavelengths to satisfy QPM condition is a limitation due to which the signal can be converted to a particular set of wavelengths. There is a need of >30 nm SH/SF bandwidth for a PPLN device to achieve the flexibility of positioning pumps anywhere in the large bandwidth to obtain idlers at desired location in the C-band. The tunability of broadcast idlers based on two broadband QPM structures is addressed in the next two chapters.

CHAPTER 5
TUNABLE ALL-OPTICAL WAVELENGTH BROADCASTING IN A PPLN WITH MULTIPLE QPM PEAKS

5.1 Overview

Over the past decade, research on cascaded second-order nonlinear interactions in QPM-LN has been growing fast to satisfy the needs of high speed and large capacity optical networks [56, 77, 79, 121]. In chapter 4, we have shown frequency conversion of an input signal at frequency ω_s to an idler frequency ω_c located in the same band using cascaded nonlinear processes in a PPLN waveguide. In the first case, one pump laser at ω_{p0} was employed to generate the converted signal at $\omega_c = 2\omega_{p0} - \omega_s$ in cascaded second harmonic generation and difference frequency generation (cSHG/DFG). Secondly, using two pump frequencies ω_{p1} and ω_{p2} the signal was converted to a frequency $\omega_c = \omega_{p1} + \omega_{p2} - \omega_s$, based on cascaded processes of sum frequency generation and difference frequency generation (cSFG/DFG). Wavelength broadcasting was demonstrated by employing two pumps within the SH phase matching bandwidth of the PPLN to generate three waves by SH/SF process which lead to three idlers in a DF mixing process with the signal wave. However, the phase matching criteria of a periodic QPM structure limits the SH/SF bandwidth. This restricts the tunability of a cSHG/DFG or cSFG/DFG frequency conversion and eventually the broadcasting process. The bandwidth problem was earlier solved by Gong *et. al.* employing two pumps for cSFG/DFG within the 1.5-μm band so that one signal was simultaneously broadcast to seven fixed peaks in an MgO-PPLN owing to its broad 25 nm bandwidth in a type-1 QPM process [56]. For practical optical communication networks, tunability of wavelength broadcasting is essential to provide variable number and location of output channels. Further, reduced efficiency owing to the use of non-preferred nonlinear coefficient (d_{31}) in type-1 QPM needs to be overcome. We propose a solution for tunable wavelength broadcasting to several channels by using a grating structure with type-0 (using d_{33}) multiple QPM-SHG, which can be tuned by varying the temperature of the crystal to obtain efficient multiple peaks at different wavelengths [122]. Unlike using a type-1 process, utilizing a

type-0 process with appropriate temperature tuning, one can benefit from both the highest nonlinearity coefficient and tunable QPM bandwidth.

In this chapter, first, variable SHG-SFG is realized in a novel type-0 multiple-QPM structure using an engineered PPLN to generate one, two or three SH-SF peaks and second, its application in multiple-wavelength broadcasting is demonstrated by DFG mixing of a signal with the generated SH-SF peaks. Moreover, tunability of wavelength broadcasting to three idlers with the desired spacing and variable position of the destination channel for WDM is achieved by detuning the two pumps within the SFG bandwidth and making use of the dependence of the QPM efficiency curves on temperature tuning of a PPLN device for the assignment of the pump wavelengths.

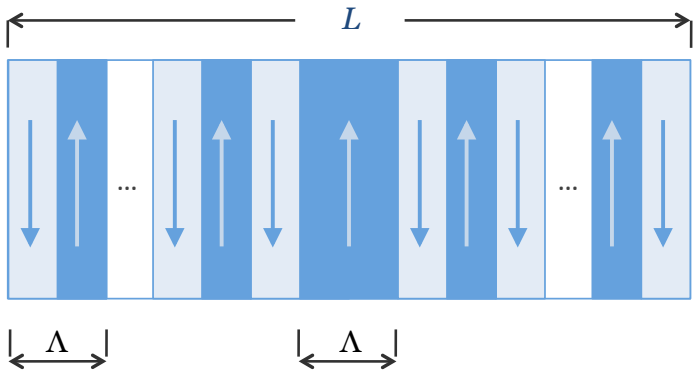

Figure 5-1: Schematic of a PPLN with an aperiodic domain in the center of the grating.

5.2 Multiple QPM structure in a type-0 PPLN

Besides the engineering of the effective nonlinearity, the advantage of QPM in materials such as lithium niobate (LN) is the access to its large d_{33} nonlinear coefficient, which can not be realized by birefringent phase-matching. In type-0 QPM process, the interacting fields propagate as extraordinary waves when polarized along the z-axis as $e + e \longrightarrow e$. An engineered phase-reversal QPM structure, used in the experiments in this chapter is shown in Figure 5-1.

This device has been fabricated by the room temperature electric field poling method described in the chapter 3. The period of the 1-cm-long PPLN is Λ = 18.5 μm with an aperiodic domain of

width Λ in the center. For a length, l of the grating and aperiodic domain in the middle at $l/2$ of the device, the variation of effective nonlinear coefficient along length, x is written as [123]:

$$\kappa(x) = d_{eff} \sin\left(\frac{2\pi x}{\Lambda}\right)\left[rect\left(\frac{x - l/4}{l/2}\right) - rect\left(\frac{x - 3l/4}{l/2}\right)\right] \tag{5.1}$$

where *rect* is the rectangular function. The SH amplitude, A_2 of the multiple-QPM PPLN device is then given by:

$$A_2(q) = iA_1^2 l d_{eff} e^{i\pi l\left(q \pm \frac{1}{\Lambda}\right)} \frac{\sin^2\left(\frac{\pi}{2} l\left(q \pm \frac{1}{\Lambda}\right)\right)}{\frac{\pi}{2} l\left(q \pm \frac{1}{\Lambda}\right)} \tag{5.2}$$

where A_1 is the FH amplitude, $q = (k_{2\omega} - 2k_{\omega})/2\pi$ is the phase mismatch, $k_{\omega,2\omega}$ are the wave numbers of FH and SH, and d_{eff} is the effective nonlinearity. The intensity, I can be calculated using $I = \frac{1}{2} c\varepsilon_0 n |A_2|^2$, where c is the speed of light, ε_0 is the free space permittivity, and n is the refractive index of the medium. This analysis will give two QPM peaks in SH spectrum with the maximum efficiencies at the pump frequencies ω_{p1} and ω_{p2}. In case of the cascaded SHG/DFG process using a signal frequency ω_s and pump at either of $\omega_{p1,p2}$ the idlers will be generated at $2\omega_{p1,p2} - \omega_s$. When two pumps are used, we also get cascaded SFG/DFG process generating an additional idler at $\omega_{p1} + \omega_{p2} - \omega_s$.

The temperature acceptance bandwidth for a QPM process can be obtained using the phase matching *sinc* term of SHG conversion efficiency considering the Sellmeier relation [72], which describes the refractive index dependence on the crystal temperature, and wavelength of the incident light. As a type-0 process has a wider temperature acceptance bandwidth than a type-1 process ($o + o \rightarrow e$) with proper tuning of temperature, the wavelength acceptance bandwidth in type-0 structure can be further improved.

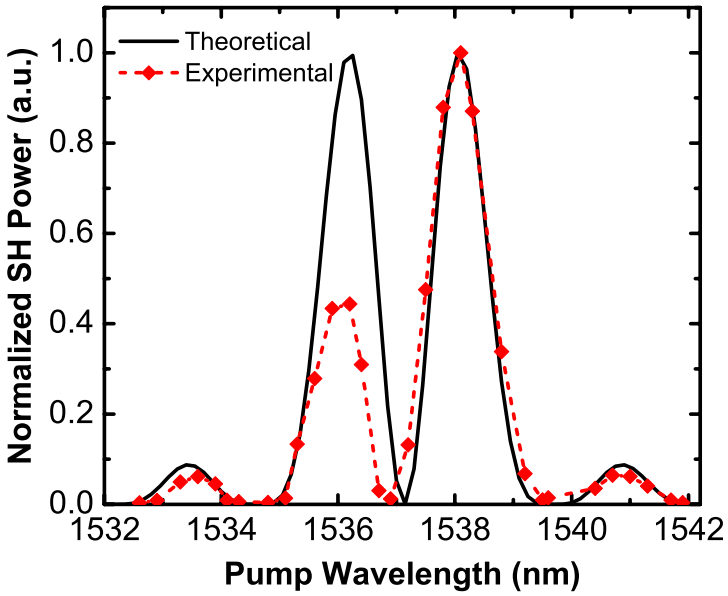

Figure 5-2: SH power vs. pump wavelength, theoretical (solid black) and experimentally observed (dotted, red) plots for the 2-peak QPM structure shown.

5.2.1 SHG and SFG characterization of multiple-QPM bulk PPLN

The maximum SHG power for each QPM peak of the phase-reversal PPLN in the plane wave approximation is calculated using the equation [70, 124]:

$$P_{SH} = \frac{8\pi {d_{eff}}^2}{\varepsilon_0 c n_{p1}^2 n_{SH} \lambda_{p1}^2 w_f^2} P_{p1}^2 l^2 \qquad (5.3)$$

Here, the pump wavelength is $\lambda_{p1} = 1538\,nm$, the effective nonlinearity coefficient of 2-peak QPM LN is: $d_{eff} = \sqrt{2}\,d_{33}/\pi = 10.6\,pm/V$, the free space permittivity is $\varepsilon_0 = 8.85 \times 10^{-12}\,F/m$, n_{p1} and n_{SH} are the refractive indices of LN at the FH and the SH wavelengths, respectively. For an input pump power $P_{p1} = 90$ mW, theoretical calculation gave a peak SHG power $P_{SHG} = 0.042$ mW or an efficiency of -33.32 dB. The SH bandwidth response was obtained by launching a tunable pump laser into the PPLN and measuring the output SH power for different wavelengths. Figure 5-2 (red-dashed curve) illustrates the normalized multiple-peak SH power for the characterized PPLN device showing two major QPM peaks for the pump wavelengths at 1536.1 nm and 1538.2 nm at 80°C, while the solid-black-curve depicts the

theoretically-calculated normalized SHG plot for such a device based on Eq. 5.2. The dual peak nature is attributed to the phase reversal due to the aperiodic domain in the center of the PPLN structure. Further a small deviation in the size of aperiodic domain from the poling period leads to the asymmetric peaks as seen in the experimentally obtained result. The maximum peak power at 1538.2 nm is 0.04 mW giving an efficiency of -33.58 dB (0.1%/W) which is in accordance with the calculated value.

The dual peak-structure was then employed to achieve SHG and SFG using two pump lasers. In the case when two pumps are set at each of the two QPM wavelengths, they result in two SH and one SF peak in between, however, with uneven powers. This is shown in Figure 5-3 (blue dashed trace) with the input wavelengths of 1536.1 nm and 1538.2 nm. Tuning one of the lasers to the dip (1536.88 nm) in the center of two-peak SHG spectrum of Figure 5-2 results in the suppression of the short-wavelength SH peak as shown in Figure 5-3 by red dotted trace; the two peaks (1 SF, 1 SH) obtained here are separated by 0.3 nm. The peak separation and relative efficiency are varied by slightly detuning the input wavelengths. By moving either of the lasers out of the SH and SF bandwidth, a single SH peak (e.g. Figure 5-3 green trace) is achieved.

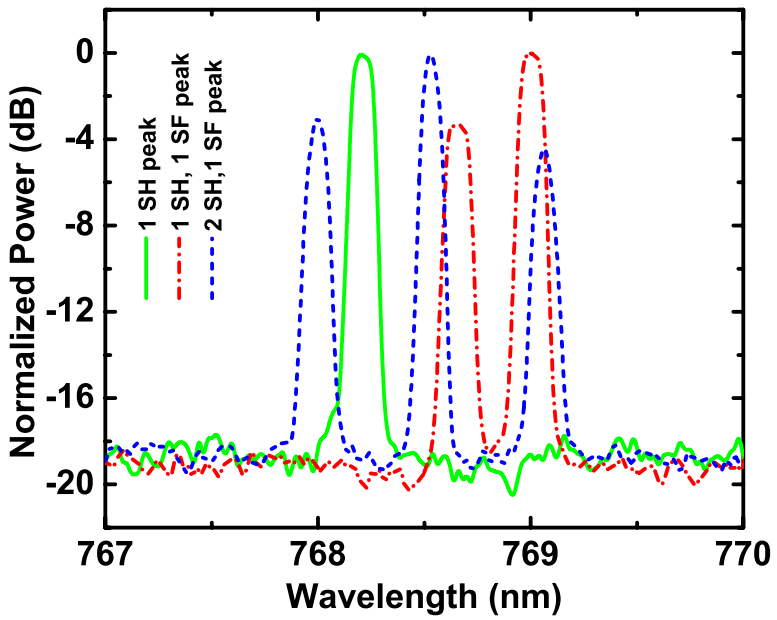

Figure 5-3: Spectra of multiple SHG-SFG for the different cases of 2 SH and 1 SF output (blue dashed); 1SH and 1SF (dash-dotted red curve); 1SH peak (green solid trace).

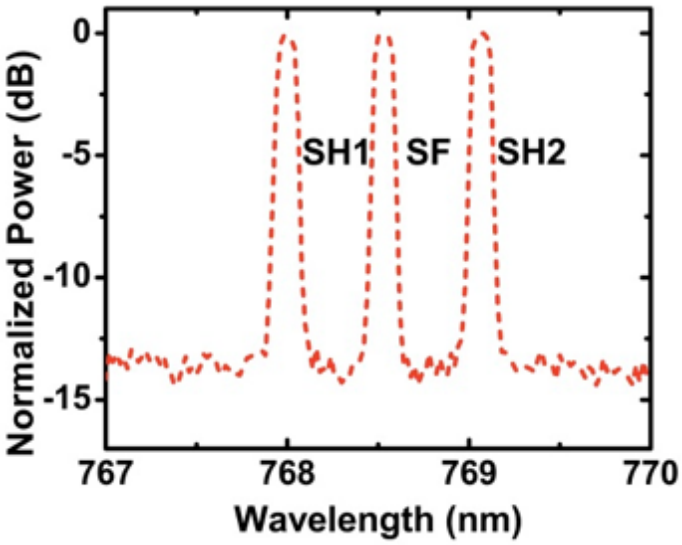

Figure 5-4: Spectrum of multiple SHG-SFG showing equalized peak powers achieved by pump detuning; mutual spacing of the SH/SF peaks is 0.55 nm.

The SH and SF powers were equalized by slightly detuning the wavelength and varying the power of input pumps, as illustrated in Figure 5-4. Here, the two pumps are set at 1536.14 nm and 1536.28 nm, a slight deviation from their QPM wavelengths. Moreover, adjusting the polarization controller also helped in establishing the equalized SF/SH peak powers.

5.2.2 Temperature dependence of SHG and SFG in multiple-QPM PPLN

The effective refractive indices n_o and n_e of the PPLN depends on the temperature of the PPLN device given by the Sellmeier equations described in chapter 2 [72]. Due to this refractive index dependence on temperature, the QPM condition for efficient SHG/SFG changes with temperature. In PPLN, the phase matching condition shifts to longer wavelengths by heating and to shorter wavelengths when the device is cooled down. Figure 5-5 demonstrates the three peaks of SH-SF response of the fabricated PPLN device at two different temperatures by launching two pump lasers. A constant 1.2-nm wavelength difference of pumps is maintained. The blue solid curve shows the three SH-SF peaks when the input pump wavelengths are set at 1537.3 nm and 1538.5 nm with the device temperature at 81.5 °C; the pink dashed trace depicts the three

wavelength-shifted SH-SF peaks at 84.5 °C when the two pumps are set at 1538.5 nm and 1539.7 nm. Thus, when each pump is shifted by 1.2 nm with the appropriate temperature tuning, it leads to a shift of 0.6 nm in the SH-SF spectrum.

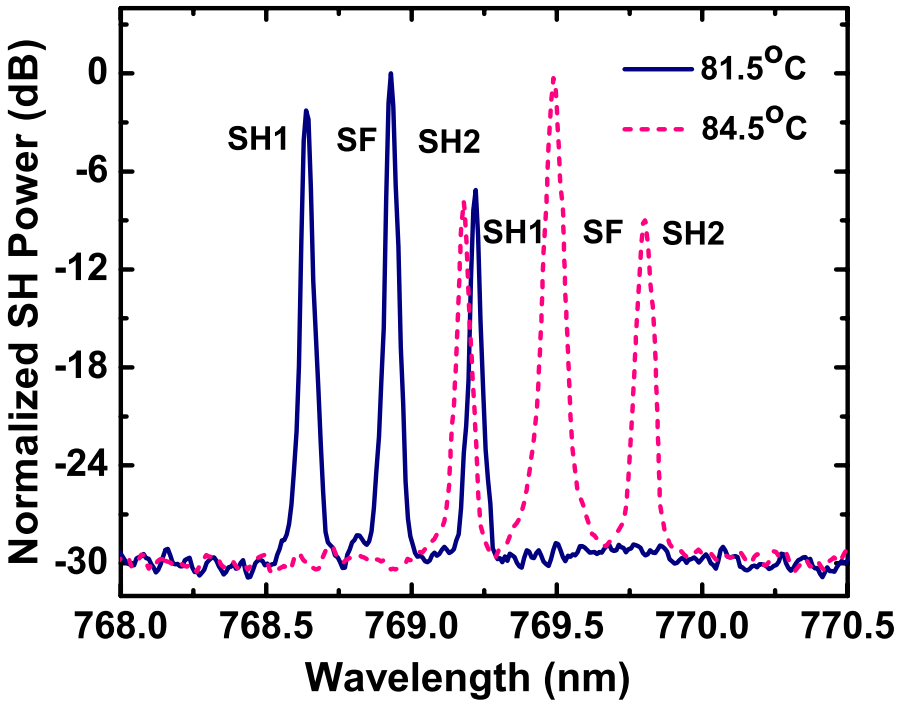

Figure 5-5: Spectra of three SH-SF peaks showing 0.6 nm peak-wavelength shift over a 3°C temperature difference when the two pump wavelengths were simultaneously shifted from 1537.3 nm and 1538.5 nm to 1538.5 nm and 1539.7 nm.

5.3 Cascaded SHG-SFG/DFG in multiple-QPM bulk PPLN

Wavelength conversion based on cascaded second order nonlinear interaction in QPM devices are attractive for signal processing in all-optical networks. The cSHG/DFG and cSFG/DFG processes and their QPM conditions have been described in chapter 4. Figure 5-6 shows the experimental setup used for c(SHG-SFG)/DFG in which two tunable lasers are employed as pumps, operating within the C-band. They are combined by a WDM coupler and then amplified by a Pritel high-power EDFA. The amplified lightwaves, passing through a polarization controller are confocally focused using a lens into a 10-mm-long bulk z-cut multiple-QPM PPLN. This corresponds to a loose focusing condition for SHG. The phase-reversal PPLN sample

is temperature controlled for tuning the operating wavelengths and maximizing the conversion efficiency. A temperature tuning coefficient of 0.3 nm/°C for the PPLN device was observed in the wavelength conversion experiments described in this chapter. A 9.5 dB filter is used for high input powers beyond 100 mW to avoid damaging the detector. The diameter of the input lights is $w_0 = 1.83\ mm$ which is focused in the center of the PPLN to a beam-waist of $w_f = 50\ \mu m$ using a 10-cm focal length lens. The confocal length parameter of focused beam equals to the length l=1cm of the PPLN. The output lights are coupled to a spectrum analyzer via a 30x Newport objective and a multimode fiber, for which the coupling loss of the setup is 1.5 dB.

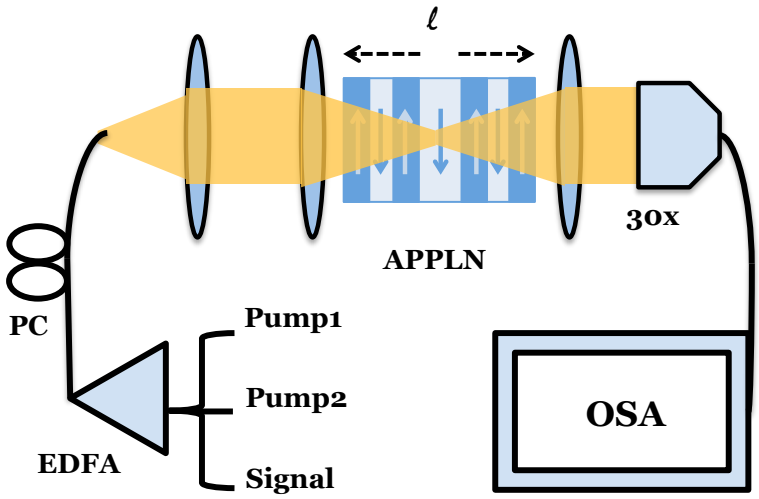

Figure 5-6: Experimental setup for cSFG/DFG with two pumps and a signal, PC: Polarization Controller, OSA: Optical Spectrum Analyzer. For SFG, just the two pump wavelengths are coupled into the setup. PPLN with a central aperiodic domain having width equal to size of the device period is shown.

In the dual-peak PPLN grating, difference frequency mixing of a C-band signal wavelength with the multiple SH-SF peaks generated from the two pumps in the C-band gives multiple idlers in the same band. The output power of the SF wave is twice the SH wave for equal-power pumps; e.g. for the two pumps with powers of 182 mW and 145 mW, respectively, the SF power obtained is $P_{SFG} = 16\pi d_{eff}^2 P_1 P_2 l^2 / (\varepsilon_0 c n_1 n_2 n_{SF} \lambda_1 \lambda_2 \omega_f^2)$ and is equal to $2\kappa P_1 P_2 l^2 = -2.63\,\text{dBm}$. The cascaded SFG/DFG output can then be calculated as: $P_{SFG/DFG} = \kappa P_{SFG} P_{signal} l^2 = -38.2\,\text{dBm}$,

considering the input P_{SFG} = average of SFG over half-length of the PPLN and P_{signal} = 14.3 dBm. The experimentally observed efficiency of ~-53.2 dB is thus comparable with the calculated efficiency of -52.5 dB. The experimental result of three idler generation is illustrated in Figure 5-7 where one signal at 1546.46 nm is converted to three idlers spaced ~ 2.0 nm each around 1528.7 nm in a cSHG-SFG/DFG process employing two pumps at the QPM peaks with a mutual spacing of 2.0 nm.

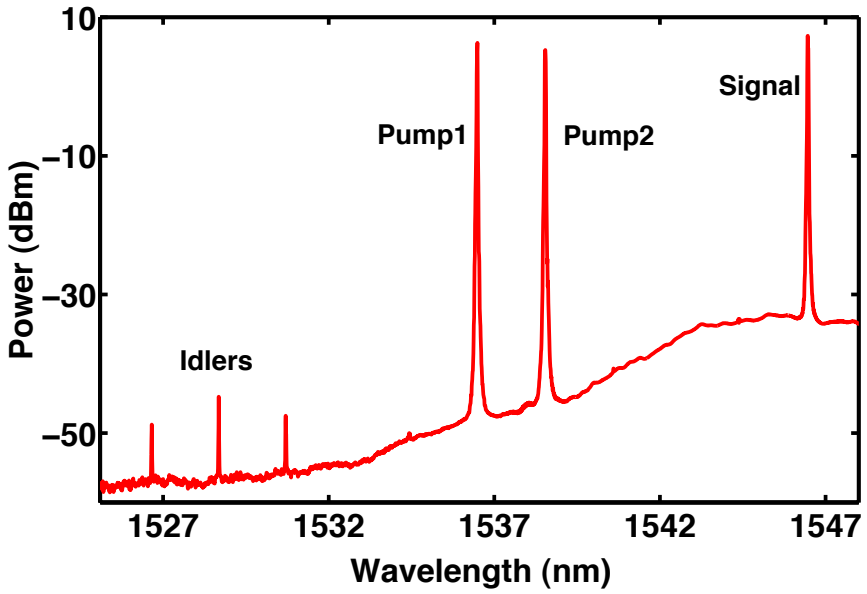

Figure 5-7: Experimentally observed spectrum of triple idler generation in the two-peak PPLN structure of a signal at 1546.5 nm to idlers at 1526.65 nm, 1528.68 nm and 1530.70 nm via cSHG/DFG and cSFG/DFG using two pumps at wavelengths 1536.48 nm and 1538.54 nm.

5.4 Tuning the idler spacing by pump detuning

The schematic of tuning the mutual spacing of the three broadcast idlers via cSFG-SHG/DFG by employing pump detuning in the SFG bandwidth is represented in Figure 5-8, where the change in the pump wavelengths is reflected identically in the three idlers. To demonstrate this experimentally, we set the two pumps within the two QPM peak bandwidths (around i.e. 1536.1 nm and 1538.2 nm, at 80°C) resulting in two SH peaks and one SF peak in between. The

channels for the WDM network considered here, are separated by 50 GHz (~0.4 nm) in the C band. DF mixing of a signal wavelength at 1545.3 nm with the three SH-SF peaks gives three idlers.

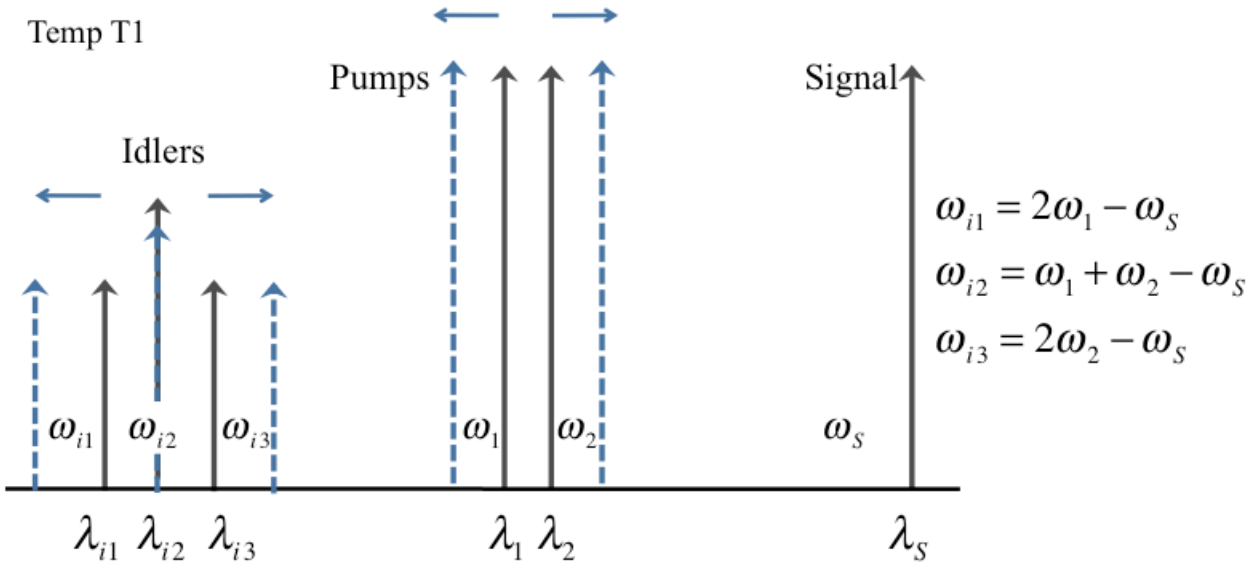

Figure 5-8: Scheme for tunable broadcasting of a signal into three idlers by detuning of the pump wavelengths.

Keeping the signal wavelength fixed, the desired wavelength spacing between the idlers is obtained by tuning of pump wavelengths around the QPM peaks of SH wavelengths. We have successfully varied the spacing from 0.4 nm to 4 nm between the idlers in steps of 0.4 nm, without registering significant loss in the idler efficiency, so that the idlers can be directed over 10 adjacent WDM channels on either side of the central idler. For example, Figure 5-9 illustrates the cases for idler spacing of 0.4 nm, 1.2 nm, 2.4 nm and 3.6 nm, while keeping the signal wavelength fixed. Employing a chirped dual-peak QPM device in which we get broader bandwidth of SHG response, many more WDM channels can be covered in terms of idler spacing.

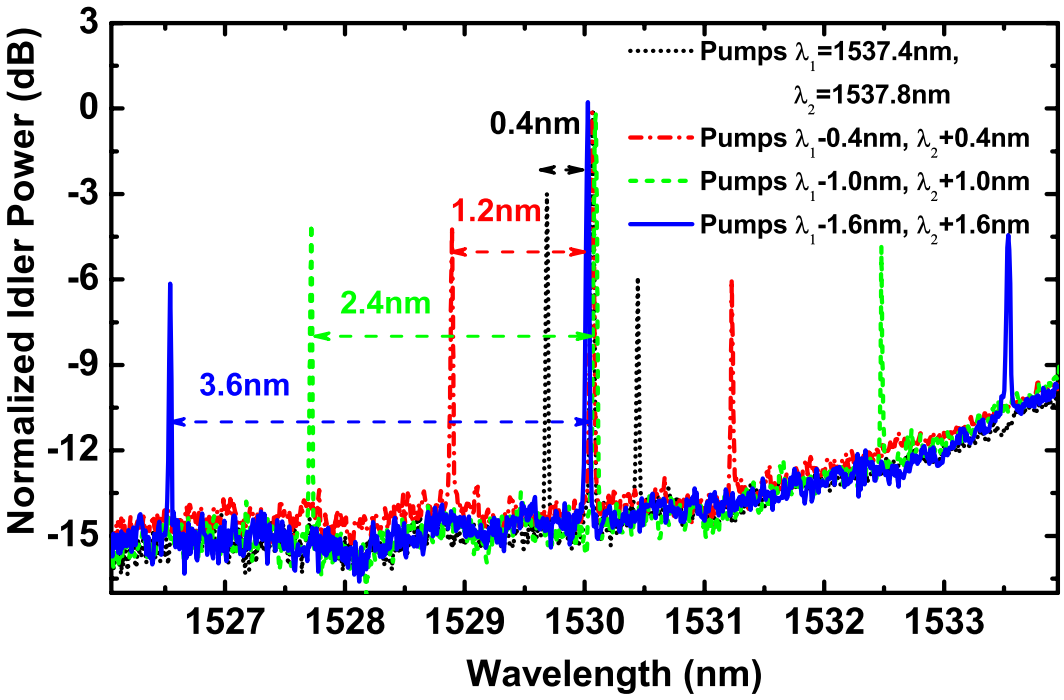

Figure 5-9: Spectral variation of idler spacing with detuning of both pump wavelengths, keeping signal fixed at 1545.3 nm.

In the above case of Figure 5-8 and 5-9, both the pumps were detuned towards or away from their respective QPM peak centers by same frequency detuning $\delta\omega$ (i.e, $\omega_{p1}-\delta\omega$ and $\omega_{p2}+\delta\omega$), so that their SFG remains fixed at $\omega_{p1}+\omega_{p2}$ after detuning and hence the corresponding central idler remains fixed in one channel. The idlers on either side however shift as they correspond to the SHG of the two pumps and the two new WDM channels are now broadcast on either side of the same central idler (channel).

There are, however, two other possibilities which require fixing one of the two pumps and tuning the other so that either the left or the right idler lies in same channel while the other two are navigated to subsequent channels as shown in the schematic of Figure 5-10. These experiments were performed, as illustrated in Figure 5-11 where the idler spacing of 0.4 nm, 2.0 nm and 3.6 nm has been obtained by tuning one pump around ω_2 while keeping the frequencies of signal and another pump fixed at ω_S and ω_1, respectively. Here, the green trace shows the three idlers for pumps at wavelengths 1537.0 nm and 1537.4 nm at a single channel separation, and the signal

at wavelength 1545.3 nm. The blue dashed and pink dotted plots show the idlers obtained by tuning the second pump further by 1.6 nm and 3.2 nm so that the idlers are mutually separated by 5 and 9 channels respectively.

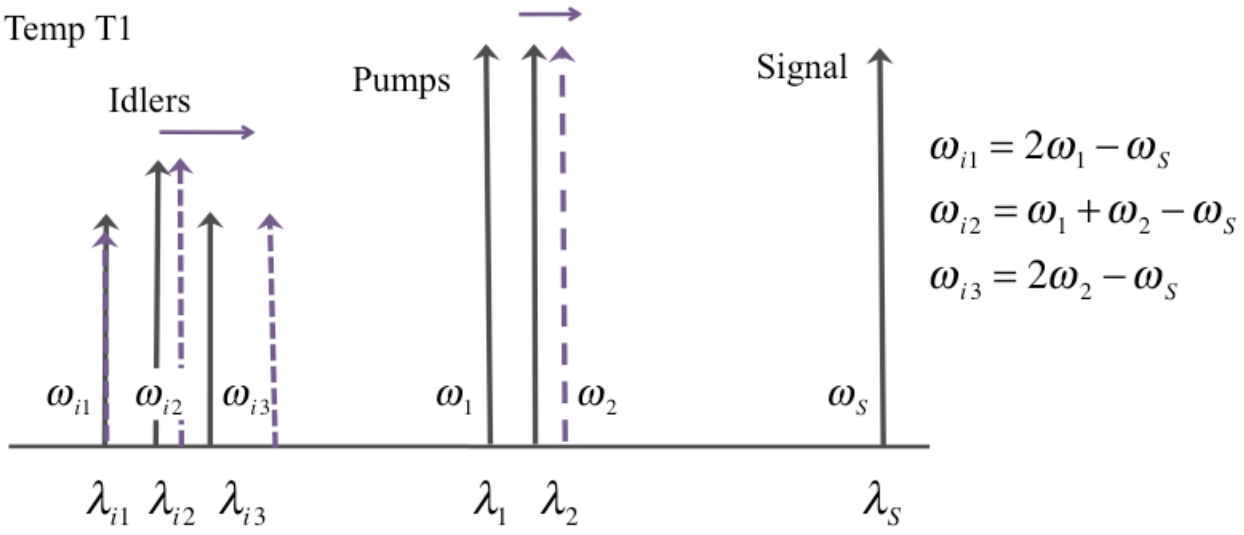

Figure 5-10: Scheme for tunable broadcasting of a signal into three idlers by detuning of one pump wavelength.

5.5 Tuning the idler position with temperature tuning

As shown in section 5.4, the number of channels across which the multiple-idlers can be swept depends on the SH bandwidth of the device. It is advantageous to have a chirped device in such a situation. However, employing temperature tunability to shift the QPM peaks will provide the desired flexibility and tunability for directing idlers across all WDM channels, as detailed in the following. Figure 5-12 shows a schematic of the temperature-assisted tunable broadcasting of a signal into three idlers based on cascaded SHG-SFG/DFG in our proposed PPLN device. The phase-matched wavelengths for the QPM processes in PPLN vary due to temperature dependence of the refractive indexes given by the Sellmeier Eq. [72]. The pumps can be tuned to a longer wavelength by increasing the temperature from T1 to T2 and thereby tuning the idlers to longer wavelengths. For example, considering two pumps with constant 1.2-nm wavelength spacing at T1, the three-idler broadcasting will place the idlers at WDM channels *1, 4* and *7*. Increasing the

temperature to T2 by 4.8°C for a new tuning of the pump wavelengths (shift of 1.6 nm) will locate the idlers at the next channels *5, 8* and *11*; and so on.

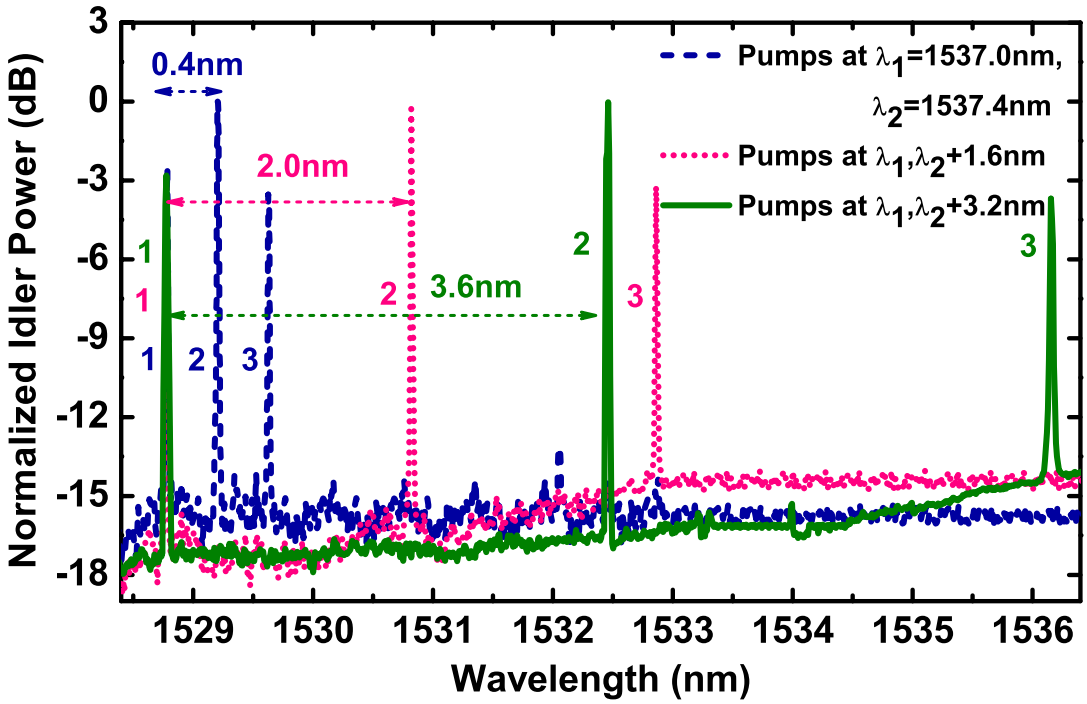

Figure 5-11: Spectral variation of idler spacing with pump wavelengths separation by tuning just one pump wavelength.

Figure 5-13 shows the spectra of idlers generated when the device is set at four different temperature values. The blue dashed curve corresponds to the case when the pumps are set at 1536.95 nm and 1538.15 nm separated by 1.2 nm at 78.2°C. Increasing the temperature by 4.8°C to 83.0°C shifts the phase matching wavelengths by 1.6 nm so that the idlers are also shifted by the same amount, shown by the red solid curve in Figure 5-13. Similarly, when the temperature is set at 86.5°C, the idlers experience a total shift of 3.0 nm as depicted by the black dotted curve and for 89.0°C the idlers have shifted by 4.4 nm shown by the green dash-dotted curve in Figure 5-13.

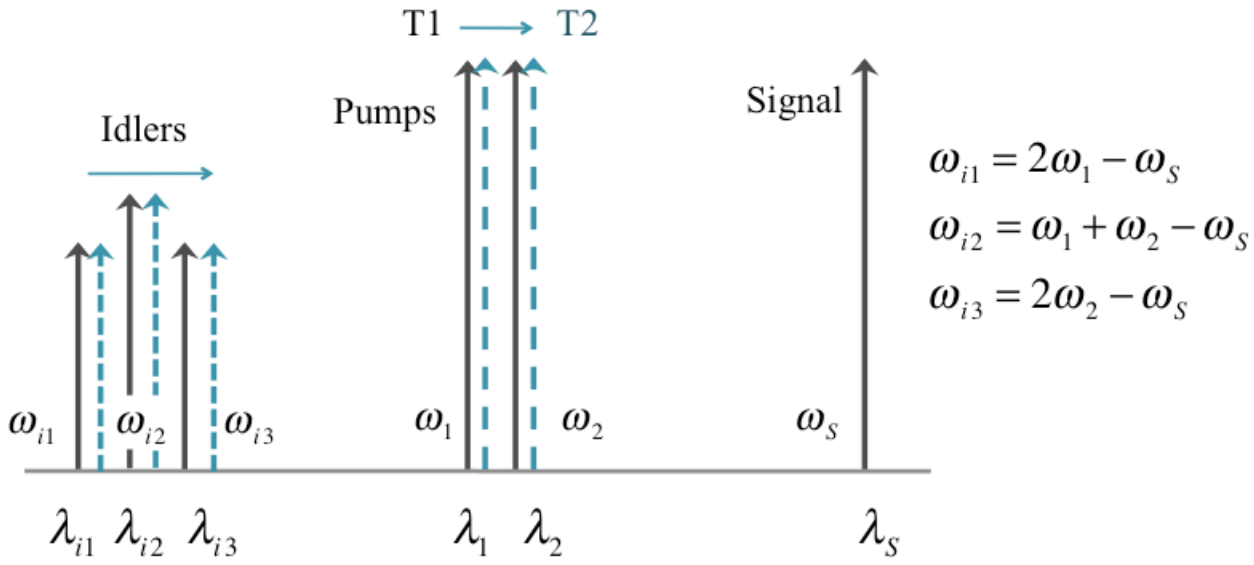

Figure 5-12: Scheme for tunable broadcasting of a signal into three idlers by temperature-assisted pump-wavelength tuning.

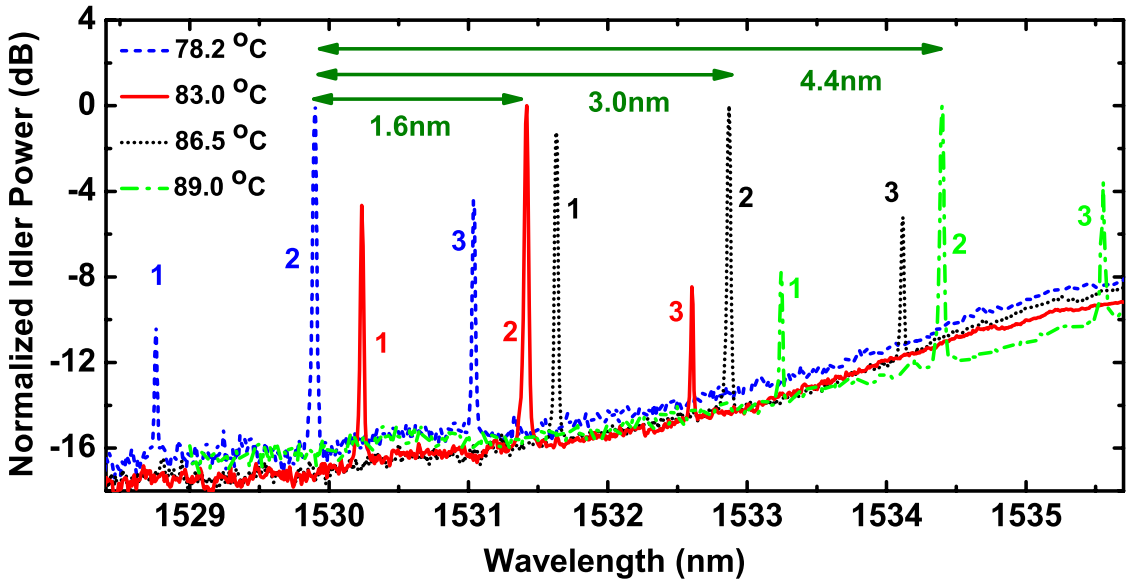

Figure 5-13: Tunable triple-idler broadcasting of a signal at 1545.27 nm with shifting the two-pump wavelengths at 1536.95 nm and 1538.15 nm by +1.6 nm, +3 nm and +4.4 nm and simultaneous temperature tuning from 78.2°C by +4.8°C, +8.3°C and +10.8°C.

Hence, tuning the temperature by ~10°C shifts the idlers by 4.4 nm to be positioned at WDM channels *12, 15* and *18*. Employing temperature tuning, we observed no degradation in the response of PPLN in terms of idler efficiency.

Using this device, an overall idler wavelength shift of less than 10 nm by selecting pumps at desired wavelengths obtained via temperature tuning, is sufficient to cover up to 40 WDM (50 GHz spacing) channels for multiple idler broadcasting. The location of idlers can thus be varied by slightly tuning the input pump wavelengths within the device's QPM bandwidth using temperature tuning. Based on these results, we can simply predict that the flexibility of broadcasting using the cSHG-SFG/DFG scheme to multiple channels can be extended to cover the entire C-band by tuning the temperature of a chirped multiple-QPM PPLN device. The time taken by the HC Photonics oven to raise the temperature of 10 mm × 10 mm × 0.5 mm PPLN device by 1°C was 0.26 ms. The temperature tuning in our experiments is thus relatively slow for ultrafast applications in optical networks, in general, but can be implemented in WDM switching devices, which do not require ultrafast dynamic reconfigurations and where this temperature response time is acceptable.

5.6 Conclusion

In this chapter, for the first time, tunable wavelength broadcasting was demonstrated in a 10-mm long multiple-QPM LN where one signal was successfully broadcast into three idlers based on cascaded type-0 SHG-SFG/DFG in the novel PPLN device for which three SH-SF peaks were achieved. The number of SH/SF peaks were also varied by positioning the two pump wavelengths in the dual peak of the phase-shifted PPLN or positioning one pump at the minima of SH response in between the two peaks. In the three idler broadcast, the mutual spacing of idlers in the WDM grid was adjusted by detuning of the two pump wavelengths within the bandwidth of the device. The temperature tunability of the multiple-QPM PPLN device assists in the choice of suitable pump wavelengths for tunable wavelength broadcasting by positioning the idlers at desired destination channels in WDM networks. Our experimental results indicate that an overall idler wavelength shift of less than 10 nm realized by selecting pump wavelengths via temperature tuning, is sufficient to cover up to 40 WDM channels for multiple idlers broadcasting. In comparison with the fixed spacing of the three idlers in the PPLN described in chapter 4, the dual-QPM peak device is therefore of immense importance for flexible network

construction by providing an effectively larger bandwidth obtained by pump detuning and temperature tuning. Channel selective multiple broadcasting achieved by this scheme proves its crucial function in signal path routing enabling the effective usage of WDM bandwidth and flexible network construction. However, for ultrafast network applications the slow speed of temperature tuning will be a constraint. Therefore, in the next chapter, a temperature independent tunable wavelength broadcast scheme is proposed and demonstrated using a step-chirped PPLN having an inherently broad SH bandwidth.

CHAPTER 6
TUNABLE WAVELENGTH BROADCASTING IN A BROADBAND STEP-CHIRPED PPLN

6.1 Overview

All optical wavelength conversion and multicasting can effectively resolve contention and increase network throughput for high bandwidth applications in communication networks [54, 56, 84, 86, 125]. Tunability of conversion over the communication band is an important requirement for QPM nonlinear devices to be fully capable for all-optical wavelength conversion and broadcasting in large capacity optical networks. We have seen in the chapter 5 that to address the needs of a tunable broadband wavelength conversion device, a temperature-tuning scheme was used for a broadened twin-peak QPM bandwidth of a type-0 PPLN device. Employing two pumps simultaneously in the phase-shifted PPLN device, tunable broadcasting to multiple peaks was demonstrated by shifting the idler location and their mutual spacing across the C-band.

Even though the device was a significant improvement over previous demonstrations of narrowband type-0 conversion or a broad but inefficient type-I conversion, the slow speed of temperature tuning can be a deterrent for ultra-fast WDM networks. The use of a chirped grating structure for SHG instead of a uniform period offers the benefit of a larger conversion bandwidth while employing the highest nonlinear coefficient d_{33} in a type-0 QPM interaction [25, 30, 87, 126, 127]. A chirped device, therefore, can easily overcome the problem associated with the need for temperature tuning to achieve broader bandwidth in a uniform QPM device. Fabricating a grating with a continuous chirp is difficult due to the small change in the period, therefore, a step-chirped grating with almost similar bandwidth response can be used for broadband applications [30, 85].

In this chapter, we have shown broadband conversion in an exclusively designed, broadband, step-chirped (SC) PPLN. The pump wavelengths can be freely tuned over the broad ~28-nm SH bandwidth of the SC-PPLN device overlapping the 1.55-μm communication band. Tunable multi-channel broadcasting of a signal into variable destination channels is then demonstrated based on

cSHG/DFG and cascaded sum and difference frequency generation (cSFG/DFG) employing two pump lasers in the SC-PPLN.

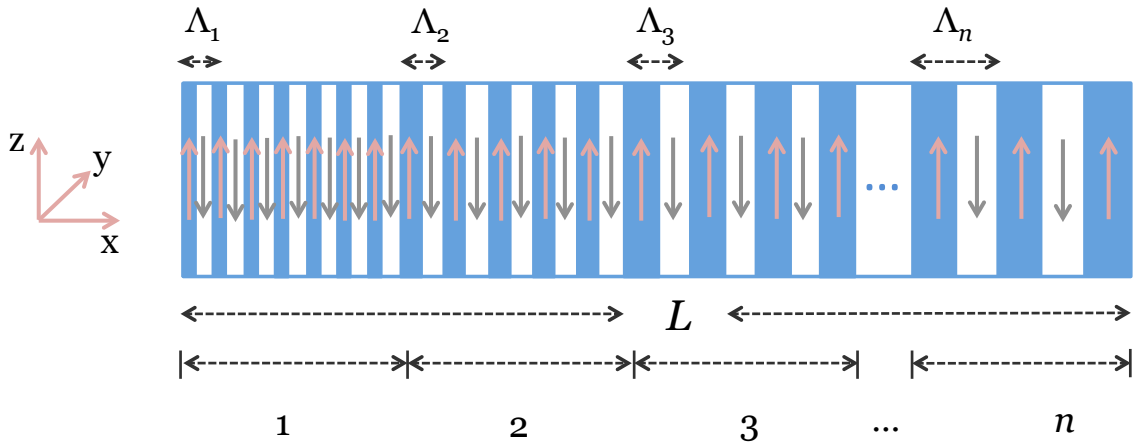

Figure 6-1: Schematic of a step-chirped PPLN grating showing n sections of increasing periods Λ_i. The reverse poled domains are shown by alternate direction of arrows. The grating channel is along the x-axis of a z-cut LN sample.

6.2 Design of step-chirped PPLN

A chirped grating is described as an aperiodic grating structure with continuously increasing or decreasing periods. This leads to broadening of the QPM bandwidth that solves the problems associated with loss in efficiency due to laser wavelength fluctuations or temperature instability. However, owing to the limitations associated with fabricating small changes in a linearly chirped grating structure, a step-chirped grating with cascading of uniform gratings with stepwise increase in their periods was employed [85]. It has been shown that appropriately designed step-chirped (SC) gratings has almost the same bandwidth and efficiency as that of linearly chirped gratings while providing significant advantage in terms of fabrication [46].

The schematic diagram of a SC-PPLN device is shown in Figure 6-1 where the length of the grating is divided into n equal sections, each consisting of a uniform grating of period Λ_i with 50% mark-space ratio of the poled and un-poled regions. Each section of step chirped PPLN is phase matched at different wavelengths leading to a broad SH conversion bandwidth. The step

change or chirp introduced in the periods of consecutive sections is $\Delta\Lambda$, so that the period of i^{th} section is related to the first period by the following equation:

$$\Lambda_i = \Lambda_1 + \Delta\Lambda(i-1) \tag{6.1}$$

The total SH amplitude is obtained by solving the nonlinear coupled equations for each section successively considering the pump and SH output of previous section as input fields for the next section. The QPM condition for a type-0 interaction in each section of SC-PPLN of period Λ_i is given by:

$$k_{2\omega} - 2k_{\omega} = 2\pi / \Lambda_i \tag{6.2}$$

where k_{ω} and $k_{2\omega}$ are the propagation constants for pump and SH waves, respectively. In the plane wave approximation and assuming non-pump depleted case, the maximum SH power for each section of a *n*-section step chirped PPLN can be calculated using

$$P_{SH} = \kappa P_p^2 (L^2 / n^2), \tag{6.3}$$

where

$$\kappa = 8\pi d_{eff}^2 / (\varepsilon_0 c n_p^2 n_{SH} \lambda_p^2 w_f^2), \tag{6.4}$$

and λ_p is the pump wavelength. The effective nonlinear coefficient of each section is $d_{eff} = \frac{2d_{33}}{\pi} = 15\ p\text{m/V}$, the free space permittivity is $\varepsilon_0 = 8.85\times10^{-12}$ F/m, speed of light in vacuum $c = 3\times10^8$ m/s, the confocal beam waist $w_f = 50\ \mu$m, n_p and n_{SH} are the refractive indices of LN at the pump and the SH wavelengths, respectively. The SH bandwidth of the SC-PPLN depends on various parameters such as number of sections *n*, length of each section, step change in the period of section $\Delta\Lambda$ etc..

The SC-PPLN device used for the wavelength broadcasting experiments in this chapter consisted of ten equilength sections in a 20-mm-long grating with the periods varying from 18.2 μm to 19.1

μm to generate a broadband SH response covering the optical C-band. The delicate fabrication of the step-chirped PPLN device was then done at room temperature using the liquid electrode poling method described in chapter 3.

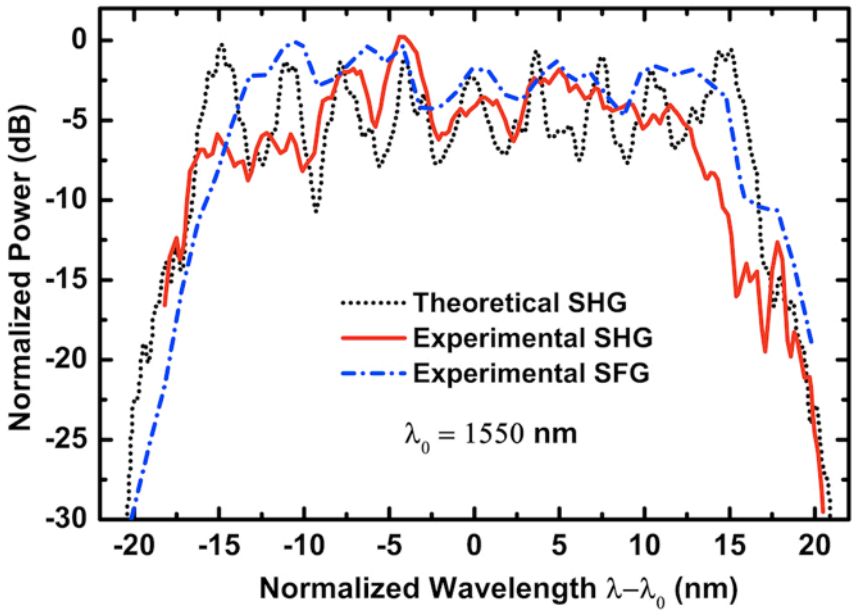

Figure 6-2: Experimental and Theoretical SH, and experimental SF intensity response achieved by pump tuning.

SH characterization

The SC-PPLN sample was placed in a oven at a controlled temperature of 125 °C, to avoid photorefractive damage, for characterizing its SH response and achieving the wavelength conversion through cascaded SHG/DFG. A tunable pump laser operating within the C-band and amplified by an EDFA is employed for generating SH power. The amplified pump is passed through a polarization controller and loosely focused into the PPLN device using a 10 cm lens. The SH output is measured using an optical spectrum analyzer by tuning the pump wavelength over the communication band. Figure 6-2 (red solid curve) illustrates the normalized SH power versus pump wavelength for the SC-PPLN device showing a 28-nm-wide bandwidth (for maximum peak-to-peak ripple), while the black dashed curve depicts the theoretically-simulated normalized SH power with a 30-nm-wide bandwidth, which was the basis for the design of the

device. For an input pump power, P_p = 0.66 W, used in the characterization experiments, the theoretical calculation with Eq. 6-3 gives a peak SH power, P_{SHG} = 0.22 mW, or an efficiency of −34.78 dB. The experimentally observed peak power of the 10-section 20-mm-long SC-PPLN is ~0.21 mW and the efficiency is ~−35 dB.

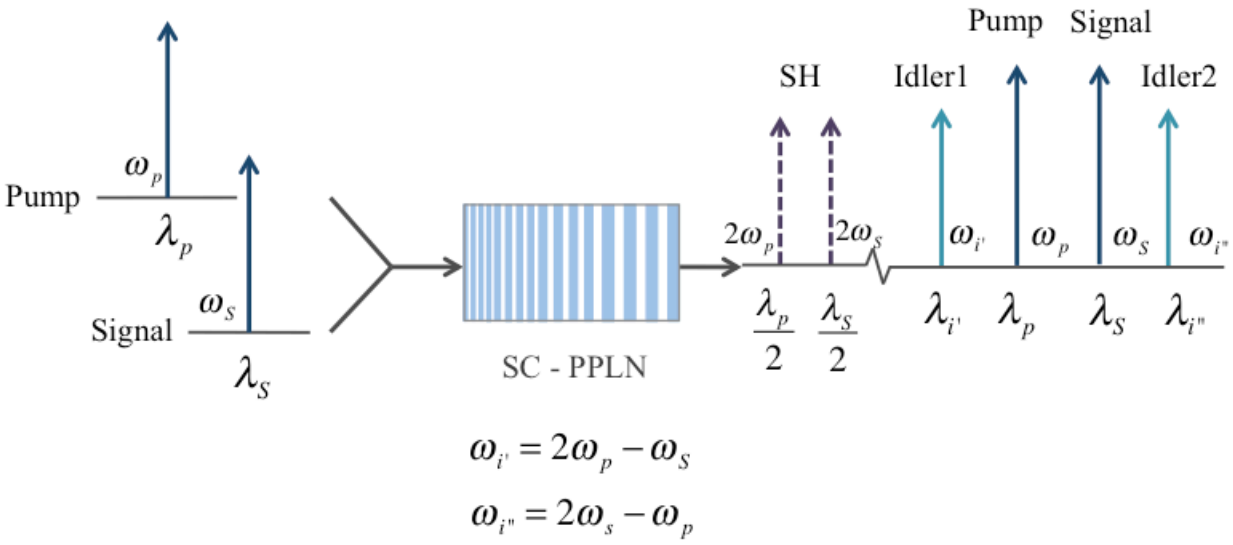

Figure 6-3: Schematic of dual idler conversion based on cSHG-DFG in a SC-PPLN

For generating SF, two pump lasers were simultaneously launched into the SC-PPLN. The SF power of the SC-PPLN shown by the blue dash-dotted curve is obtained by tuning one pump over the C band while keeping the other pump fixed at 1550 nm. The SF bandwidth is measured to be ~30 nm. The experimentally observed SH and SF power have similar features as the simulated one but with a comparatively smaller bandwidth, which is due to the errors involved in the poling process. In fact, due to the constraints of minimum step change in period possible in the mask fabrication at Polytechnique, the number of sections was less than the optimum value. This explains larger ripples in the SH bandwidth, which may be reduced in the future by increasing the number of sections and reducing $\Delta\Lambda$ [30, 88]. Apodizing the step-chirped PPLN devices by increasing and decreasing patterns of duty ratios along the grating length has also been proposed to reduce the ripples further in the SH response [30]. Nevertheless, in the next sections, employing the broadband SC-PPLN device, tunable wavelength conversion and broadcasting of a

signal in the C-band is experimentally demonstrated based on cascaded SHG/SFG-DFG processes.

6.3 Single to dual channel conversion based on cSHG-DFG

The experimental setup used for cSHG/DFG has two tunable lasers operating within the C-band employed as pump and signal wavelengths. The schematic description of dual idler generation is shown in Figure 6-3. Here, pump and signal frequencies are represented as ω_p and ω_s respectively. Since the pump and the signal both lie in the SH bandwidth of SC-PPLN, each generates a SH wave in the 775 nm band at respective frequencies $2\omega_p$ and $2\omega_s$. Based on the DF mixing of the signal frequency and the SH of pump frequency, the signal is converted to a primary idler at frequency

$$\omega_{i'} = 2\omega_p - \omega_s$$

or, wavelength

$$1/\lambda_{i'} = 2/\lambda_p - 1/\lambda_s. \qquad (6.5)$$

In the case of a uniform PPLN, the SH bandwidth is narrow and just the pump frequency is located in that bandwidth while the signal frequency is placed out of this narrow bandwidth. However, in the case of the step chirped PPLN with an SH bandwidth almost covering the whole of the C-band, the signal channel also falls within the SH conversion bandwidth. Thus, in addition to the primary idler mentioned earlier in Eq. (6.5), the signal is also converted to a secondary idler at frequency

$$\omega_{i''} = 2\omega_s - \omega_p$$

or, wavelength

$$1/\lambda_{i''} = 2/\lambda_s - 1/\lambda_p. \qquad (6.6)$$

when the SH of the signal mixes with the pump frequency via a DFG process.

The experimental demonstration of dual idler broadcast was performed for a fixed signal wavelength and a pump laser tunable over the C-band. The input pump power measured after the

EDFA was 720 mW while the amplified signal power was 920 mW. Figure 6-4 demonstrates the dual idler broadcasting for the signal fixed at 1552.0 nm and the pump wavelength tuned from 1550.8 nm to 1542.8 nm. Six overlapping spectra of dual idler broadcasting, normalized to the EDFA ASE noise, are shown in Figure 6-4, in which a pump tuning over 8 nm results in a single-to-dual-channel conversion over nearly 30 nm spanning across the C band.

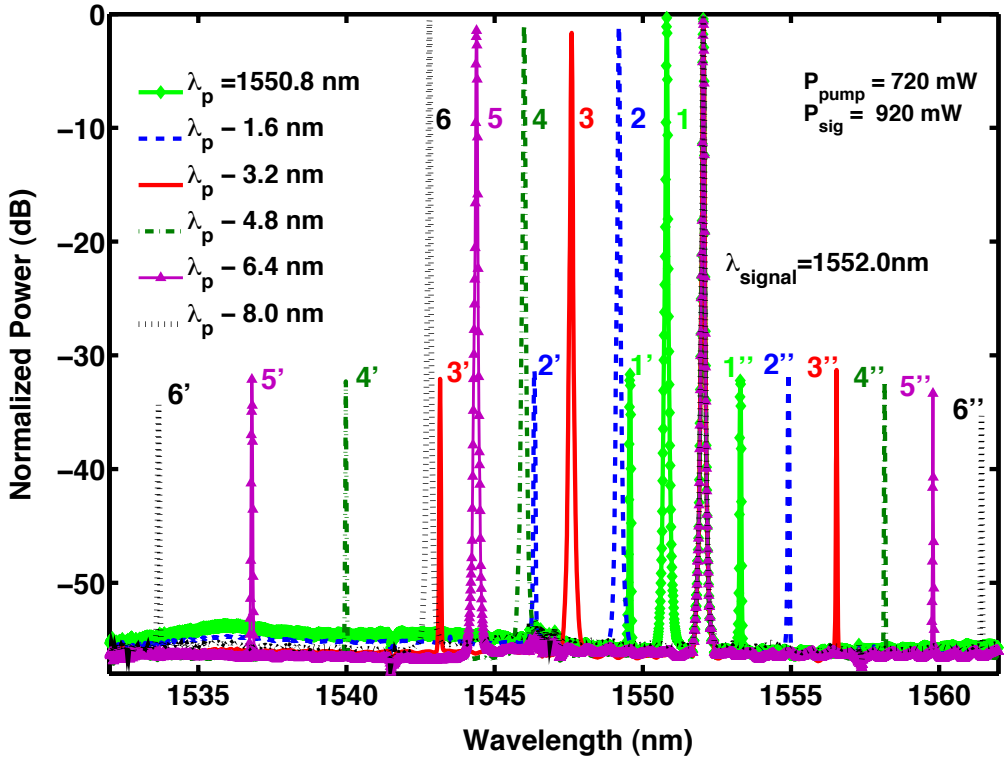

Figure 6-4: Overlap of six experimentally observed spectra for converting a fixed signal wavelength at 1552.0 nm to dual-idler wavelengths numbered i' and i'' by tuning the pump wavelength over 8 nm located at wavelengths numbered i, for i = 1 to 6.

For the signal at 1552.0 nm and the pump at 1550.8 nm the two idlers are obtained at 1549.6 nm and 1553.2 nm, lying symmetrically about the center of the pump and signal wavelengths, as shown in the green solid line with diamond markers in Figure 6-4. In the second trace shown by the blue dashed line, the pump is shifted by -1.6 nm to 1549.2 nm, giving idlers at 1546.4 nm and 1554.8 nm at a shift of -3.2 nm and +1.6 nm respectively. Therefore, for every pump tuning of $+\delta$ nm, the primary idlers shift by "$+2\delta$" nm whereas the secondary idlers shift by "$-\delta$" nm. The

frequency spacing between the multicasting channels can be tuned to comply with the ITU grid by changing the frequency spacing between the incident waves within the broad conversion bandwidth of the SC-PPLN device. The results shown in Figure 6-4 illustrated the conversion range of 30 nm in C-band with the use of less than a third of the SC-PPLN bandwidth. Employing a broadband amplifier to tune the boosted pump/signal across the complete SC-PPLN bandwidth, this dual-idler multicasting can be extended to parts of L and S bands as well.

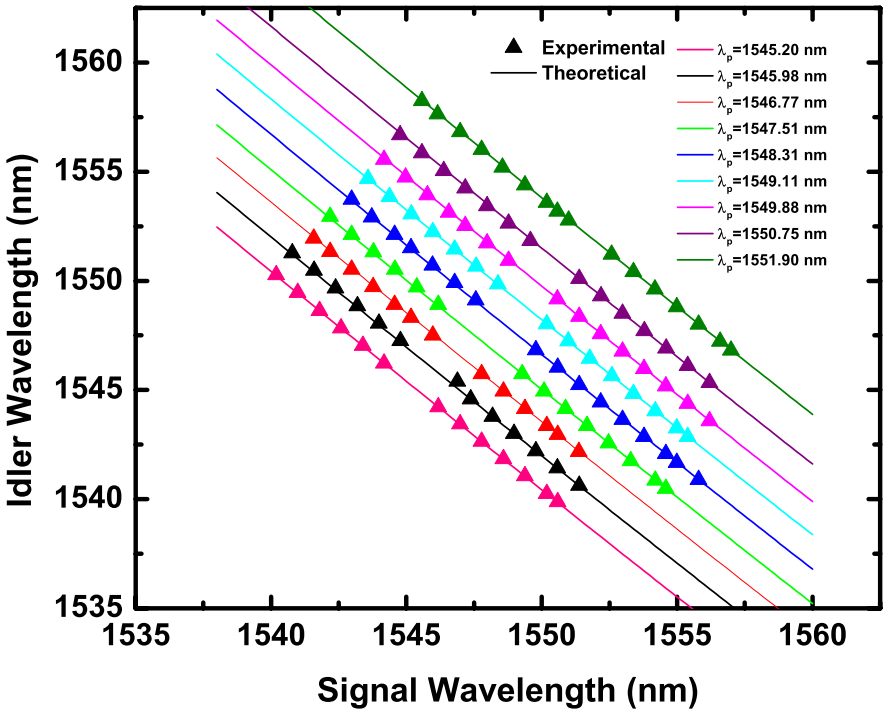

Figure 6-5: Experimental and theoretical curves for primary idler wavelength λ_i, vs. Signal wavelength λ_s as a function of pump wavelength λ_p.

In another set of experiments for dual wavelength broadcasting, the pump laser was kept fixed while tuning the signal wavelength across the C-band. The results have been summarized in Figure 6-5 which illustrates the relationship between the primary idler wavelength and signal wavelength as a function of pump wavelength. The triangle markers are experimentally observed values and the solid lines correspond to the theoretical relationship of the participating wavelengths as per Eq. 6.5. The experimental results shown here for 9 different pump wavelengths verify that for a signal wavelength tuning of "+δ" nm, the primary idlers shift by "-δ" nm. The pump wavelengths are located across 6.7 nm and for each pump wavelength the

signal is swept across for ~15 nm to obtain an equal spread of idler wavelengths. A similar relationship plot can be established for the secondary idler observing a detuning of "+2δ" nm for the tuning of signal wavelength by "+δ".

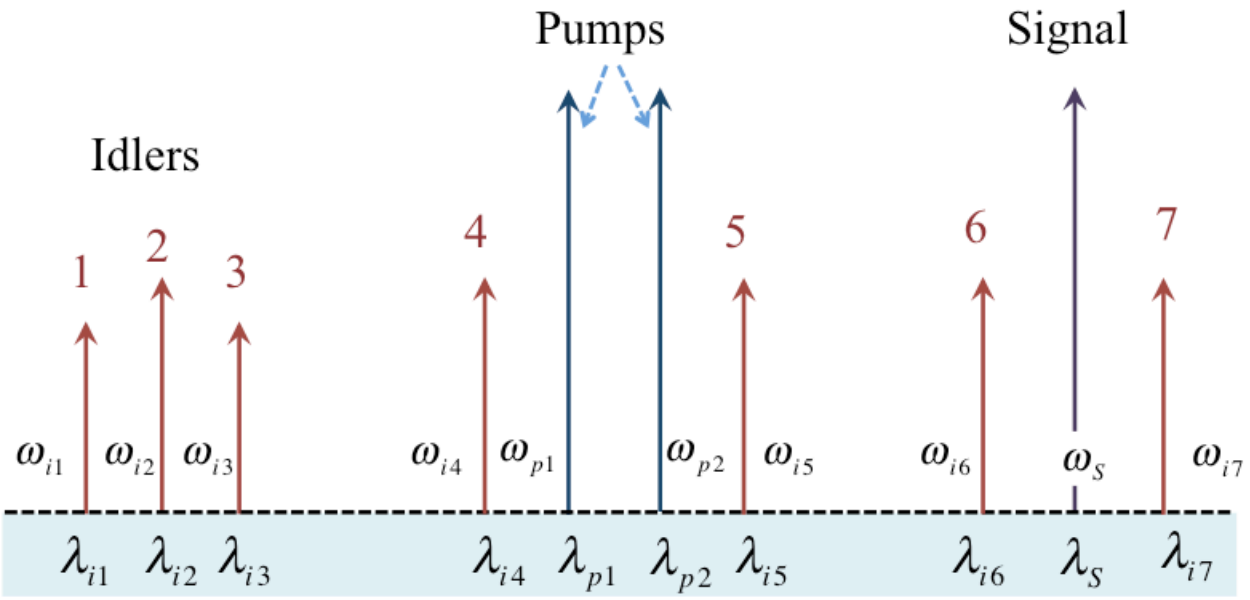

Figure 6-6: Schematic of seven idler broadcasting based on cascading of SHG/SFG-DFG process in the broadband PPLN device.

6.4 Seven-fold broadcasting of a signal using two pumps

In the previous section, one signal channel was converted to two idler channels by employing one pump in a cascaded SHG-DFG process, benefitting from the ultra-broad bandwidth of a SC-PPLN. Here, multiple idler generation in the SC-PPLN is demonstrated by inputting two pump lasers along with the signal. As shown in Figure 6-6, seven idlers are observed as a result of cascading of different second order nonlinear processes between the three interacting lasers. For given pump frequencies of ω_{p1} and ω_{p2} and signal at ω_s, the idlers are obtained at the following frequencies:

$$\omega_{i1} = 2\omega_{p2} - \omega_s,$$

$$\omega_{i2} = \omega_{p1} + \omega_{p2} - \omega_s,$$

$$\omega_{i3} = 2\omega_{p1} - \omega_s,$$

$$\omega_{i4} = 2\omega_{p1} - \omega_{p2},$$

$$\omega_{i5} = 2\omega_{p2} - \omega_{p1},$$

$$\omega_{i6} = \omega_{p1} + \omega_s - \omega_{p2},$$

$$\text{and, } \omega_{i7} = \omega_{p2} + \omega_s - \omega_{p1}. \qquad (6.7)$$

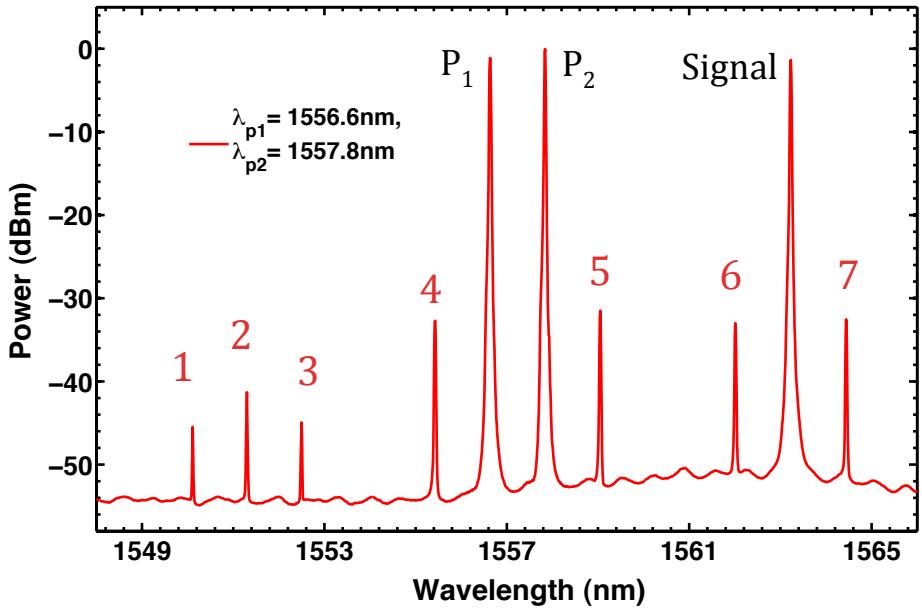

Figure 6-7: Normalized spectrum of broadcasting of a signal at 1563.2 nm to seven idlers by cascaded SHG/SFG-DFG processes in the SC-PPLN device.

In the second harmonic spectrum in the 775nm wavelength range, each of the two pumps have a second harmonic at $2\omega_{p1}$ and $2\omega_{p2}$; a sum frequency component for the two pumps at $\omega_{p1} + \omega_{p2}$; and also the sum frequency of each of the pumps with the signal wavelength at the frequencies $\omega_{p1} + \omega_s$ and $\omega_{p2} + \omega_s$. The first idler is the DF mixing of the signal with the SH of P2, second idler is DF mixing between signal and SF of the two pumps, third idler is the DF mixing of signal with SH of P1, third and fourth idlers are DF mixing of one pump with the SH of the other, while the last two idlers are DF mixing of one pump with the SF of other pump and

the signal wave. Two other idlers not included in this schematic since they lie out of the C-band, are the DF mixing of each of the pumps with the SH of signal. Thus in this configuration, a signal can be broadcast to a total of 9 idlers. Tunable filters can be employed to select the desired number of wavelength channels at the output.

The experimental demonstration of multiple idler broadcasting is illustrated in Figure 6-7 where a signal at 1563.2 nm is converted to seven idlers across 14 nm using two pumps at 1556.6 nm and 1557.8 nm in the broadband SC-PPLN device. The selection of pump wavelengths anywhere in the C-band is made possible by the broad ~28 nm SH/SF bandwidth of the step chirped PPLN.

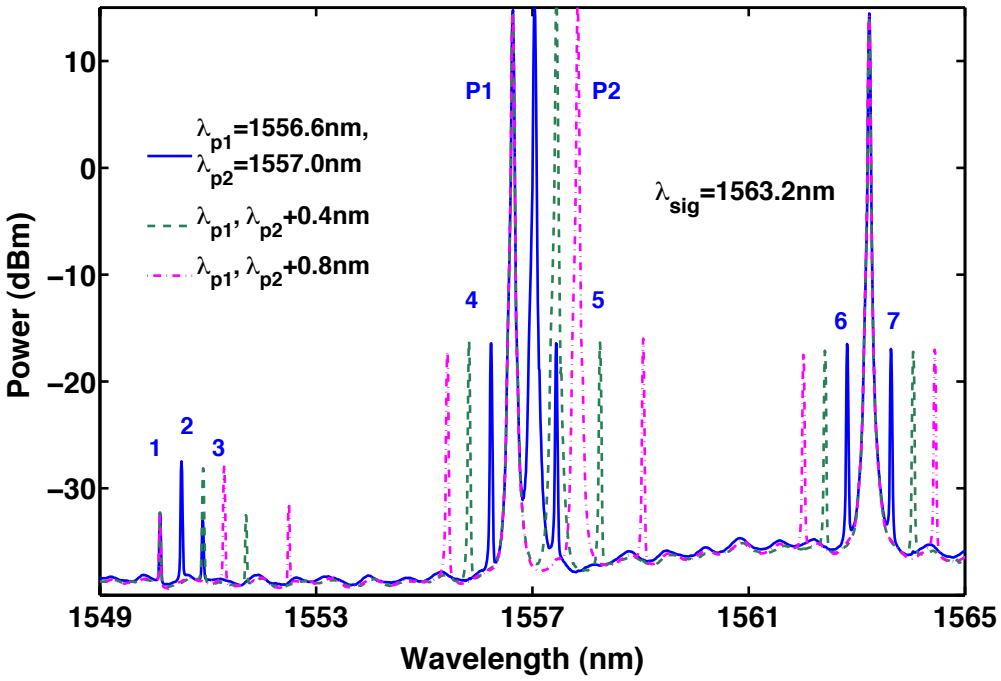

Figure 6-8: Experimentally observed spectra for tunable seven-idler broadcasting by detuning of just one pump for a fixed signal at 1563.2nm.

The position and mutual spacing of the multicast idlers can be varied by tuning the pumps within the broad SH/SF bandwidth, as in the case of the tunable dual-idler conversion. The tuning of idler spacing is experimentally demonstrated by shifting either or both of the pump wavelengths. For instance, in Figure 6-8 the blue solid trace corresponds to the pumps at 1556.6 nm and 1557.0 nm with a single WDM channel spacing in the 50-GHz International Telecommunication Union

(ITU) grid, and the corresponding idlers have been marked 1-7 (in blue) for a fixed signal at 1563.2 nm.

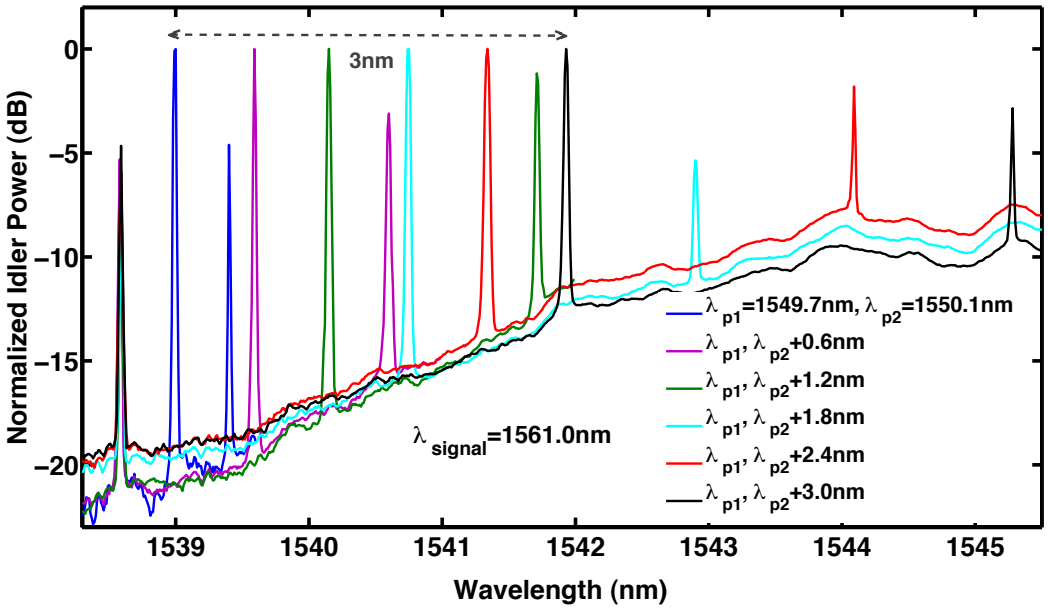

Figure 6-9: Tunable idler spacing in of a signal at 1561.0 nm with one pump fixed at 1549.7 nm and shifting the other pump wavelength at 1550.1 nm by +1.2 nm and +2.4 nm.

In this experiment, the pumps were set at power of 500 mW and 525 mW, whereas the signal power was 670 mW. For the spectrum shown by the green dashed trace, the pump spacing is increased to 0.8 nm i.e. 2 WDM channels with detuning of one of the pumps by 0.4 nm. Except the idler marked '1', the position of all other idlers in the WDM grid is changed. The magenta dashed plot shows the shift in idler positions obtained by detuning one of the pumps by 0.8 nm, so that the idlers occupy different channels over 13 nm in the C band. By detuning the pump by 6.0 nm, the idler positions in grid are varied to cover the entire C band. The extent of tunability of the multicast idlers by detuning one pump can be seen from Figure 6-9, where the experimental demonstration is provided for 3 different values of pump/idler spacing illustrating idlers 1-3 out of 7 idlers for clarity. The blue trace corresponds to pump/idler spacing of 0.4 nm when the pumps are located at 1549.7 nm and 1550.1 nm for signal at 1561.0 nm. In subsequent traces, the idler spacing has been changed over an additional 2.4 nm (6 WDM channels) by tuning the second pump by the same amount.

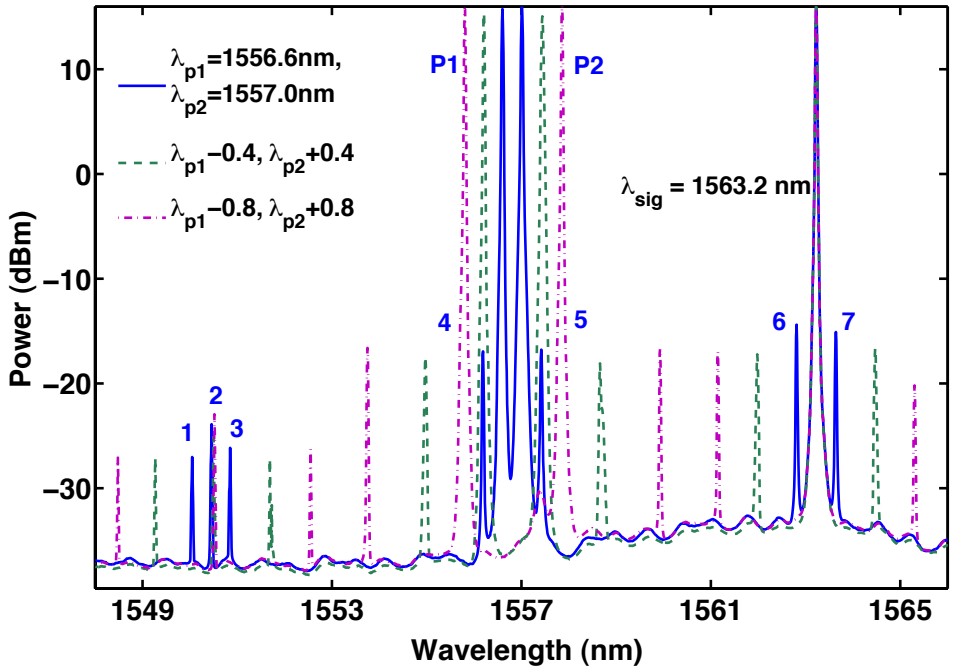

Figure 6-10: Experimentally observed spectra for tunable seven-idler broadcasting by detuning both pumps for a fixed signal at 1563.2nm.

In another experiment, the idler positions were tuned by detuning of both pump wavelengths. The initial pump and signal wavelengths in the spectrum depicted by the blue solid plot in Figure 6-9 are kept identical to the previous experiment. This time the pumps were set at powers 440 mW and 475 mW while the signal power was measured as 610 mW. The idler positions were symmetrically varied by increasing the spacing between the pumps (1.2 nm) using equal tuning of each pump wavelength by 0.4 nm, so that the idlers occupy different destination channels as seen in Figure 6-10 by green dashed plot. In this configuration, the position of the idler marked '2' did not change. In the magenta dash-dotted trace, the idlers further spread to cover 16 nm of the C- band by increasing the pump spacing to 2.0 nm i.e. 5 WDM channels, using equal detuning of 0.8 nm. This experiment is performed for a pump tuning of only 5.6 nm, to sweep idlers over the entire C band. The 7-idler multicasting is also extendable across L and S bands using a broadband amplifier making complete use of the available bandwidth.

It should be noted from Eq. (6.7) that, while idlers 1-3 and 6-7 vary with the signal, the position of idlers marked 4 and 5 depends entirely on the pump wavelengths. However, as all three input lasers lie within the broad SF-SH bandwidth of the SC-PPLN, their positions in the WDM grid are interchangeable. The same seven idlers can be obtained by swapping the position of one of the pumps P_1 (P_2) with the signal such that the idlers 4 and 5 now tune with the signal and P_2 (P_1) but does not depend on P_1 (P_2). This additional degree of freedom for pump/signal location is also useful to obtain selective amount of spacing for each of the seven idler wavelengths. For example, in the configuration of Figure 6-8 ($\lambda_{p1} < \lambda_{p2} < \lambda_s$), by moving the signal by '$+\delta$' nm the idlers 1-3 shift by '$-\delta$', idlers 4-5 do not shift with the signal, and the idlers 6-7 shift by '$+\delta$'. In an alternative scheme of ($\lambda_s < \lambda_{p2} < \lambda_{p1}$) achieved by swapping the position of the pump (P_1) and signal, the idler marked 1 experience no shift with signal; idlers 2, 5-7 shift by '$+\delta$' , while the idlers 3-4 move by '$+2\delta$'. Thus, by selectively varying the location of idlers in the WDM grid, a broadband SC-PPLN improves the functionality of the optical multicasting devices.

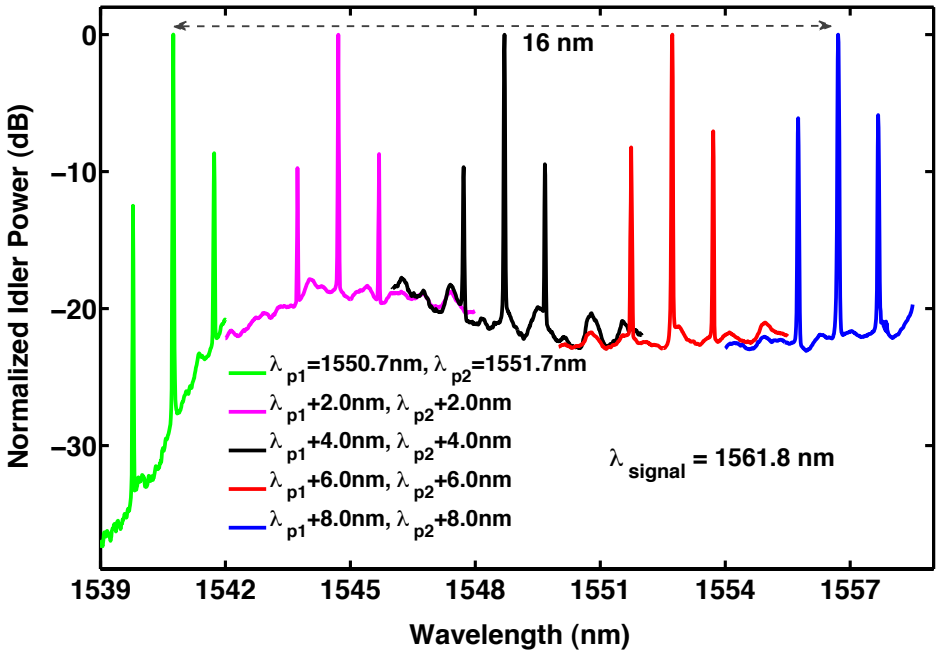

Figure 6-11: Spectral demonstration of tunable WDM position in triple-idler broadcasting of a signal at 1561.7 nm by shifting the two-pumps at 1550.7 nm and 1551.7 nm by +2.0 nm, +4.0 nm, +6.0 nm and +8.0 nm.

In the results shown in Figure 6-10, both pumps were simultaneously tuned in opposite direction to generate different spacing of the idlers. However, the liberty of choice of tuning two pump positions together in same direction in the broad conversion bandwidth of the step-chirped PPLN results in the simultaneous shift of broadcast idlers across the C-band, as illustrated in Figure 6-11.

Table 6.1: Relationship of tunability of the idlers with the pump detuning.

	One pump detuning	**Both pumps opposite detuning**	**Both pumps identical detuning**
Detuning of Pump 1 λ_{p1}	0	$-\delta\ nm$	$+\delta\ nm$
Detuning of Pump 2 λ_{p2}	$+\delta\ nm$	$+\delta\ nm$	$+\delta\ nm$
Detuning of Idler 1 λ_{i1}	0	$-2\delta\ nm$	$+2\delta\ nm$
Detuning of Idler 2 λ_{i2}	$+\delta\ nm$	0	$+2\delta\ nm$
Detuning of Idler 3 λ_{i3}	$+2\delta\ nm$	$+2\delta\ nm$	$+2\delta\ nm$
Detuning of Idler 4 λ_{i4}	$-\delta\ nm$	$-2\delta\ nm$	$+\delta\ nm$
Detuning of Idler 5 λ_{i5}	$+2\delta\ nm$	$+2\delta\ nm$	$+\delta\ nm$
Detuning of Idler 6 λ_{i6}	$-\delta\ nm$	$-2\delta\ nm$	0
Detuning of Idler 7 λ_{i7}	$+\delta\ nm$	$+2\delta\ nm$	0

The three idlers represent idlers 1-3 in the schematic of Figure 6-6, wherein the two pumps lying in the C-band launched into PPLN produce one SF wave and two SH waves, the signal then undergoes DF mixing with each of the three SH/SF waves and result in these three idlers within the same band. Figure 6-11 shows the overlap of 5 experimentally observed idler spectra corresponding to different pumps, e.g. the green trace shows the idlers at 1539.7 nm, 1540.7 nm

and 1541.7 nm for the signal at 1561.7 nm and the pumps at 1550.7 nm and 1551.7 nm. By tuning the pumps over 8 nm the idlers get shifted by twice the amount i.e. 16 nm to 1555.7 nm, 1556.7 nm and 1557.7 nm i.e. across 40 WDM channels considering 50 GHz spacing grid, as illustrated by the blue trace. The idlers 4-5 not shown in this plot, also shift in the direction of the pump tuning. With the detuning of both pumps by '$+\delta$' nm, the idlers 4-5 also shift by '$+\delta$' nm. However, idlers 6-7 which are the result of DF mixing of one pump with the SF of the signal and other pump, do not shift in this scheme as is apparent from the relations given in Eq. 6.7. The results of detuning obtained for each idler in the different schemes demonstrated in Figures 6-8 to 6-11 are summarized in Table 6-1.

Table 6.2: Multiple idler generation in a SC-PPLN device based on cascaded second order interaction using three pumps and one signal.

1 Signal	3 Pumps	9 SH/SF		21 Idlers
ω_S	ω_{p1}	$2\omega_{p1}$		$2\omega_{p1}-\omega_s$
				$2\omega_{p1}-\omega_{p2}$
				$2\omega_{p1}-\omega_{p3}$
		$2\omega_{p2}$		$2\omega_{p2}-\omega_s$
				$2\omega_{p2}-\omega_{p1}$
				$2\omega_{p2}-\omega_{p3}$
		$2\omega_{p3}$		$2\omega_{p3}-\omega_s$
				$2\omega_{p3}-\omega_{p1}$
				$2\omega_{p3}-\omega_{p2}$
	ω_{p2}	$\omega_{p1}+\omega_{p2}$		$\omega_{p1}+\omega_{p2}-\omega_s$
				$\omega_{p1}+\omega_{p2}-\omega_{p3}$
		$\omega_{p1}+\omega_{p3}$		$\omega_{p1}+\omega_{p3}-\omega_s$
				$\omega_{p1}+\omega_{p3}-\omega_{p2}$
	ω_{p3}	$\omega_{p1}+\omega_s$		$\omega_{p1}+\omega_s-\omega_{p2}$
				$\omega_{p1}+\omega_s-\omega_{p3}$
		$\omega_{p2}+\omega_{p3}$		$\omega_{p1}+\omega_{p3}-\omega_s$
				$\omega_{p1}+\omega_{p3}-\omega_2$
		$\omega_{p2}+\omega_s$		$\omega_{p2}+\omega_s-\omega_{p1}$
				$\omega_{p2}+\omega_s-\omega_{p3}$
		$\omega_{p3}+\omega_s$		$\omega_{p3}+\omega_s-\omega_{p1}$
				$\omega_{p3}+\omega_s-\omega_{p2}$

Similar to obtaining the 7 idlers using two pumps, the wavelength conversion technique is also extendable to multicasting a signal to a maximum of 21 idlers by launching 3 pump lasers within the wide SC-PPLN bandwidth as demonstrated in Table 6-2. The three pumps and one signal result in 9 peaks in SH/SF spectrum in the 775 nm wavelength regime. The interaction of these 9 peaks via DF mixing with the 4 FH waves, gives 21 distinct idlers in the 1.55 μm band. This signifies that the broadband SC-PPLN device will improve the flexibility of all-optical broadcasting to multiple channels in a cascaded SH'SF-DF process using multiple tunable pumps.

6.5 Conclusion

In this chapter, an engineered step-chirped PPLN device was demonstrated for the first time, designed and fabricated for obtaining broad ~30nm bandwidth in the 1.55 μm wavelength band. The 20 mm long SC-PPLN was divided into ten equal sections having periods varying from 18.2 μm to 19.1 μm in steps of 0.1 μm each. The ease of fabrication of a step-chirped scheme with large step changes is a great advantage over a linearly chirped grating without sacrificing the bandwidth or efficiency. The experimentally observed SH bandwidth of ~28 nm is in excellent agreement with theory having a similarly rippley response as that of the theoretically simulated bandwidth of 30 nm. The ripples in SH bandwidth translate in a similar manner to the cascaded SHG-DFG conversion and therefore not desirable for WDM networking applications. To overcome the power fluctuations for the output idlers, slightly varying the power of input pumps can flatten the response. However, an ideal solution in terms of an apodization technique has been proposed to flatten the conversion bandwidth of step-chirped PPLN devices. The efficiency of the SC-PPLN device is lowered considerably due to the use of CW pumps and a bulk configuration. Waveguides of small cross section can be fabricated in such PPLN devices for increasing the idler efficiency by >20 dB.

Wavelength conversion is demonstrated by DF mixing of the signal and the SH of pump wave by inputting a signal along with the pump lying in the broad SH bandwidth of the SC-PPLN device. Moreover, since the signal also lies in the SH bandwidth of the SC-PPLN device, another idler is generated by DF mixing of the pump and the SH of the signal wave. By tuning the pump laser anywhere within the wide SH bandwidth, tunability of wavelength conversion of the signal into

primary and secondary idlers located in the entire C band is demonstrated. Tuning the pump laser over 8 nm is sufficient to obtain idlers spreading over 28 nm in the C band.

Further, employing two pumps in the wide bandwidth of the SC-PPLN, one signal was successfully converted to seven idlers using cascaded second order interactions of SHG/DFG and SFG/DFG. The free choice of pump position tunes the mutual idler spacing as well as their locations in the C-band. Results have been shown for three different configurations of pump tuning with variable destination channel spacings and locations.

Summarizing, agile multicasting of a single-channel has been proposed and demonstrated based on cascaded SHG-SFG and DFG in a 20-mm-long step-chirped PPLN with >28-nm SH-SF bandwidth lying in the C-band. By using an SC-PPLN we have also overcome the limited speed of tunable multicasting arising from using a temperature-tuning-based PPLN. Agile multicasting achieved by this temperature-independent scheme in an SC-PPLN, covering whole C, L and S band using a broadband amplifier, is agnostic to signal modulation formats and will play a significant role in enhancing the dynamic signal path routing in WDM networks, and help in the construction of flexible all-optical networks.

CHAPTER 7
CONCLUSIONS

7.1 Thesis summary

This thesis proposed and demonstrated new devices for broadband and tunable wavelength conversion for wide bandwidth communication applications, such as video broadcasting and triple play, based on quasi phase matched (QPM) nonlinear interaction in (a)periodically domain inverted nonlinear crystals. All-optical wavelength conversion QPM devices such as periodically poled lithium niobate (PPLN) are promising for optical networks in comparison with the current high speed electronics because of their several advantages, such as low noise, high speed, compact size, no dependence on bit rate and signal modulation format etc.. While QPM devices have been extensively investigated to achieve higher efficiency of second harmonic generation (SHG), improvement to increase their SH conversion bandwidth was necessary for mainly two reasons: firstly, to achieve the flexibility of wavelength conversion of a signal to any channel in the communication band; and secondly, to broadcast a signal to several channels simultaneously by employing multiple pump lasers within its broad bandwidth. This thesis addressed these requirements by demonstrating wavelength conversion based on cascaded SHG and difference frequency generation (cSHG/DFG) and cascaded sum frequency generation (cSFG)/DFG mixing in domain inverted gratings in LN engineered for a broad bandwidth over the optical communication (C) band.

The first step in implementation of the QPM devices was the design of periodic or chirped (varying period) grating for the desired conversion wavelength and bandwidth. The use of QPM technology in nonlinear crystals allowed longer and hence more efficient devices. There is, however, a trade-off in uniform QPM gratings between higher efficiency obtained by increasing the length of the device and larger bandwidth obtained by decreasing it's length. Although chirped and step-chirped (SC) gratings have already been proposed to broaden the QPM bandwidth by changing the period of the inverted domains as a function of crystal length, practical realization of a first broadband SC-PPLN for communication band was presented in this dissertation.

In chapter 3, domain inversion to produce PPLN gratings was done by the popular liquid

electrode poling method which has evolved at a tremendous rate since its introduction in 1993 [128]. This process involved photolithographic patterning of the z-cut 0.5 mm thick LN wafer with a positive photoresist S1813. The periodic grating pattern was transferred to the substrate by UV exposure through a mask. A high electric field of ~22kV/mm in the form of 0.5 ms step pulses was applied across the imprinted wafer to invert the domains. In-situ monitoring of poling was done by a crossed-polarizer setup and inverted domains were visualized by etching of –z face in HF acid. After optimization of the poling process, a mask of 1:4 duty-ratio was used to achieve a 1:1 final mark-space ratio in uniform gratings. The challenge in fabricating very small step-changes in the period for continuously chirped gratings was overcome by designing step-chirped grating profile without sacrificing in efficiency or bandwidth [88]. Three different grating structures were fabricated with a uniform, phase-shifted and a step-chirped profile and implemented for wavelength broadcasting, for the first time.

We first used a uniform PPLN waveguide to demonstrate wavelength conversion in C-band based on cSFG/DFG, as described in chapter 4. In a cSFG/DFG process two widely separated pump wavelengths were employed, which gave ripples in the conversion bandwidth due to large phase mismatch in the center of bandwidth curve associated with the DFG process. By slightly detuning the pump wavelengths from perfect phase-matching, we decreased the phase mismatch in the center of the bandwidth curve. This gave a flattened bandwidth for cascaded conversion, for the first time, and the bandwidth (peak-to-peak) ripples were reduced from 2 dB to 0.5 dB.

Demonstration of all-optical broadcasting of one signal to three output channels based on simultaneous SHG/DFG and SFG/DFG was achieved in uniform PPLN by inputting two closely spaced pumps in the SH bandwidth of the PPLN. The mutual separation of triple-output channels was decided by the pump wavelength separation. Owing to the narrow second harmonic bandwidth of PPLN, the pump spacing could not be tuned more than 0.5 nm. Therefore, the spacing between the output channels and hence their location in WDM grid could not be varied without drastically losing the output idler efficiency.

For practical WDM networks, it is essential to provide variable location of output channels. In chapter 5 of this thesis, a solution for tunable broadcasting was demonstrated by using a PPLN with a central aperiodic domain. The phase shift resulted in a dual-peak SH response having twice bandwidth (~2.1 nm) than a uniform PPLN of same length. There is a corresponding 3-dB

decrease in the peak SH efficiency. The choice of pump wavelengths coinciding with the dual-peaks of aPPLN led to three SH/SF peaks in the SH spectrum. Further, tuning one pump wavelength to the minima between the dual-peaks suppressed one out of the three SH/SF peaks. Cascading this variable SH/SF output of pumps with DFG mixing of the signal resulted in variable number of output channels in C-band. Triple channel broadcasting was again demonstrated, however this time the channels could be spread across ~7nm in C-band, equivalent to ~18 WDM channels of 50GHz separation. In addition, by varying the temperature of the crystal by 10 °C, the SH/SF bandwidth of the aPPLN was then tuned over 4.4 nm in the C-band. By combining the pump detuning with temperature tuning, the three idlers can be positioned in C-band with desired spacing and variable position in WDM grid.

The slow speed of temperature tuning is a deterrent for ultra-fast WDM applications, therefore a third PPLN device with step-chirped (SC) grating structure was exclusively designed and implemented in a 20mm long SC-PPLN with 10 sections of periods varying from 18.2 μm to 19.1 μm with a chirp step of 100 nm. The SC-PPLN had a broad temperature independent ~30 nm bandwidth in C-band, where the pump wavelength could be freely tuned to obtain wavelength conversion with tunable spacing and desired location in the WDM grid. Flexible broadcasting of a signal to seven tunable output idlers was realized owing to the DF mixing of signal with pump SHs and also the SH of signal with the pump frequencies. The inherent broad bandwidth allowed temperature independent operation of the device for ultrafast all-optical network applications.

Therefore, the essential contributions of this thesis were to design and implement $LiNbO_3$ QPM devices for tunable broadband wavelength conversion and flexible broadcasting in high capacity future all-optical WDM networks. This dissertation has realized multiple-idler generation in periodic, aperiodic and step-chirped PPLN. The broadband response of a step-chirped PPLN offered great advantage of enhancing the tunability of all-optical converters to cover the entire communication C-band.

7.2 Directions for future work

In future networks, all-optical broadband wavelength converters will play a crucial role to avoid wavelength blocking and improve the use of signal wavelengths. We have considered various bandwidth-broadening schemes of bulk PPLN devices in this work, however, further work is needed to incorporate the objectives for efficiency enhancement of these schemes. Combining

research that has already been proposed for improving the conversion efficiency by using double pass configuration or smaller cross-section APE waveguides [80] to further scale the efficiency will greatly enhance the capabilities of flexible conversion and efficient broadcast devices. Moreover, the SC-PPLN device described in chapter 6, has ripples in the frequency response owing to the interference among constituent phase matching spectra originating from different positions in the gratings. A similar device with added apodization feature, which includes changing duty ratio of the chirped grating, can be implemented in future to remove the ripples and obtain a flat response.

There is also a great need to develop a complete theoretical model for understanding the multi-channel broadcast based on competing nonlinear processes of cSHG/DFG and cSFG/DFG in the QPM all-optical converters. A mechanism for filtering out selected idlers from the generated idlers is also an important work that should be considered.

REFERENCES

1. A. H. Gnauck, G. Charlet, P. Tran, P. J. Winzer, C. R. Doerr, J. C. Centanni, E. C. Burrows, T. Kawanishi, T. Sakamoto, and K. Higuma, "25.6-Tb/s WDM Transmission of Polarization-Multiplexed RZ-DQPSK Signals," Lightwave Technology, Journal of **26**, 79-84 (2008).

2. D. Gallant, "Optical network foundation for triple play services roll-out," in *Optical Fiber Communication Conference, 2006 and the 2006 National Fiber Optic Engineers Conference. OFC 2006*, 2006), 6 pp.

3. T. H. Maiman, "Optical and Microwave-Optical Experiments in Ruby," Physical Review Letters **4**, 564-566 (1960).

4. P. A. Franken, A. E. Hill, C. W. Peters, and G. Weinreich, "Generation of optical harmonics," Physical Review Letters **7**, 118-119 (1961).

5. J. A. Armstrong, N. Bloembergen, J. Ducuing, and P. S. Pershan, "Interactions between light waves in a non-linear dielectric," Physical Review **127**, 1918-1939 (1962).

6. J. A. Giordmaine, "Mixing of Light Beams in Crystals," Physical Review Letters **8**, 19 (1962).

7. P. D. Maker, R. W. Terhune, M. Nisenoff, and C. M. Savage, "Effects of Dispersion and Focusing on the Production of Optical Harmonics," Physical Review Letters **8**, 21 (1962).

8. D. A. Kleinman, "Theory of second harmonic generation of light," Physical Review **128**, 1761-1775 (1962).

9. G. D. Boyd, A. Ashkin, J. M. Dziedzic, and D. A. Kleinman, "Second-harmonic generation of light with double refraction," Physical Review **l37**, A1305-A1320 (1965).

10. D. A. Kleinman, A. Ashkin, and G. D. Boyd, "Second harmonic generation of light by focused laser beams," IEEE Journal of Quantum Electronics **QE-2**, 425-429 (1966).

11. G. D. Boyd and D. A. Kleinman, "Parametric integration of focused Gaussian light beams," in *1968 international quantum electronics conference, 14-17 May 1968*, IEEE J. Quantum Electron. (USA) 1968), 353.

12. D. E. Thompson, J. D. McMullen, and D. B. Anderson, "Second harmonic generation in GaAs stack of plates using high power CO_2 laser radiation," Applied Physics Letters **29**, 113-115 (1976).

13. R. C. Miller, "Optical second harmonic generation in piezoelectric crystals," Applied Physics Letters **5**, 17-19 (1964).

14. S. Matsumoto, E. J. Lim, H. M. Hertz, and M. M. Fejer, "Quasiphase-matched second harmonic generation of blue light in electrically periodically-poled lithium tantalate waveguides," Electronics Letters **27**, 2040-2042 (1991).

15. M. Yamada, N. Nada, M. Saitoh, and K. Watanabe, "First-order quasi-phasematched $LiNbO_3$ waveguides periodically poled by applying an external electric field for efficient SHG," Molecular Crystals and Liquid Crystals Science and Technology Section B: Nonlinear Optics **7**, 333-337 (1994).

16. W. K. Burns, W. McElhanon, and L. Goldberg, "Second harmonic generation in field poled, quasi-phase-matched, bulk $LiNbO_3$," Photonics Technology Letters, IEEE **6**, 252-254 (1994).

17. J. Webjorn, V. Pruneri, P. S. J. Russell, and D. C. Hanna, "55% conversion efficiency to green in bulk quasi-phase-matching lithium niobate," Electronics Letters **31**, 669-671 (1995).

18. L. E. Myers, R. C. Eckardt, M. M. Fejer, and R. L. Byer, "Quasi-phasematched optical parametric oscillators using bulk periodically poled $LiNbO_3$," in *Solid State Lasers and Nonlinear Crystals, Febrary 5, 1995 - Febrary 7, 1995*, Proceedings of SPIE - The International Society for Optical Engineering (Society of Photo-Optical Instrumentation Engineers, 1995), 154-162.

19. G. D. Miller, R. G. Batchko, W. M. Tulloch, D. R. Weise, M. M. Fejer, and R. L. Byer, "42%-efficient single-pass cw second-harmonic generation in periodically poled lithium niobate," Opt. Lett. **22**, 1834-1836 (1997).

20. F. Jermann, M. Simon, and E. Kratzig, "Photorefractive properties of congruent and stoichiometric lithium niobate at high light intensities," Journal of the Optical Society of America B (Optical Physics) **12**, 2066-2070 (1995).

21. W. M. Young, R. S. Feigelson, D. H. Jundt, and M. M. Fejer, "Influence of composition of MgO-doped lithium niobate on phase-matching temperature for frequency doubling in the visible," Journal of Applied Physics **69**, 7372-7374 (1991).

22. Y. Furukawa, K. Kitamura, S. Takekawa, A. Miyamoto, M. Terao, and N. Suda, "Photorefraction in $LiNbO_3$ as a function of [Li]/[Nb] and MgO concentrations," Applied Physics Letters **77**, 2494-2496 (2000).

23. M. L. Bortz and M. M. Fejer, "Annealed proton-exchanged $LiNbO_3$ waveguides," Opt. Lett. **16**, 1844-1846 (1991).

24. Y. Nishida, H. Miyazawa, M. Asobe, O. Tadanaga, and H. Suzuki, "0-dB wavelength conversion using direct-bonded QPM-Zn : $LiNbO_3$ ridge waveguide," Photonics Technology Letters, IEEE **17**, 1049-1051 (2005).

25. T. Suhara and H. Nishihara, "Theoretical analysis of waveguide second-harmonic generation phase matched with uniform and chirped gratings," IEEE Journal of Quantum Electronics **26**, 1265-1276 (1990).

26. G. Imeshev, A. Galvanauskas, D. Harter, M. A. Arbore, M. Proctor, and M. M. Fejer, "Engineerable femtosecond pulse shaping by second-harmonic generation with Fourier synthetic quasi-phase-matching gratings," Opt. Lett. **23**, 864-866 (1998).

27. A. M. Schober, M. Charbonneau-Lefort, and M. M. Fejer, "Broadband quasi-phase-matched second-harmonic generation of ultrashort optical pulses with spectral angular dispersion," J. Opt. Soc. Am. B **22**, 1699-1713 (2005).

28. A. M. Schober, G. Imeshev, and M. M. Fejer, "Tunable-chirp pulse compression in quasi-phase-matched second-harmonic generation," Opt. Lett. **27**, 1129-1131 (2002).

29. M. A. Arbore, A. Galvanauskas, D. Harter, M. H. Chou, and M. M. Fejer, "Engineerable compression of ultrashort pulses by use of second-harmonic generation in chirped-period-poled lithium niobate," Optics Letters **22**, 1341-1343 (1997).

30. A. Tehranchi and R. Kashyap, "Design of novel unapodized and apodized step-chirped quasi-phase matched gratings for broadband frequency converters based on second-harmonic generation," Journal of Lightwave Technology **26**, 343-349 (2008).

31. A. Tehranchi and R. Kashyap, “Response flattening of efficient broadband wavelength converters based on cascaded sum and difference frequency generation in periodically poled lithium niobate waveguides,” IEEE Journal of Quantum Electronics **45**, 1114-1120 (2009).

32. G. W. Ross, M. Pollnau, P. G. R. Smith, W. A. Clarkson, P. E. Britton, and D. C. Hanna, “Generation of high-power blue light in periodically poled $LiNbO_3$,” Optics Letters **23**, 171-173 (1998).

33. W. Sohler, B. Hampel, R. Regener, R. Ricken, H. Suche, and R. Volk, “Integrated optical parametric devices,” Lightwave Technology, Journal of **4**, 772-777 (1986).

34. M. L. Bortz, M. A. Arbore, and M. M. Fejer, “Quasi-phase-matched optical parametric amplification and oscillation in periodically poled LiNbO3 waveguides,” Opt. Lett. **20**, 49-51 (1995).

35. L. E. Myers and W. R. Bosenberg, “Periodically poled lithium niobate and quasi-phase-matched optical parametric oscillators,” Quantum Electronics, IEEE Journal of **33**, 1663-1672 (1997).

36. L. E. Myers, R. C. Eckardt, M. M. Fejer, R. L. Byer, and W. R. Bosenberg, “Multigrating quasi-phase-matched optical parametric oscillator in periodically poled LiNbO3,” Opt. Lett. **21**, 591-593 (1996).

37. D. D. Marcenac, A. E. Kelly, D. Nesset, and D. A. O. Davies, “Bandwidth enhancement of wavelength conversion via cross-gain modulation by semiconductor optical amplifier cascade,” Electronics Letters **31**, 1442-1443 (1995).

38. K. Obermann, S. Kindt, D. Breuer, and K. Petermann, “Performance analysis of wavelength converters based on cross-gain modulation in semiconductor-optical amplifiers,” Lightwave Technology, Journal of **16**, 78-85 (1998).

39. C. Q. Xu, H. Okayama, and M. Kawahara, “1.5 micron band efficient broadband wavelength conversion by difference frequency generation in a periodically domain inverted $LiNbO_3$ channel waveguide,” Applied Physics Letters **63**, 3559-3561 (1993).

40. C.-Q. Xu, H. Okayama, and T. Kamijoh, "Broadband Multichannel Wavelength Conversions for Optical Communication Systems Using Quasiphase Matched Difference Frequency Generation," Japanese Journal of Applied Physics **34**, 3 (1995).

41. M. H. Chou, J. Hauden, M. A. Arbore, and M. M. Fejer, "1.5-μm-band wavelength conversion based on difference-frequency generation in $LiNbO_3$ waveguides with integrated coupling structures," Opt. Lett. **23**, 1004-1006 (1998).

42. G. P. Banfi, P. K. Datta, V. Degiorgio, and D. Fortusini, "Wavelength shifting and amplification of optical pulses through cascaded second-order processes in periodically poled lithium niobate," Applied Physics Letters **73**, 136-138 (1998).

43. G. I. Stegeman, D. J. Hagan, and L. Torner, "χ(2) cascading phenomena and their applications to all-optical signal processing, mode-locking, pulse compression and solitons," Opt Quant Electron **28**, 1691-1740 (1996).

44. K. Gallo and G. Assanto, "Analysis of lithium niobate all-optical wavelength shifters for the third spectral window," J. Opt. Soc. Am. B **16**, 741-753 (1999).

45. C.-Q. Xu and B. Chen, "Cascaded wavelength conversions based on sum-frequency generation and difference-frequency generation," Opt. Lett. **29**, 292-294 (2004).

46. A. Tehranchi and R. Kashyap, "Improved cascaded sum and difference frequency generation-based wavelength converters in low-loss quasi-phase-matched lithium niobate waveguides," Applied Optics **48**, G143-G147 (2009).

47. C. Langrock, S. Kumar, J. E. McGeehan, A. E. Willner, and M. M. Fejer, "All-Optical Signal Processing Using χ(2) Nonlinearities in Guided-Wave Devices," J. Lightwave Technol. **24**, 2579 (2006).

48. A. Bogoni, X. Wu, J. Wang, and A. E. Willner, "Ultra-Fast All Optical Signal Processing and Switching Based on PPLN Waveguides," in OSA Technical Digest (CD) (Optical Society of America, 2010), PWA1.

49. H. Furukawa, A. Nirmalathas, N. Wada, S. Shinada, H. Tsuboya, and T. Miyazaki, "Tunable All-Optical Wavelength Conversion of 160-Gb/s RZ Optical Signals by Cascaded SFG-DFG Generation in PPLN Waveguide," Photonics Technology Letters, IEEE **19**, 384-386 (2007).

50. A. Bogoni, X. Wu, I. Fazal, and A. E. Willner, "Photonic processing of 320 Gbits/s based on sum-/difference-frequency generation and pump depletion in a single PPLN waveguide," Opt. Lett. **34**, 1825-1827 (2009).

51. M. H. Chou, K. R. Parameswaran, M. M. Fejer, and I. Brener, "Multiple-channel wavelength conversion by use of engineered quasi-phase-matching structures in $LiNbO_3$ waveguides," Opt. Lett. **24**, 1157-1159 (1999).

52. M. Asobe, O. Tadanaga, H. Miyazawa, Y. Nishida, and H. Suzuki, "Multiple quasi-phase-matched $LiNbO_3$ wavelength converter with a continuously phase-modulated domain structure," Opt. Lett. **28**, 558-560 (2003).

53. N. E. Yu, J. H. Ro, M. Cha, S. Kurimura, and T. Taira, "Broadband quasi-phase-matched second-harmonic generation in MgO-doped periodically poled $LiNbO_3$ at the communications band," Opt. Lett. **27**, 1046-1048 (2002).

54. F. Lu, Y. Chen, J. Zhang, W. Lu, X. Chen, and Y. Xia, "Broadcast wavelength conversion based on cascaded $\chi^{(2)}$ nonlinearity in MgO-doped periodically poled $LiNbO_3$," Electronics Letters **43**, 1446-1447 (2007).

55. J. Zhang, Y. Chen, F. Lu, and X. Chen, "Flexible wavelength conversion via cascaded second order nonlinearity using broadband SHG in MgO-doped PPLN," Opt. Express **16**, 6957-6962 (2008).

56. M. Gong, Y. Chen, F. Lu, and X. Chen, "All optical wavelength broadcast based on simultaneous Type I QPM broadband SFG and SHG in MgO:PPLN," Opt. Lett. **35**, 2672-2674 (2010).

57. M. Scaffardi, F. Fresi, A. Bogoni, and L. Poti, "Implementation of a tunable 160 Gb/s wavelength multi-converter based on supercontinuum in a highly nonlinear fibre," in *Optical Communications, 2006. ECOC 2006. European Conference on*, 2006), 1-2.

58. G. Qin, X. Yan, C. Kito, M. Liao, T. Suzuki, A. Mori, and Y. Ohishi, "Highly nonlinear tellurite microstructured fibers for broadband wavelength conversion and flattened supercontinuum generation," Journal of Applied Physics **107**, 043108 (2010).

59. F. D. Mahad, A. S. M. Supa'at, S. M. Idrus, and D. Forsyth, "Comparative performance testing of SOA wavelength conversion techniques for future all-optical systems," Optik - International Journal for Light and Electron Optics **124**, 1254-1259 (2013).

60. J. Wang, H. Fu, D. Geng, and A. E. Willner, "Single-PPLN-assisted wavelength-/time-selective switching/dropping/swapping for 100-GHz-spaced WDM signals," Opt. Express **21**, 3756-3774 (2013).

61. A. Malacarne, G. Meloni, G. Berrettini, N. Sambo, L. PotÏ, and A. Bogoni, "Optical Multicasting of 16QAM Signals in Periodically-Poled Lithium Niobate Waveguide," J. Lightwave Technol. **31**, 1797-1803 (2013).

62. A. Bogoni, X. Wu, S. R. Nuccio, and A. E. Willner, "640 Gb/s All-Optical Regenerator Based on a Periodically Poled Lithium Niobate Waveguide," J. Lightwave Technol. **30**, 1829-1834 (2012).

63. B.-J. Kim, C.-S. Kim, D.-J. Kim, H.-H. Lim, S.-K. Park, M.-S. Cha, and K.-J. Kim, "Fabrication of Thick Periodically-poled Lithium Niobate Crystals by Standard Electric Field Poling and Direct Bonding," J. Opt. Soc. Korea **14**, 420-423 (2010).

64. Z. Jin-Hua, L. Xiu-Hong, H. Qing, L. Peng, and W. Xue-Lin, "Lithium Niobate Ridge Waveguides Fabricated by Ion Implantation Followed by Ion Beam Etching," Lightwave Technology, Journal of **28**, 1913-1916 (2010).

65. A. Bogoni, X. Wu, Z. Bakhtiari, S. Nuccio, R. W. Hellwarth, and A. E. Willner, "640 Gb/s All-Optical Add/Drop Multiplexing Based on Pump Depletion in a PPLN Waveguide," in OSA Technical Digest (CD) (Optical Society of America, 2010), PTuB6.

66. J. Wang, S. Nuccio, X. Wu, O. Yilmaz, L. Zhang, I. Fazal, J.-Y. Yang, Y. Yue, and A. Willner, "40-Gbit/s Optical Data Exchange between WDM Channels Using Second-Order Nonlinearities in PPLN Waveguides," in OSA Technical Digest (CD) (Optical Society of America, 2009), PDPA1.

67. T. Umeki, M. Asobe, T. Yanagawa, O. Tadanaga, Y. Nishida, K. Magari, and H. Suzuki, "Broadband wavelength conversion based on apodized $\chi^{(2)}$ grating," J. Opt. Soc. Am. B **26**, 2315-2322 (2009).

68. M. V. Drummond, J. D. Reis, R. N. Nogueira, P. P. Monteiro, A. Luis Teixeira, S. Shinada, N. Wada, and H. Ito, "Error-free wavelength conversion at 160 Gbit/s in PPLN waveguide at room temperature," Electronics Letters **45**, 1135-1137 (2009).

69. A. Jechow, A. Heuer, and R. Menzel, "52%-Efficient Single-Pass SHG in a PPLN Waveguide by Frequency Doubling of a cw-DFB RW Laser Diode," in OSA Technical Digest (CD) (Optical Society of America, 2008), JWA13.

70. W. P. Risk, T. R. Gosnell, and A. V. Nurmikko, *Compact Blue-Green Lasers* (Cambridge University Press, 2003).

71. R. W. Boyd, *Nonlinear Optics,* 3rd Edition ed. (Academic Press, 2008).

72. D. H. Jundt, "Temperature-dependent Sellmeier equation for the index of refraction, ne, in congruent lithium niobate," Opt. Lett. **22**, 1553-1555 (1997).

73. Y. Petit, B. Boulanger, P. Segonds, P. Brand, C. Felix, B. Menaert, H. Ishizuki, and T. Taira, "Angular Quasi-Phase-Matching in MgO:PPLN," in OSA Technical Digest (CD) (Optical Society of America, 2008), CFK7.

74. M. M. Fejer, G. A. Magel, D. H. Jundt, and R. L. Byer, "Quasi-phase-matched second harmonic generation: tuning and tolerances," Quantum Electronics, IEEE Journal of **28**, 2631-2654 (1992).

75. D. Feng, N.-B. Ming, J.-F. Hong, Y.-S. Yang, J.-S. Zhu, Z. Yang, and Y.-N. Wang, "Enhancement of second-harmonic generation in $LiNbO_3$ crystals with periodic laminar ferroelectric domains," Applied Physics Letters **37**, 607-609 (1980).

76. K. Gallo, G. Assanto, and G. I. Stegeman, "Efficient wavelength shifting over the erbium amplifier bandwidth via cascaded second order processes in lithium niobate waveguides," Applied Physics Letters **71**, 1020-1022 (1997).

77. J. Wang and J. Sun, "40Gbit/s all-optical tunable format conversion in $LiNbO_3$ waveguides based on cascaded SHG/DFG interactions," in (SPIE, 2006), 634407-634407.

78. G. Shiming, Y. Changxi, X. Xiaosheng, T. Yu, Y. Zheng, and J. Guofan, "Bandwidth enhancement and response flattening of cascaded sum- and difference-frequency generation-based wavelength conversion," Optics Communications **266**, 296-301 (2006).

79. W. Sohler, D. Buchter, L. Gui, H. Herrmann, H. Hu, R. Ludwig, R. Nouroozi, V. Quiring, R. Ricken, C. Schubert, and H. Suche, "Wavelength conversion and optical signal processing in PPLN waveguides," in *Communications and Photonics Conference and Exhibition (ACP), 2009 Asia*, 2009), 1-2.

80. A. Tehranchi and R. Kashyap, "Wideband wavelength conversion using double-pass cascaded χ(2): χ(2) interaction in lossy waveguides," Optics Communications **283**, 1485-1488 (2010).

81. K. J. Lee, S. Liu, K. Gallo, P. Petropoulos, and D. J. Richardson, "Analysis of acceptable spectral windows of quadratic cascaded nonlinear processes in a periodically poled lithium niobate waveguide," Opt. Express **19**, 8327-8335 (2011).

82. A. Tehranchi, R. Morandotti, and R. Kashyap, "Efficient flattop ultra-wideband wavelength converters based on double-pass cascaded sum and difference frequency generation using engineered chirped gratings," Opt. Express **19**, 22528-22534 (2011).

83. G. Berrettini, A. Malacarne, E. Lazzeri, G. Meloni, and A. Bogoni, "Multiformat Wavelength Swapping in Periodically Poled Lithium Niobate Waveguide," in OSA Technical Digest (online) (Optical Society of America, 2013), JTh2A.58.

84. A. Malacarne, G. Meloni, G. Berrettini, L. Poti, and A. Bogoni, "Optical Multicasting of a 224Gb/s PM-16QAM Signal in a Periodically-Poled Lithium Niobate Waveguide," in OSA Technical Digest (online) (Optical Society of America, 2013), OM2G.2.

85. A. Tehranchi and R. Kashyap, "Flattop wideband wavelength converters based on cascaded sum and difference-frequency generation using step-chirped gratings," in *SPIE,* (San Francisco, California, USA, 2011), pp. 79171D-79178.

86. O. F. Yilmaz, S. R. Nuccio, S. Khaleghi, J. Y. Yang, L. Christen, and A. E. Willner, "Optical multiplexing of two 21.5 Gb/s DPSK signals into a single 43 Gb/s DQPSK channel with simultaneous 7-fold multicasting in a single PPLN waveguide," in *Optical Fiber Communication - incudes post deadline papers, 2009. OFC 2009. Conference on*, 2009), 1-3.

87. G.-W. Lu, S. Shinada, H. Furukawa, N. Wada, T. Miyazaki, and H. Ito, "160-Gb/s all-optical phase-transparent wavelength conversion through cascaded SFG-DFG in a broadband linear-chirped PPLN waveguide," Opt. Express **18**, 6064-6070 (2010).

88. A. Tehranchi and R. Kashyap, "Novel designs for efficient broadband frequency doublers using singly pump-resonant waveguide and engineered chirped gratings," IEEE Journal of Quantum Electronics **45**, 187-194 (2009).

89. M. Houe and P. D. Townsend, "An introduction to methods of periodic poling for second-harmonic generation," Journal of Physics D: Applied Physics **28**, 1747 (1995).

90. J. Webjorn, V. Pruneri, P. S. J. Russell, J. R. M. Barr, and D. C. Hanna, "Quasi-phase-matched blue light generation in bulk lithium niobate, electrically poled via periodic liquid electrodes," Electronics Letters **30**, 894-895 (1994).

91. K. Pandiyan, Y. S. Kang, H. H. Lim, B. J. Kim, and M. Cha, "Nondestructive quality evaluation of periodically poled lithium niobate crystals by diffraction," Opt. Express **17**, 17862-17867 (2009).

92. R. S. Weis and T. K. Gaylord, "Lithium niobate: Summary of physical properties and crystal structure," Appl. Phys. A **37**, 191-203 (1985).

93. S. C. Abrahams, J. M. Reddy, and J. L. Bernstein, "Ferroelectric lithium niobate. 3. Single crystal X-ray diffraction study at 24℃," Journal of Physics and Chemistry of Solids **27**, 997-1012 (1966).

94. S. C. Abrahams, W. C. Hamilton, and J. M. Reddy, "Ferroelectric lithium niobate. 4. Single crystal neutron diffraction study at 24℃," Journal of Physics and Chemistry of Solids **27**, 1013-1018 (1966).

95. "IRE Standards on Piezoelectric Crystals (1949)," in *Proc. IRE, 37*, 1949), 1378.

96. O. Y. Jeon, "Broadband optical parametric interactions in periodically poled lithium niobate crystals," (Pusan National University, Busan, Korea, 2006).

97. T. J. Yang, U. Mohideen, and M. C. Gupta, "Near-field scanning optical microscopy of ferroelectric domain walls," Applied Physics Letters **71**, 1960-1962 (1997).

98. V. Gopalan and T. E. Mitchell, "Wall velocities, switching times, and the stabilization mechanism of 180° domains in congruent $LiTaO_3$ crystals," Journal of Applied Physics **83**, 941-954 (1998).

99. R. Landauer, "Electrostatic Considerations in $BaTiO_3$ Domain Formation during Polarization Reversal," Journal of Applied Physics **28**, 227-234 (1957).

100. V. Gopalan, T. E. Mitchell, Y. Furukawa, and K. Kitamura, "The role of nonstoichiometry in 180° domain switching of $LiNbO_3$ crystals," Applied Physics Letters **72**, 1981-1983 (1998).

101. T. J. Yang, V. Gopalan, P. J. Swart, and U. Mohideen, "Direct Observation of Pinning and Bowing of a Single Ferroelectric Domain Wall," Physical Review Letters **82**, 4106-4109 (1999).

102. R. C. Miller and G. Weinreich, "Mechanism for the Sidewise Motion of 180° Domain Walls in Barium Titanate," Physical Review **117**, 1460-1466 (1960).

103. A. Savage and R. C. Miller, "Temperature Dependence of the Velocity of Sidewise 180° Domain-Wall Motion in $BaTiO_3$," Journal of Applied Physics **31**, 1546-1549 (1960).

104. R. C. Miller and A. Savage, "Motion of 180° Domain Walls in $BaTiO_3$ under the Application of a Train of Voltage Pulses," Journal of Applied Physics **32**, 714-721 (1961).

105. S. Chao, W. Davis, D. D. Tuschel, R. Nichols, M. Gupta, and H. C. Cheng, "Time dependence of ferroelectric coercive field after domain inversion for lithium-tantalate crystal," Applied Physics Letters **67**, 1066-1068 (1995).

106. V. Y. Shur, E. L. Rumyantsev, E. Nikolaeva, E. Shishkin, R. G. Batchko, G. D. Miller, M. M. Fejer, and R. L. Byer, "Micro- and nanoscale domain engineering in lithium niobate and lithium tantalate," 143-154 (2000).

107. M. Missey, S. Russell, V. Dominic, R. Batchko, and K. Schepler, "Real-time visualization of domain formation in periodically poled lithium niobate," Opt. Express **6**, 186-195 (2000).

108. V. Gopalan, Q. X. Jia, and T. E. Mitchell, "In situ video observation of 180° domain kinetics in congruent $LiNbO_3$ crystals," Applied Physics Letters **75**, 2482-2484 (1999).

109. S. I. Bozhevolnyi, J. M. Hvam, K. Pedersen, F. Laurell, H. Karlsson, T. Skettrup, and M. Belmonte, "Second-harmonic imaging of ferroelectric domain walls," Applied Physics Letters **73**, 1814-1816 (1998).

110. F. Saurenbach and B. D. Terris, "Imaging of ferroelectric domain walls by force microscopy," Applied Physics Letters **56**, 1703-1705 (1990).

111. R. Luthi, H. Haefke, K.-P. Meyer, E. Meyer, L. Howald, and H.-J. Guntherodt, "Surface and domain structures of ferroelectric crystals studied with scanning force microscopy," Journal of Applied Physics **74**, 7461-7471 (1993).

112. V. Gopalan and T. E. Mitchell, "In situ video observation of 180° domain switching in $LiTaO_3$ by electro-optic imaging microscopy," Journal of Applied Physics **85**, 2304-2311 (1999).

113. I. E. Barry, G. W. Ross, P. G. R. Smith, R. W. Eason, and G. Cook, "Microstructuring of lithium niobate using differential etch-rate between inverted and non-inverted ferroelectric domains," Materials Letters **37**, 246-254 (1998).

114. E. Iannone and R. Sabella, "Wavelength conversion in WDM optical networks: a comparison among different devices based on semiconductor amplifiers," in *Lasers and Electro-Optics Society Annual Meeting, 1995. 8th Annual Meeting Conference Proceedings, Volume 1., IEEE*, 1995), 42-43 vol.42.

115. C. A. Brackett, A. S. Acampora, J. Sweitzer, G. Tangonan, M. T. Smith, W. Lennon, K. C. Wang, and R. H. Hobbs, "A scalable multiwavelength multihop optical network: a proposal for research on all-optical networks," Lightwave Technology, Journal of **11**, 736-753 (1993).

116. J. M. H. Elmirghani and H. T. Mouftah, "All-optical wavelength conversion: technologies and applications in DWDM networks," Communications Magazine, IEEE **38**, 86-92 (2000).

117. C. Q. Xu, H. Okayama, and M. Kawahara, "1.5 μm band efficient broadband wavelength conversion by difference frequency generation in a periodically domain-inverted $LiNbO_3$ channel waveguide," Applied Physics Letters **63**, 3559-3561 (1993).

118. M. H. Chou, I. Brener, M. M. Fejer, E. E. Chaban, and S. B. Christman, "1.5-μm-band wavelength conversion based on cascaded second-order nonlinearity in $LiNbO_3$ waveguides," Photonics Technology Letters, IEEE **11**, 653-655 (1999).

119. M. L. Bortz and M. M. Fejer, "Measurement of the second-order nonlinear susceptibility of proton-exchanged LiNbO3," Opt. Lett. **17**, 704-706 (1992).

120. F. Hideaki, N. Ampalavanapillai, W. Naoya, S. Satoshi, T. Hiroshi, and M. Tetsuya, "Tunable All-Optical Wavelength Conversion of 160-Gb/s RZ Optical Signals by Cascaded SFG-DFG Generation in PPLN Waveguide," Photonics Technology Letters, IEEE **19**, 384-386 (2007).

121. S. Jing, Y. Song, G. Wanyi, and Y. Jian Quan, "Optimum Design for 160-Gb/s All-Optical Time-Domain Demultiplexing Based on Cascaded Second-Order Nonlinearities of SHG and DFG," Quantum Electronics, IEEE Journal of **45**, 694-699 (2009).

122. M. Ahlawat, A. Tehranchi, K. Pandiyan, M. Cha, and R. Kashyap, "Tunable Wavelength Broadcasting in a PPLN with Multiple QPM Peaks," in *Nonlinear Photonics*, 2012), JTu5A.37.

123. S. K. Pandiyan, "Fabrication of Periodically Poled Lithium Niobate Crystals for Quasi-Phase Matching Nonlinear Optics and Quality Evaluation by Diffraction," (Pusan National University, Busan, South Korea, 2010).

124. G. D. Boyd and D. A. Kleinman, "Parametric Interaction of Focused Gaussian Light Beams," Journal of Applied Physics **39**, 3597-3639 (1968).

125. C.-S. Bres, A. O. J. Wiberg, J. Coles, and S. Radic, "160-Gb/s optical time division multiplexing and multicasting in parametric amplifiers," Opt. Express **16**, 16609-16615 (2008).

126. G. Shiming, C. Yang, and J. Guofan, "Flat broad-band wavelength conversion based on sinusoidally chirped optical superlattices in lithium niobate," Photonics Technology Letters, IEEE **16**, 557-559 (2004).

127. A. Bostani, A. Tehranchi, and R. Kashyap, "Engineering of effective second-order nonlinearity in uniform and chirped gratings," J. Opt. Soc. Am. B **29**, 2929-2934 (2012).

128. M. Yamada, N. Nada, M. Saitoh, and K. Watanabe, “First-order quasi-phase matched $LiNbO_3$ waveguide periodically poled by applying an external field for efficient blue second-harmonic generation,” Applied Physics Letters **62**, 435-436 (1993).